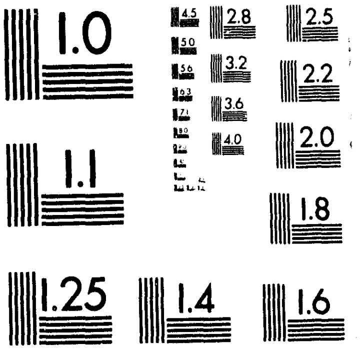
1.0
1.1
1.25
1.4
1.6
1.8
2.0
2.2
2.5
2.8
3.2
3.6
4.0
4.5
5.0
5.6
6.3
7.1
8.0

1 of 2

1737

EVALUATION OF SUPERCONDUCTING WIGGLER DESIGNS AND FREE-ELECTRON LASER SUPPORT

Final Report

Submitted to

University of California
Los Alamos National Laboratory
Post Office Box 990
Los Alamos, New Mexico

by

Spectra Technology, Inc.
2755 Northup Way
Bellevue, Washington 98004

12 OCTOBER 1990

DISCLAIMER

MASTER

DISTRIBUTION OF THIS DOCUMENT IS UNLIMITED

MONTHLY PROGRESS REPORT

October 1989

Contract: 9-XG9-E9513-1
STI Control No.: 1737

EVALUATION OF SUPERCONDUCTING WIGGLER DESIGNS AND FREE-ELECTRON LASER SUPPORT

Monthly Progress Report
October 1989

Task 2.1 SPACE-BASED FEL WIGGLER DEVELOPMENT

A survey of existing superconducting undulators, wigglers, dipoles and quadrupoles was completed. We found that no magnet has been designed to handle heating from any source in excess of 10 W/m. In the SSC dipoles, the synchrotron radiation heating budget was 0.12 W/m. Including liquid helium cooling channels in the vacuum tube to remove image current heating is desirable. Radiation heating is problematical, but it's magnitude is unknown. The gap standoff i.e. the difference between magnetic gap and vacuum tube aperture will be effected by cooling considerations, magnetic forces of attraction and vacuum tube strength. On existing superconducting wigglers the standoff increases with increasing magnetic attraction, despite significant design differences between the wigglers. Systems without attractive forces, such as dipoles still have 3mm gap standoffs. We have established a very rough standoff scaling with attractive force.

Magnetic field calculations of a holmium pole wiggler using PANDIRA have been completed. These calculations have been used to determine gap, wavelength and current scaling laws of the magnetic field. Peak magnetic fields in the coils, forces and load lines have been determined. Scaling laws for the stresses on the wires in the coils have been calibrated using the finite-element stress analysis code COSMOS. By combining the peak field load lines with the critical current curve of the superconductor we have established peak critical currents vs wavelength.

The superconductor of choice is niobium titanium. While niobium tin has the potential for higher current densities, the brittleness of the material limits its usefullnes to long wavelength wigglers. At long wavelegths the wigglers already have very large a_w (>30). Short wavelength devices benefit from increases currents, but niobiom tin may not be readily formed into small enough coils.

Superconducting magnets cannot operate at their full rated critical current because the addition of extremely small amounts of energy will cause the wires to heat up and go normal. The energy input could be due to many factors such as mechanical disturbances, insulator fracture, heat leaks, radiation heating or beam tube heating by image currents. We have determined distributed disturbance, transient quench energy densities; point disturbance, transient energy; minimum propagating zone sizes and current-sharing temperatures vs wavelength and current. (There is a negligable gap dependance as well.) Estimates of maximum current densities vs wavelength have been made. This initial stability analysis indicates that short wavelength systems are more stable than long wavelength systems since their magnetic fields are lower which leads to lower magnetic stresses. Continuous disturbances such as heat leaks, radiation heating, or image current heating will impact the cryogenic engineering and may degrade performance below the estimates based on transient disturbance stability analysis.

Superfluid helium cooling has been proposed as a means of increasing performance in superconducting magnets due to the increased specific heat, thermal conductivity and very low viscosity of the superfluid. These systems must be run pressurized to about 1 atm and operated below 1.8°K to maximize heat transfer by minimizing film boiling. At present, due to concerns about image current and radiation heating we think that the superfluid helium option may not be realistic. We found no wigglers, dipoles or quadrupoles which use superfluid cooling. Several use forced flow cooling and more use bath cooling. We only found one instance when superfluid cooling has been used. It was on a high field, low-current-density solenoid.

Wedged pole hybrid scaling laws for magnetic field and mass have been completed. Minimization of pole saturation was used to find the optimum magnet and pole sizes.

Next month's work will consist of completing a more detailed write-up; further studies into stability, especially probing the relative importance of distributed vs point disturbances; refining the mass scaling to more accurately reflect the support structure scaling with magnetic attraction between wiggler halves; investigating relative merits of bath cooling vs supercritical helium forced flow cooling vs lower temperature cooling (non-superfluid); and refining the cryovessel mass estimates based on the cooling system design. Lowering the cryogen temperature can enhance stability and allow higher currents, if needed. Only the short wavelength wigglers are lacking in field strength, so we will concentrate on the amount of improvement to be gained by using a lower helium temperature at short wavelengths.

SUMMARY OF SCALING LAWS

POLE-COIL GEOMETRY

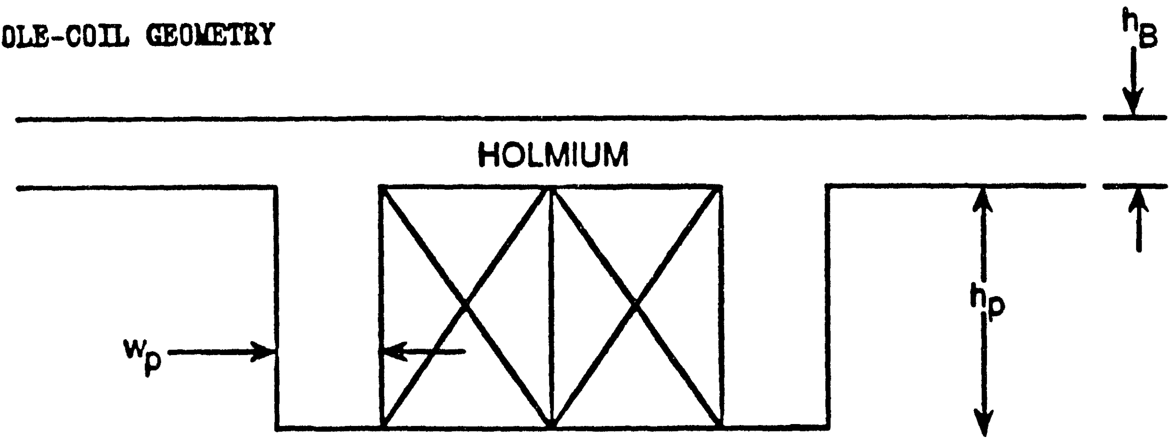

$$B(T) = 1.26\ e^{-\pi g/\lambda_w} + 0.0269\ j\ \left(kA/cm^2\right)\ \lambda_w(cm)\, e^{-\pi g/\lambda_w}$$

$$\text{Mass}\ (kg/m) = 0.55\ \lambda_w^2\ (cm) + M_c$$

$$M_c \sim 400\ kg/m$$

$$h_B/h_p \sim \frac{1}{4}$$

$$h_p/\lambda_w = \frac{3}{8}$$

$$w_p/\lambda_w = 0.2$$

$$\text{transverse length} = 1.5\ \lambda_w$$

$$B_{peak}^{coil}\ (T) = 0.843 + 0.0147j\ \lambda_w\ (kA/cm)$$

$$j^{peak} = \sum_{n=0}^{3} C_n\ \lambda_w^h$$

$$C_0 = 130\ kA/cm^2$$

$$C_1 = -30.6\ kA/cm^3$$

$$C_2 = 3.3\ kA/cm^4$$

$$C_3 = -0.13\ kA/cm^5$$

$$\text{Peak hoop stress} = 2x10^{-4}\ \left(j\ \lambda_w(kA/cm)\right)^2$$

$$\text{Attractive force (ton/m)} = 2.2x10^{-6}\ \frac{B^2(gauss)\ 1.5\ \lambda_w(cm)}{16\ \pi}$$

$$\Delta gap\ (cm) = \max\left\{0.3,\ 6.7x10^{-1} + 1.4x10^{-3}\ f/l\ (ton/m) + 4.7x10^{-5}\ (f/l)^2\right\}$$

Wedged Pole Hybrid

$$B(T) = 0.0296 + 1.4u + 2.14u^{-2} - 1.37\ u^3$$

$$u = e^{-\pi g/\lambda_w}$$

$$M(kg/m) = \left(1.0 + 3.0u - 8.7\ u^2 + 18.3\ u^3 - 9.2\ u^4\right)\ \lambda_w^2\ (cm)\ x\ 3$$

Task 2.2 FEL ANALYSIS SUPPORT

This task was initiated by examination of the wiggler prebuncher option for enhancement of the performance of the the Laser Subsystem (LSS) to be sited at the White Sands Missile Range (WSMR). The prebuncher appears to be a design modification which provides significant potential performance improvement with minimal added cost. Detailed results are documented in the attached memorandum.

Wiggler performance sensitivity studies were initiated during the latter half of the performance period. A two-plane model of alternating-type e-beam trajectory correctors was developed and implemented in the LANL FELEX code in an effort to provide a more realistic representation of the expected LSS geometry. Multipass calculations in a mode-matched optical cavity will be used to quantify the expected degradation due to wiggler field errors and trajectory position sensing errors; results are expected during November.

Spectra Technology Memorandum

Date: 13 October 1989

To: Brian McVey, Distribution

From: Dave Quimby

Subject: LSS Prebuncher Analysis

INTRODUCTION. The use of an electron prebuncher has been suggested as a means for enhancing the performance of the LSS oscillator. In this system, performance is measured primarily in terms of power output. This memo reviews the prebuncher design in an effort to quantify the potential improvement. In order to evaluate the prebuncher on its own merits, one ground rule used here is that the overall wiggler length is held fixed as the prebuncher is added. Adding wiggler length to enhance FEL performance is a separate consideration.

BACKGROUND. Prebunchers for tapered wigglers have been examined theoretically [1-3] and experimentally [4,5]. A sketch of the typical prebuncher geometry is shown in Figure 1. A short uniform wiggler of length L(Buncher) is placed at a precise distance L(Drift) in front of the main tapered wiggler. The prebuncher exerts a small velocity modulation on the e-beam. This modulation is then converted to spatial bunching at the optical wavelength as the electrons drift to the main undulator. The drift distance determines where the electron bunches are inserted relative to the separatrix of the ponderomotive potential well. Note that the drift length does not necessarily have to be a physical drift space; a magnetic dispursive section (as employed in optical klystrons) is a compact way to achieve a long equivalent drift within a short distance.

PREBUNCHER DESIGN. Parameters representative of the LSS simulations completed here are listed in Table 1. Note that misalignments and field errors have been neglected for the purposes of this study. Under the constant overall wiggler length restriction, the prebuncher may use the same gap and period as the main wiggler without restricting propagation of the Gaussian optical mode.

In this study, the wiggler taper has been self-designed according to the following resonant phase prescription

$$\psi_r(z) = \frac{\psi_1 T(z_2) - \psi_2 T(z_1) + (\psi_2 - \psi_1) T(z)}{T(z_2) - T(z_1)}$$

where, $T(z) \equiv \tan^{-1}\left(\frac{z-z_0}{z_t}\right)$.

The resonant phase angle is taken to be Psi1 = 0 at the entrance to the main wiggler section (Z = Z1) and Psi2 = 30 degrees at the exit (Z = Z2). The phase varies according to the arctangent function at intervening positions. This programmed phase prescription has been proposed by Los Alamos [6] and is an elegant generalization of the simple constant section plus linearly tapered section often used by STI. (The arctangent prescription reduces to the constant plus linearly tapered prescription in the limit as the transition length parameter (Zt) goes to zero.)

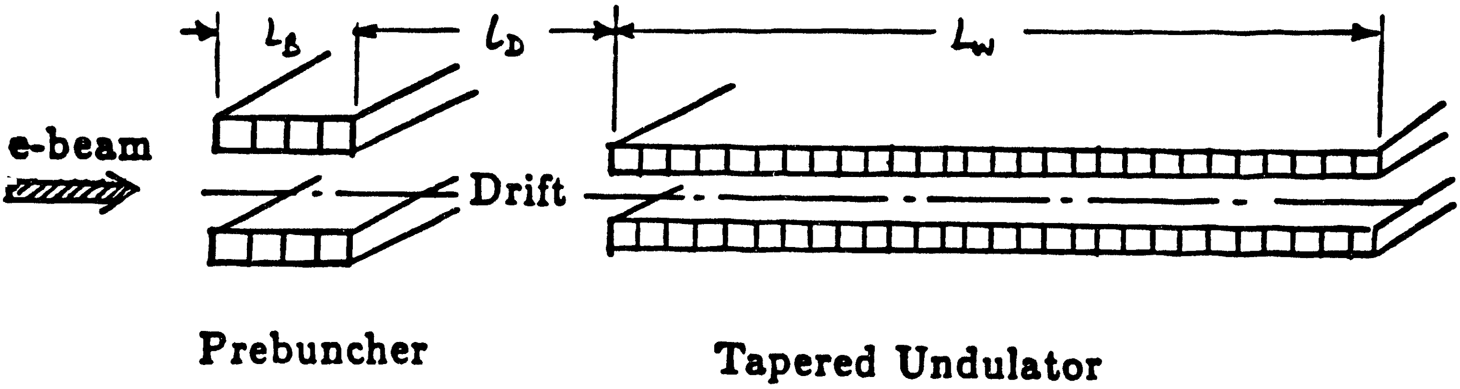

Figure 1. Schematic of prebuncher configuration

Table 1. Standard LSS Parameters with Prebuncher

Quantity	Standard Value	Comment
E-BEAM:		
Resonant Energy	100 MeV	
Peak Current	480 A	384 A micro. avg. used in single wavefront calculations
Energy Spread	1 percent	Gaussian distrib., 90% particles
Norm. Emittance	57 pi mm-mrad	Gaussian distrib., 90% particles
Radius	0.67 mm	Edge radius, 90% particles
Betatron Period	9.5 m	
Misalignment	None	
Mismatching	None	
WIGGLER:		
Overall Length	14.9 m	
Period	3.72 cm	
Peak Field	4.47 kG	
Aw (RMS)	1.099	
Clear Aperture	1.152 cm	
Vac. Tube Ellipticity	2:1	
Field Errors	None	
PREBUNCHER:		
L(Buncher)	0.50 m	
Bucket Height	2.6 %	
Amount of induced energy spread	+/- 0.75%	
DRIFT SECTION:		
L(Drift)	1.05 m	
N(Drift)	13	No. of waves of slip
MAIN WIGGLER:		
L(Main)	13.35 m	
Taper Prescription	Programmed Resonant Phase Angle	
PsiR(entr)	0 deg	Psi1 parameter
PsiR(exit)	30 deg	Psi2 parameter
Transition Position	At 0.25 L(Main)	Zo parameter
Transition Length	2.5 m	Zt parameter
Bucket Height	2.6 %	At entrance
OPTICAL BEAM:		
Assumed Steady-State Input Power	1.6 GW	
Resonant Wavelength	1.06 microns	
Rayleigh Range	5.0 m	
Waist Radius	1.30 mm	1/e**2 intensity point
Misalignment	None	
Input Optical Beam	Gaussian TEMoo	Assumes perfect mode matching

Throughout a long drift length, the electrons slip back many optical wavelengths along the optical pulse. If the buncher and wiggler are spaced correctly, the bunched electrons are injected into the wiggler at the optimum phase for capture and deceleration. As the drift distance is varied, slippage arguments dictate that best capture will be repeated on a spatial scale of (2*Gamma**2)x(Optical Wavelength), the free space distance within which a resonant electron slips back one optical wavelength. Thus there are a large number of possible capture windows, which for the LSS parameters repeat every 8.12 cm. This is illustrated in Figure 2, which shows the fine scale variation in the vicinity of the nominal 1.05 m drift length listed in Table 1.

The prebuncher length is generally limited by the condition that the additional energy spread induced (together with the initial energy spread, both true and effective) not exceed the energy spread acceptance of the main wiggler. For the LSS parameters at an input power of 1.6 GW (representative of the expected peak power at saturation), we see that the prebuncher designer has considerable freedom. The bucket height of the main wiggler at the design optical power is 2.6 percent. This greatly exceeds the nominal true energy spread of the e-beam (1 percent). In fact, PARMELA simulations suggest that considerably smaller energy spread is possible, perhaps as low as 0.3 percent [6]. The buncher length required to induce a given small amount of energy spread (half width) into an initially monoenergetic beam is given by

$$L_B = \frac{\gamma^2}{e_s a_w}\left(\frac{\Delta\gamma}{\gamma}\right)_{HW} \qquad (2)$$

where, $e_s = \frac{eE_0}{\sqrt{2}mc^2}$, $a_w = \frac{eB_0}{\sqrt{2}mc^2 k_w}$.

The 0.5 m LSS buncher length listed in Table 1 provides an energy modulation of amplitude 0.75 percent (1.5 percent full width). This is a relatively large value, implying that only a modest drift length is needed to convert the velocity modulation into bunching. Figure 3 shows the calculated LSS performance for various buncher lengths. This also shows that optimal performance is obtained for the 0.5 m buncher length.

Figure 3 also implies that the capture fraction increases with increasing drift length up to point where optimum bunching has been achieved. Performance is degraded by overbunching at longer drift lengths. The optimum bunching point is expected to be approximately when the electron of maximum induced energy shift drifts in phase by pi/2 relative to the resonant particle. This condition is given by

$$L_D = \frac{\lambda_s \gamma^2}{4(\Delta\gamma/\gamma)_{HW}} \qquad (3)$$

which for the LSS parameters gives 1.35 m at L(Buncher) = 0.5 m. As shown in Figure 4, the actual optimum drift length is slightly less than predicted by these simple arguments.

Dispersive drift sections are often characterized by the parameter Nd, which is the amount of slippage of the electrons measured in terms of number of optical waves [7]. The Nd value is given by

$$N_d = \frac{L_D}{2\gamma^2\lambda_s} = \frac{L_D}{\lambda_w(1+a_w^2)} \qquad (4)$$

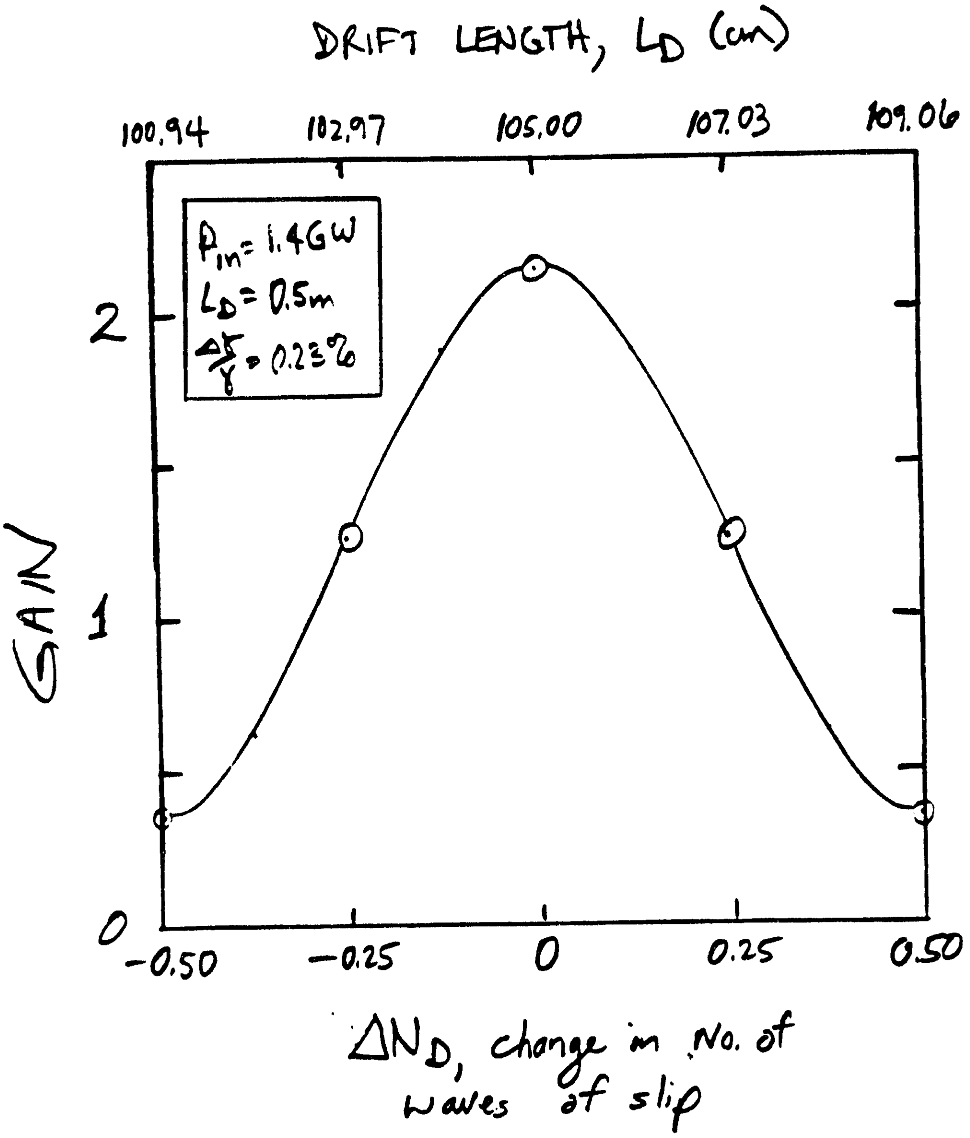

Figure 2. Periodicity of capture window has been verified to be $\Delta N_D = 1$, or $\Delta L_D = \lambda_s (2\gamma^2) = 8.12$cm

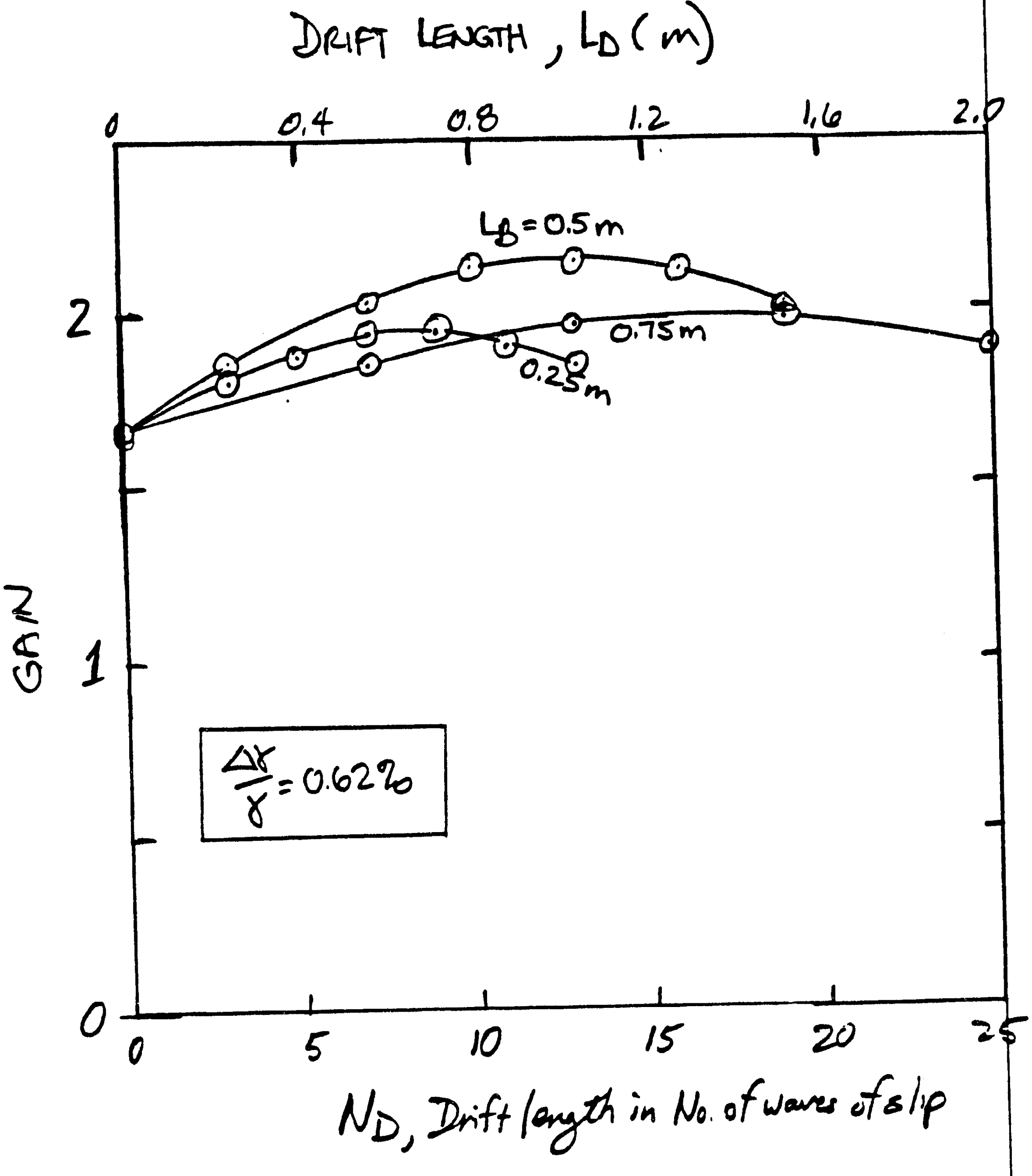

Figure 3. Optimum buncher length is about 0.5 m

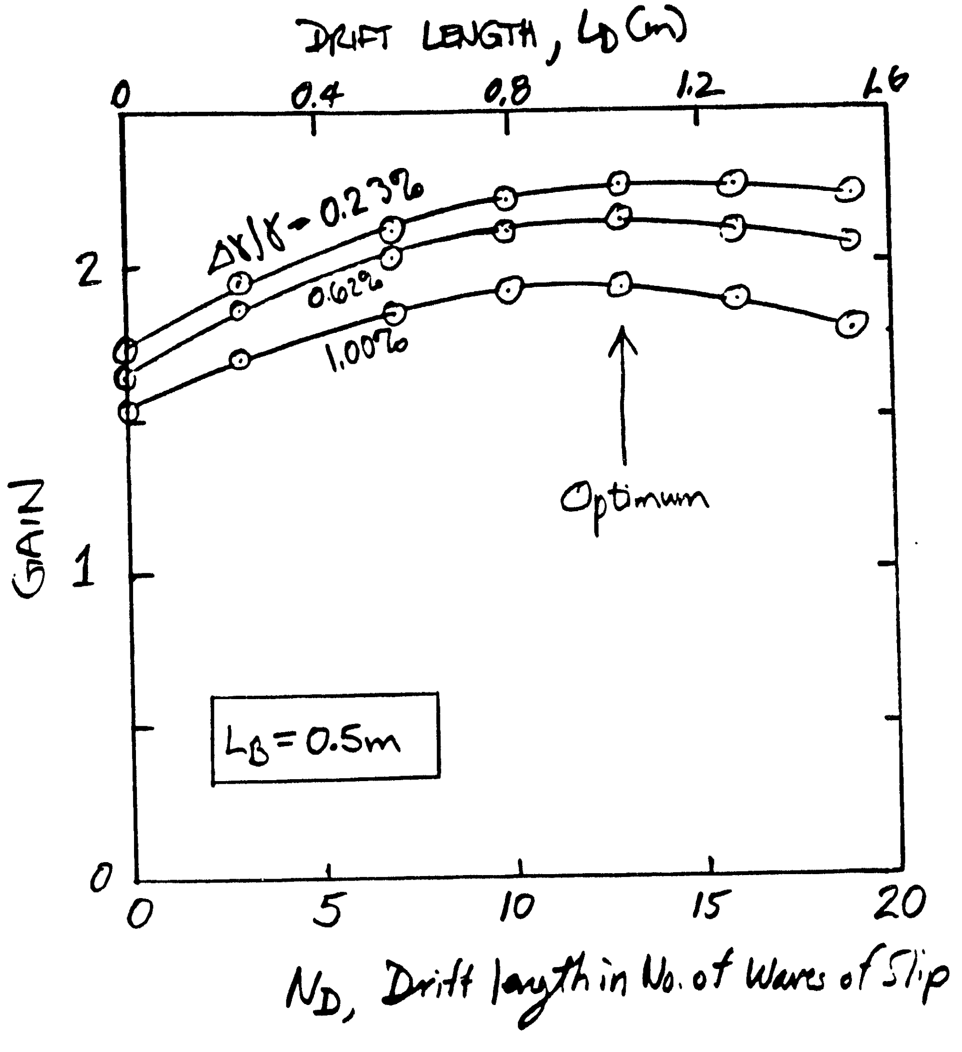

Figure 4. Optimum Drift Length is ~1.05m; this quantity is only weakly dependent on input energy spread for the LSS parameters.

Note that Nd remains constant if the FEL wavelength is tuned by varying the electron energy, since the product of gamma**2 x lambda remains fixed. However, if the optical wavelength is tuned by varying the wiggler gap (Aw tuning), the drift length must also be adjusted to keep Nd at the desired value.

DRIFT LENGTH TUNING. The LSS wiggler is envisioned to be built in 20 0.75 m modules. A 1.05 m drift length could be created by simply unloading the last one-third of the magnets and poles from the first module and leaving the second module out. A strong dispersive section is not essential; the drift length is short enough that one would not lose a large fraction of the wiggler length. (This contrasts with earlier prebuncher analysis for the NISUS parameters [3], where it was shown that the only practical way for implementation would require a strong dispersive section.)

It is essential that the drift length be adjustable to produce the proper phasing for optimal capture under various conditions. Three tuning options are available. One is to put the prebuncher on an axial translation stage. That would be a considerable complication for the LSS wiggler since it also requires transverse gap adjustment. A far more practical approach for LSS is to provide a weak electromagnetic dispersive element for fine tuning. A third option would be to use a strong electromagnetic dispersive section. This would likely fit within approximately a 20 cm length, thus allowing the second wiggler module to be reinserted.

Table 2 compares the relative performance of the various options. For low energy spread, the use of prebuncher with a long drift section improves the gain by 21-24 percent relative to what it would be without any prebuncher. The improvement is about 10 percent at 1 percent energy spread. The use of a strong dispersive section can further improve the performance by several percentage points.

Table 2. Prebuncher Benefits for Various LSS Embodiments

ENERGY SPREAD	RELATIVE GAIN AT FIXED INPUT POWER		
	Without Prebuncher	Prebuncher w/ Long Drift	Prebuncher w/ Strong Disperser
0.23%	1.06	1.31	1.35
0.62%	1.02	1.23	1.27
1.00%	1.00	1.10	1.13

The results shown in Table 2 show that the full benefit of the prebuncher is felt for energy spread values up to around 0.6 percent. Initial accelerator modeling indicates that it may well be realistic to expect the energy spread to be in this range. In any case, the improvement is very noticeable even for the nominal 1 percent energy spread.

STARTUP CONSIDERATIONS. Figure 5 examines the expected gain during startup with a prebuncher in place. Note that these are single-pass gain calculations using TEMoo mode input; the actual gain may be somewhat lower during startup because of mode mismatching. These results show that startup should proceed easily without chirp (as will be the case with a fixed grating rhomb).

Figure 6 compares the gain saturation characteristics for lasing at a fixed optical wavelength with and without using a prebuncher. Interestingly, the prebuncher improves both small-signal and saturated performance, even at an energy spread of 1 percent. Somewhat surprisingly, there is no pronounced gain dip at the transition from small signal to trapping. This may be feature resulting from the gradual transition between the constant section and the linearly tapered section in the Los Alamos taper prescription or from the relatively high gain of the LSS system.

The use of a time-dependent taper has been suggested as a way to optimize the LSS performance after startup. Figure 7 examines this issue for the case of the normal wiggler configuration without prebuncher. Revision of the resonant phase angle prescription to a constant phase angle eliminates the untapered section of the wiggler and results in about a 7 percent improvement in saturated gain at fixed input power. Other alternative taper prescriptions may provide additional advantages.

CONCLUSIONS. The applicability of a prebuncher has been examined for the parameters of the LSS oscillator experiment. The potential improvement is modest (10 to 27 percent, depending on the energy spread and drift length configuration), but this improvement is extremely significant for a high average power device. The prebuncher can be implemented very easily by including a modest (approx. 1 m) drift space together with a weak electromagnetic dispersive element for fine tuning the effective drift length to optimize the capture fraction. Alternatively, the use of a stronger electromagnetic dispersive section would allow marginally better performance by allowing a somewhat longer main wiggler within the same overall length.

The potential improvement has been quantified in terms of added gain at fixed input power in this memo. The potential improvement can then be thought of as added margin to protect against possible deleterious effects. Alternatively, the prebuncher could be used to produce higher efficiency at fixed gain, thus providing a large potential cost savings by reducing input power requirements. For this latter application the potential improvement may be more dramatic. In this case the gain-extraction product may be a more useful figure of merit; the potential improvement is expected to roughly scale as the square of the relative gain at fixed input power.

The only added cost for implementation of a prebuncher option would be for the design and development of the electromagnetic dispersive section. Considering the large potential benefit for minimal additional effort, the LSS prebuncher should be seriously considered for implementation. A decision to proceed only adds more flexibility, the straight wiggler would be retained as a viable option.

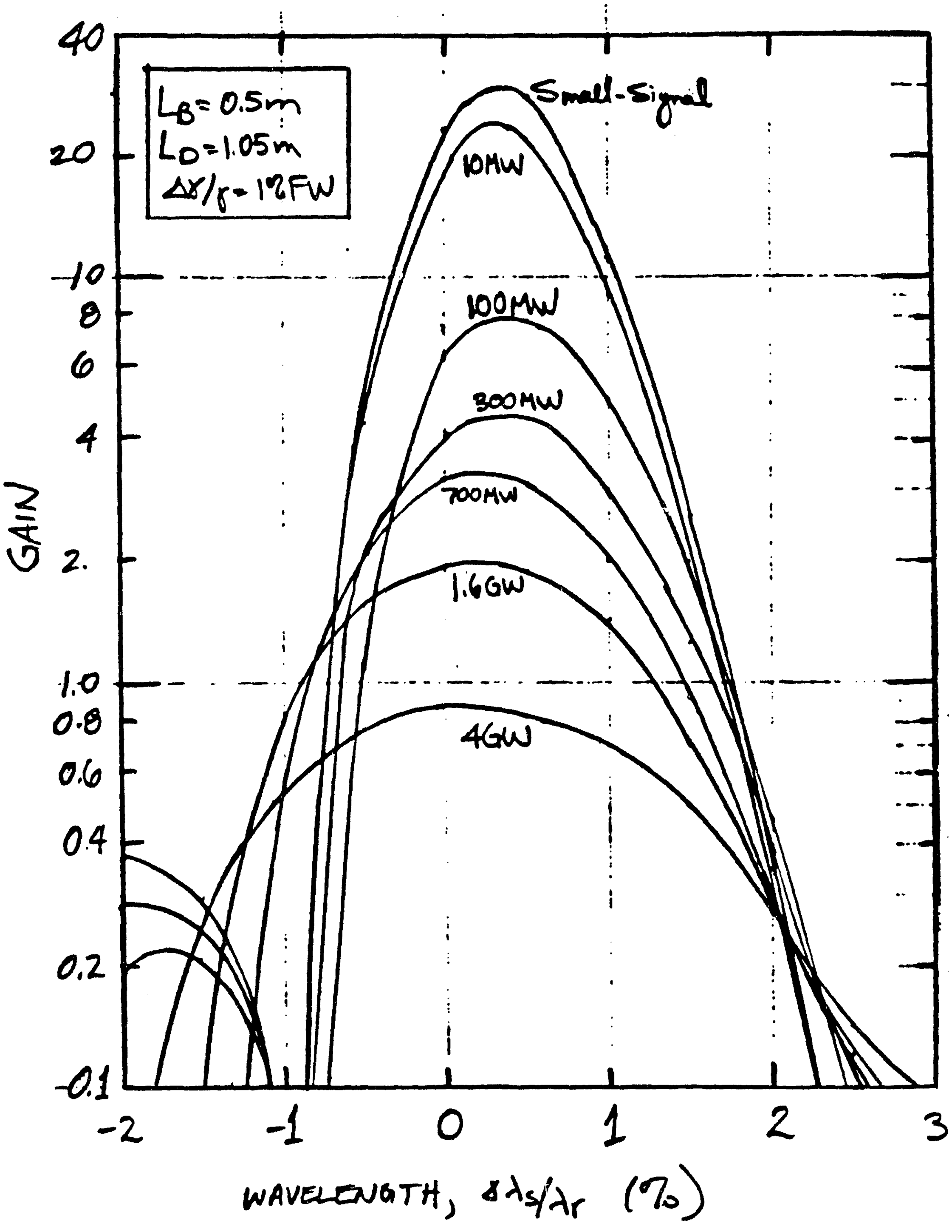

Figure 5. Gain curves at various input powers with prebuncher in place.

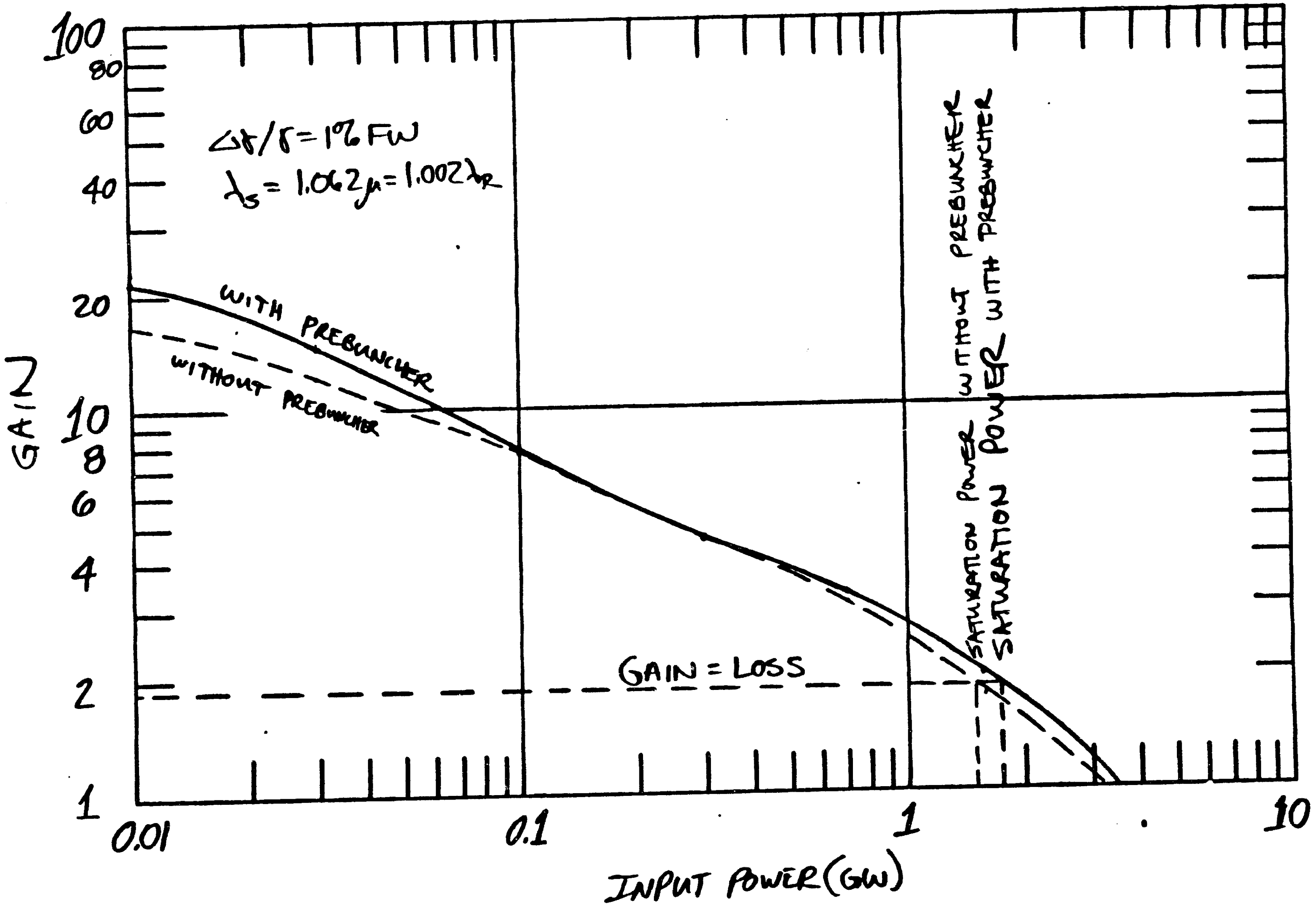

Figure 6. Gain saturation characteristics with and without a prebuncher.

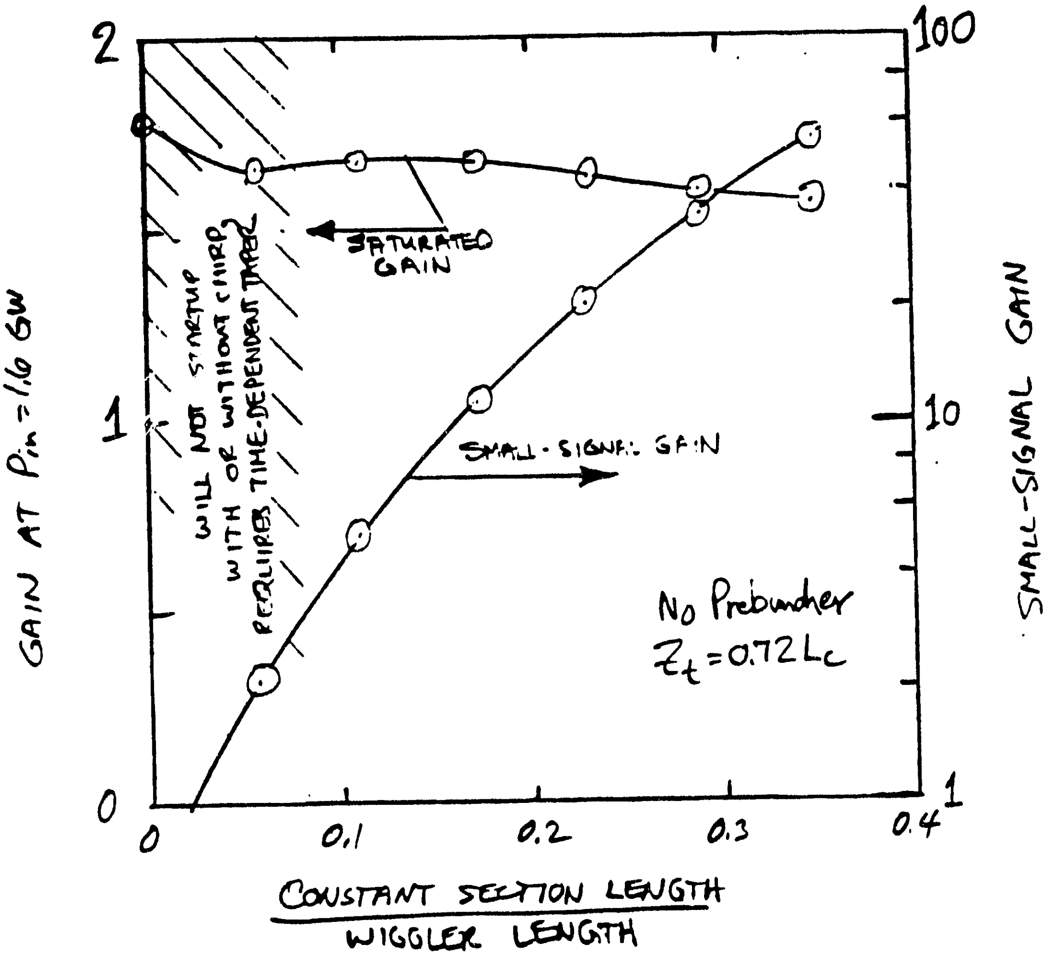

Figure 7. Dependence of small-signal and saturated gain on constant section length for a straight wiggler (without prebuncher)

REFERENCES

[1] C.-C. Shih and M.Z. Caponi, "Theory of Multicomponent Wiggler Free-Electron Lasers in the Small-Signal Regime," Phys. Rev. A, Vol. 26, 438 (1982).

[2] H. Takeda, B.D. McVey, and J.C. Goldstein, "Theoretical Study of a High-Extraction Efficiency Undulator for a Free Electron Laser Oscillator," Nucl. Instr. and Meth., Vol. A259, 295 (1987).

[3] D. Quimby, "HAP Prebuncher Analysis," memo dated 14 February 1989.

[4] J.A. Edighoffer, G.R. Neil, C.E. Hess, T.I. Smith, S.W. Fornaca, and H.A. Schwettman, "Variable-Wiggler Free-Electron-Laser Oscillation," Phys. Rev. Lett., Vol. 52, 344 (1984).

[5] D.W. Feldman, H. Takeda, R.W. Warren, J.E. Sollid, W.E. Stein, W.J. Johnson, A.H. Lumpkin, and R.B. Feldman, "High Extraction Efficiency Experiments with the Los Alamos Free-Electron Laser," presented at the Tenth International Free Electron Laser Conference, Jerusalem, Israel, 29 August-2 September 1988, to be published in Nucl. Instr. and Meth. (1989).

[6] B. McVey, Los Alamos National Laboratory, private communication.

[7] P. Elleaume, "Optical Klystrons," J. de Phys. (Paris), Vol. 44, C1-333 (1983).

Distribution:

Boeing - Denis Pistoresi, John Adamski, Bob Papadopulos
LANL - Brian McVey
STI - Jack Slater, Steve Gottschalk, Kem Robinson, file (STI 1737).

superfluid cooling has been used. It was on a high field, low-current-density solenoid.

Wedged pole hybrid scaling laws for magnetic field and mass have been completed. Minimization of pole saturation was used to find the optimum magnet and pole sizes.

Next month's work will consist of completing a more detailed write-up; further studies into stability, especially probing the relative importance of distributed vs point disturbances; refining the mass scaling to more accurately reflect the support structure scaling with magnetic attraction between wiggler halves; investigating relative merits of bath cooling vs supercritical helium forced flow cooling vs lower temperature cooling (non-superfluid); and refining the cryovessel mass estimates based on the cooling system design. Lowering the cryogen temperature can enhance stability and allow higher currents, if needed. Only the short wavelength wigglers are lacking in field strength, so we will concentrate on the amount of improvement to be gained by using a lower helium temperature at short wavelengths.

SUMMARY OF SCALING LAWS

POLE-COIL GEOMETRY

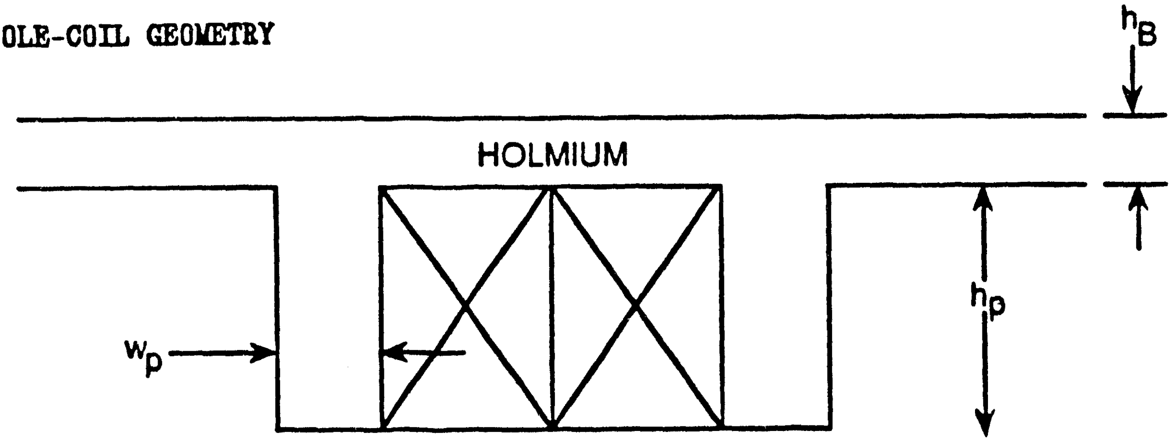

MONTHLY PROGRESS REPORT

November 1989

Contract: 9-XG9-E9513-1

STI Control No.: 1737

EVALUATION OF SUPERCONDUCTING WIGGLER DESIGNS
AND FREE-ELECTRON LASER SUPPORT
MONTHLY PROGRESS REPORT
November 1989

Task 2.1 SPACE-BASED FEL WIGGLER DEVELOPMENT.

Further stability studies have been made. The earlier studies established the maximum current density by fixing the ratio of the peak hoop stress over distributed disturbance quench energy density. This ratio rapidly increases with currrent density once it has reached about 1000. Therefore, we established current limits by setting this ratio to be 1000. We have also examined two other ways of estimating the maximum allowable current. The first is to operate with a fixed difference between the bath temperature and the temperature at which ohmic heat generation starts. One rule of thumb is to set this at 1 deg. When this is used, the highest allowable current increases significantly at long wavelengths, but remains essentially unchanged at wavelengths below 3 cms. The long wavelength wigglers appear to be capable of large enough K, so this limit does not improve the short wavelength performance. If a quench is initiated by localized stick-slip conductor motion then the absolute amount of heat energy needed to propagate a normal zone which cannot be cooled down below the critical temperature sets a limit on the current density. We used 10^{-5} Joules as a limit. This did not affect the peak current. Therefore, the earlier maximum current estimates still hold. Further refinement appears to be in the realm of art and will await detailed engineering studies.

Support structure scaling needed to keep the wiggler halves from collapsing under magnetic attraction has been completed. The solution is to incorporate a small (ca. .5mm) stress relieving depression into a solid vacuumn tube which redistributes the attractive force out to the transverse edges of the vacuumn tube, away from the thin center section. Thus the added support structure weight due to attractive forces is simply the weight of a 1.5 lambda wide by the gap high rectangular piece of stainless steel.

Conductor sizing has been completed. Stability against flux jumps due to the self fields and transport current fields within a superconducting wire establishes an upper limit on the size of the wire. At 2 cm wavelength a 1 mm diameter wire is stable and at 10 cm wavelength a 1.6 cm diameter wire is stable. Fine multi-filament wires within the larger copper superconductor matrix are used to keep the interior of the wire from overheating when the magnet flux is changing during ramping of the current. Dynamic stability of these fine filaments sets a limit on their radii of 25 microns. The usual safety factor is about 2, so the fine superconducting filaments need to be about 15 microns in radius. These conductor dimensions are essentially standard within the industry.

Initial work has been started on analyzing quench performance vs wavelength. Preliminary calculations indicate that quenches would be quite long (3-5 seconds) due to the low inductance of the wigglers, so large voltages would not develop within the windings. Typical quench velocities appear to be 40 to 20 m/sec. Short wavelength wigglers have faster velocities. These factors appear to cause very large temperature rises within the windings. Initial calculations indicate that at the maximum current densities, that the windings could reach several thousand degrees kelvin. Several methods can be used to prevent these large temperatures. Quench analysis will be continued in the following month. Suitable protection methods will be determined.

With the small exception of the vacuumn tube weighting, the original mass estimate remains unchanged pending further cryogenic engineering studies.

Cryogenic issues such as superfluid cooling, lower temperature cooling and supercritical cooling will be examined. Emphasis will shift more towards engineering a specific point design.

Task 2.2 FEL ANALYSIS SUPPORT.

A study of the sensitivity to wiggler field errors and e-beam position sensing effors was completed during the performance period. The performance of various geometric arrangements of e-beam trajectory straighteners was compared for the parameters of the LSS design. Preliminary results were presented informally to Boeing and Los Alamos personnel on 9 November. Final results are documented in the attached memorandum.

Spectra Technology Memorandum

Date: 7 December 1989

To: Brian McVey, Distribution

From: Dave Quimby

Subject: Review of Wiggler Field Error Issues in the LSS Design

INTRODUCTION. The sensitivity of the LSS design to wiggler field errors and beam position sensing errors has been calculated previously by McVey [1]. That work included two-plane errors, but the e-beam trajectory correctors were modeled using the THUNDER-type coincident geometry. Since that time, improved models of the newer NISUS-type alternating corrector geometry have been developed [2,3]. It is anticipated that the NISUS-type geometry will be utilized in the LSS design. This work extends the modeling reported in references [2,3] to both transverse planes and the error sensitivities are then evaluated for the parameters of the LSS design.

SWOOP MODEL. Elliott's analytical treatment of e-beam trajectory correction schemes provides guidance as to the relative merit of various corrector geometries and predicts the optimum number of beam position monitors (BPMs) as a function of the error level [2]. The primary result is that the NISUS-type alternating geometry is predicted to provide much reduced BPM error sensitivity. Enhanced FEL performance is expected in cases where BPM errors are significant, but this benefit can be fully realized only at the expense of providing additional correctors.

Elliott measures the degradation of FEL performance due to field errors and beam position sensing errors in terms of the average angle squared of the e-beam centroid orbit. (Symbols are defined in Tables 1 and 2.)

$$\langle \overline{\theta^2} \rangle = 2\left(\frac{\sigma_x N_c}{Q_x L_w}\right)^2 + \frac{(\sigma_\theta^2)\gamma L_w}{6 Q_k^2 N_c} \qquad (1)$$

The orbit angle equation contains terms defining the contributions from BPM errors and field errors, respectively. The averages denoted by the angular brackets and the horizontal bar are taken over the axial extent of the wiggler and for the ensemble of possible random error distributions. The centroid angle squared is a useful figure of demerit since it is proportional to the dephasing of the electrons relative to the ponderomotive potential well of the FEL interaction. This dephasing is measured by the longitudinal coherence phase,

$$\langle \phi_{LC} \rangle = \frac{k_s L_w}{2} \langle \overline{\theta^2} \rangle \qquad (2)$$

which is one representative measure for the impact of field errors [4-6].

Table 1. Parameters Specified for LSS

Wiggler Length	L_w	14.9m
No. of Correctors	N_c	20
Field Errors	σ_K	≤ 0.005 ($\frac{1}{2}$% RMS)
BPM Errors	σ_x	≤ 0.006cm (60 μm RMS) (± 104 μm 1 plane box)
Spatial rate of increase of angular variance from field errors	$(\sigma_\theta^2)' = \frac{8}{\lambda_w}\left[\frac{K\sigma_K}{\gamma}\right]^2$	$= 3.38 \times 10^{-9}$ cm^{-1}
E-Beam Energy in units of rest mass	γ	196
Wiggler Period	λ_w	3.72 cm
Peak Wiggler Parameter	K	1.554
Optical Wavenumber	$k_s = 2\pi/\lambda_s$	5.93×10^4 cm^{-1}
Optical Wavelength	λ_s	1.06 μm

Table 2. Error Correction Quality and Cost Factors [2,7].

Correction Algorithm	Q_x	Q_K	Q_{1s}	C_{1s}
THUNDER-Type (T_1)	1.0	1.0	1.0	1.0
NISUS-Type, 1 Iteration (N_{13})	2.0	0.89	1.37	1.71
NISUS-Type, 2 Iteration (N_{-1135})	1.37	0.92	1.10	1.30

This analytical model can easily be generalized for the case of two-plane field errors. This requires a model for the distribution of BPM errors in the two planes. As shown in Figure 1(a), we have previously assumed that 1-plane BPM errors have been uniformly distributed within a box extending between +/-1.732 times the rms BPM error. For the specified maximum rms level of 60 microns, this corresponds to a +/-104 micron box. In extending this model to two planes, we have maintained the uniform distribution model as shown in Figure 1(b). The two-plane field errors are taken to be uniformly distributed within a pillbox of radius equal to 1.414 times the rms BPM error. In this memo it is assumed that the peak BPM errors remain within a box of radius 104 microns, so that the two-plane rms error is approximately 75 microns.

Generalization to two planes then leads to the following expression for the average orbit angular deviation,

$$\langle\overline{\theta^2}\rangle = 2\left(\frac{\sigma_x N_c}{Q_x L_w}\right)^2 + \frac{L_w}{6 Q_F^2 N_c}\left[(\sigma_{\theta x}^2)' + (\sigma_{\theta y}^2)'\right] \tag{3}$$

There is a particular number of correctors which minimizes the angular deviation. Differentiation of the equation reveals the straightest wiggler orbit operating point (SWOOP):

$$N_{cs} = L_w\left[\frac{(\sigma_{\theta x}^2)' + (\sigma_{\theta y}^2)'}{24\sigma_x^2}\right]^{1/3} C_{1s} \tag{4}$$

$$\langle\overline{\theta^2}\rangle_s = \frac{1}{2}\left[3\sigma_x^2\left[(\sigma_{\theta x}^2)' + (\sigma_{\theta y}^2)'\right]^2\right]^{1/3}\frac{1}{Q_{1s}} \tag{5}$$

Equation (4) is very useful for predicting how the required number of BPMs will scale for varying error levels. The SWOOP quality and cost factors are listed in Table 2. It is found that a NISUS-type correction geometry with 1 iteration has a 37 percent better average angle squared than a THUNDER-type correction algorithm, but requires 1.7 times the number of BPMs to achieve that level.

The impact of adding two-plane errors can be seen by examination of equation (3). Assuming an equal level of rms field errors in each plane, the field error contribution to the average trajectory angle squared is doubled. For uniform BPM box errors of a given peak amplitude, the contribution to the angle squared is increased by 1.5 times. According to equation (4), the net effect is only a 10 percent increase in the optimum number of correctors.

Figure 2 shows the predictions of the two-plane SWOOP model (eq. (3)) at the LSS specifications of 0.5 percent rms field errors and 75 micron rms BPM errors. For the THUNDER-type corrector geometry (called T(1) in the notation of ref. [2]), the optimum number of BPMs is about 25 and the minimum (a.) Single Plane

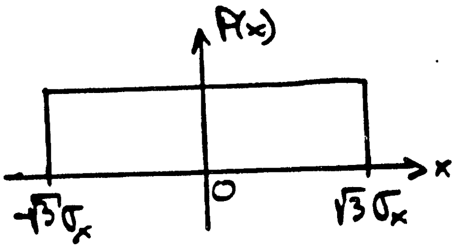

σ_x = RMS error

(b.) Two Planes

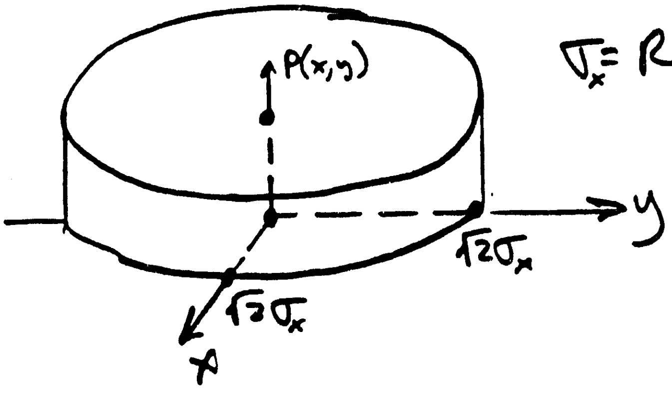

σ_x = RMS error

Figure 1. Comparison of uniformly-distributed BPM error models for (a) single plane and (b) two planes. For 60 μm RMS errors in one plane, the box extent is ± 104 μm. For 104 μm pill box in two planes, the RMS error is ~75 μm.

(a) THUNDER-TYPE CORRECTORS (T_1)

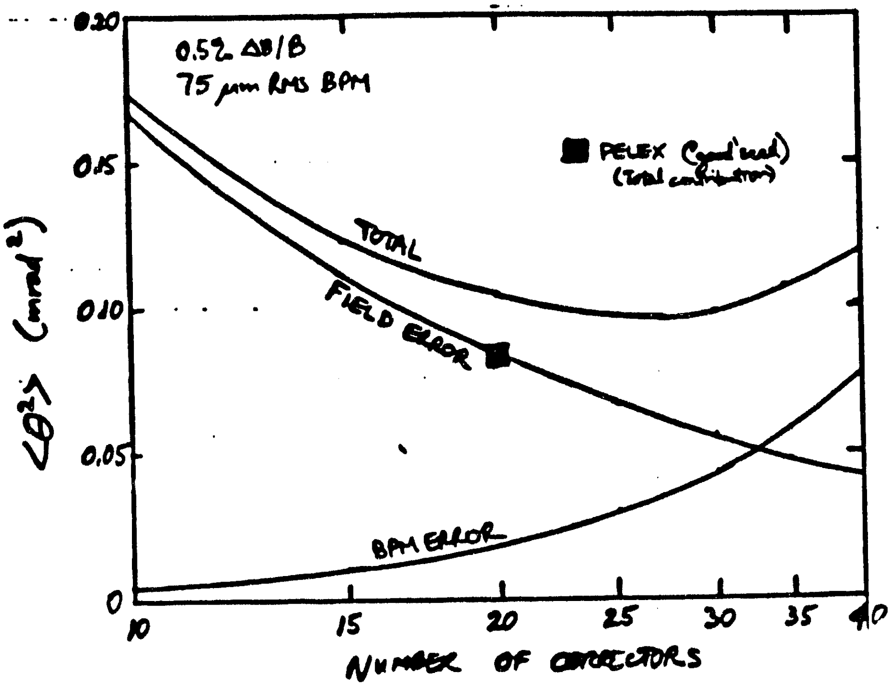

(b) NISUS-TYPE CORRECTORS, 1 Iteration (N_{13})

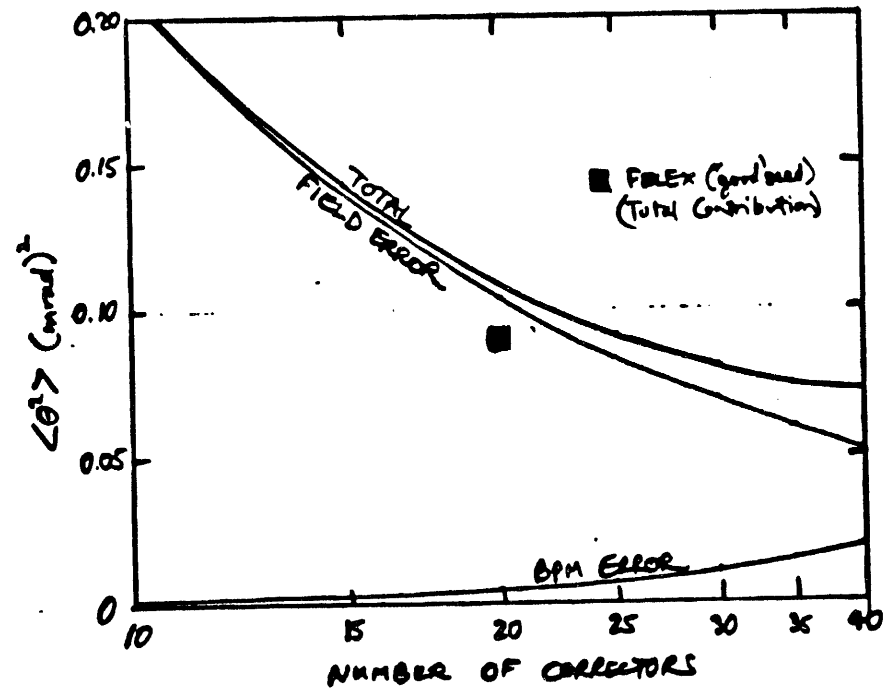

Figure 2. E-beam orbit angular deviation due to two-plane field errors and BPM errors as predicted by the SWOOP analytic model for various corrector geometries. Numerical results shown by the dark boxes.

trajectory wander is about 0.1 mrad**2, in agreement with equations (4) and (5). For the NISUS-type corrector geometry with 1 iteration (N(13) in SWOOP notation), the BPM error contribution is much smaller, leading to an optimum number of BPMs near 40. In both cases, however, the optimum is very broad. In fact, similar performance is predicted for each algorithm at the present LSS specification of 20 BPMs. According to the scaling of Equation (4), 20 BPMs would be optimum for the NISUS-type algorithm with one iteration if the field error level was 0.3 percent rms and the BPM error level was about 125 microns rms. Another notable feature is that for the present specifications, the performance degradation can be expected to be dominated by field error effects; BPM errors at the 75 micron rms level (104 microns peak) have minimal effect.

In an effort to compare the numerical and analytical models, the theta-squared quantity was computed from a couple of FELEX runs; results are shown by the dark boxes in Figure 2. The numerical calculations fall somewhat below the analytical predictions, but this can be explained by the fact that the numerical calculations used a particularly good random number seed which tends to minimize the trajectory angles. It is believed that the deviation from the mean is representative of what can be expected for a particular random error distribution.

MULTIPLE ITERATIONS. It is shown in reference [3] that the NISUS-type geometry has the additional feature that multiple iterations are useful in cases where the field error contribution dominates over the BPM error contribution. Quality and cost factors (Table 2) for the analytic model have recently become available [7] for the case of the NISUS-type alternating geometry with 2 iterations (called N(-1135) in ref. [2]). Several numerical calculations have been completed in an effort to compare with the SWOOP analytical model for this correction algorithm. Results are shown in Figure 3 for the case of 0.5 percent rms two-plane field errors and 75 micron rms BPM errors. The error bars denote the variance for two particular random number seeds yielding large and small angular trajectory deviations.

The theta-squared quantity is minimized at around 30 BPMs for the 2 iteration case. This correction algorithm has characteristics intermediate to the THUNDER-type and NISUS-type algorithm with one iteration. In particular, the sensitivity to BPM errors remains less than that experienced by the THUNDER-type scheme. Again, it appears that the performance of each of the three schemes will be comparable with 20 BPMs.

OPTIMUM NUMBER OF BPMs. The SWOOP model predicts that, for the specified maximum allowable error levels, performance is optimized with about 25, 30, or 40 BPMs for the THUNDER-type corrector geometry, the NISUS-type geometry with 2 iterations, or the NISUS-type geometry with 1 iteration, respectively. Figure 4 shows comparable results obtained with the FELEX numerical model. The results are in general agreement with the SWOOP predictions, at least in some respects. In particular, the numerical model predicts performance optimums at the expected number of BPMs for the THUNDER-type geometry and for the NISUS-type corrector geometry with 1 iteration. FELEX predicts a broad optimum in the 20-30 BPM range for the NISUS-type corrector geometry with two iterations.

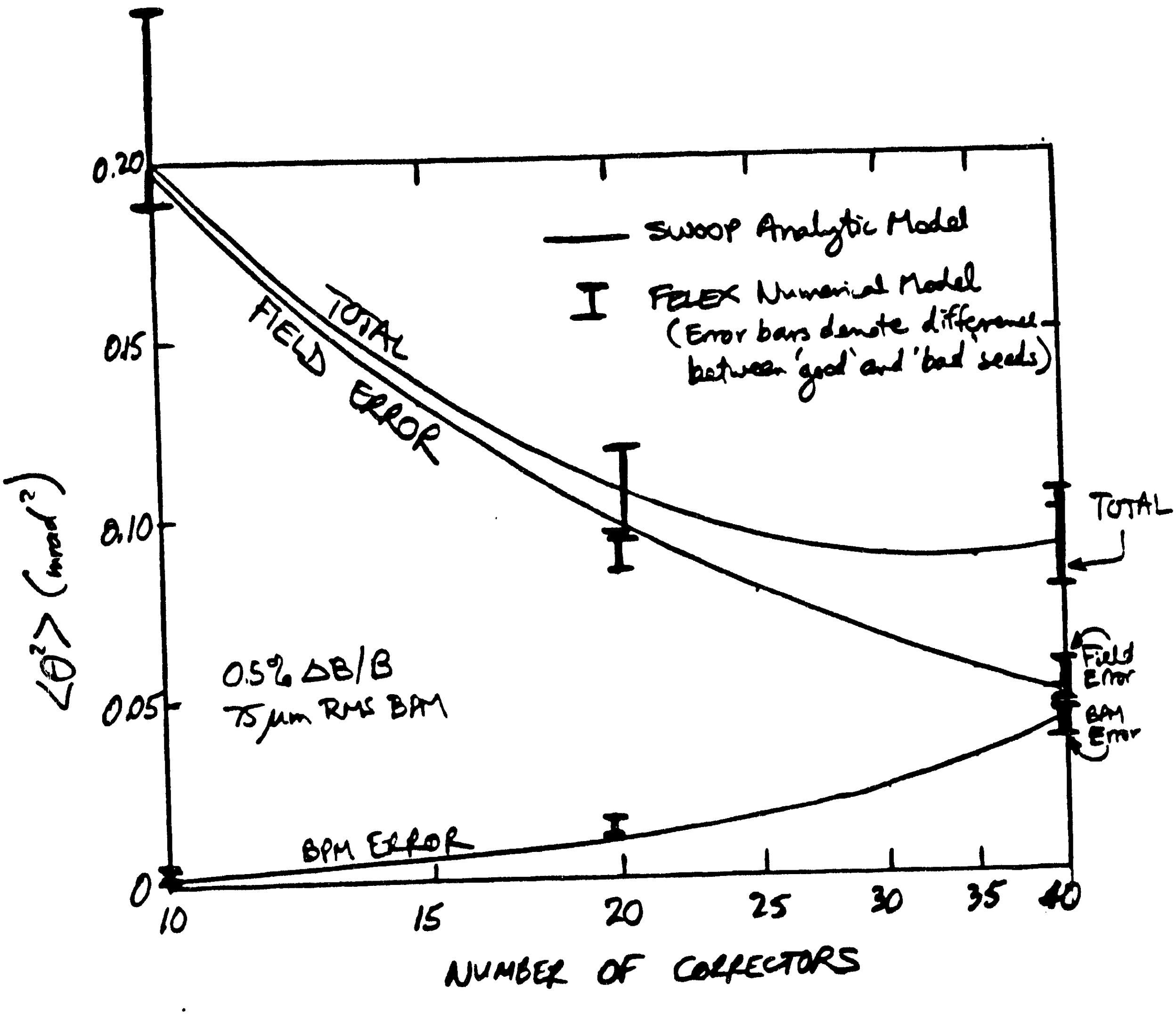

Figure 3. Comparison of numerical and analytical evaluations of $\langle\theta^2\rangle$ for the NISNS-type correction scheme with two iterations. This correction algorithm has characteristics intermediate between the T_1 and N_{13} schemes.

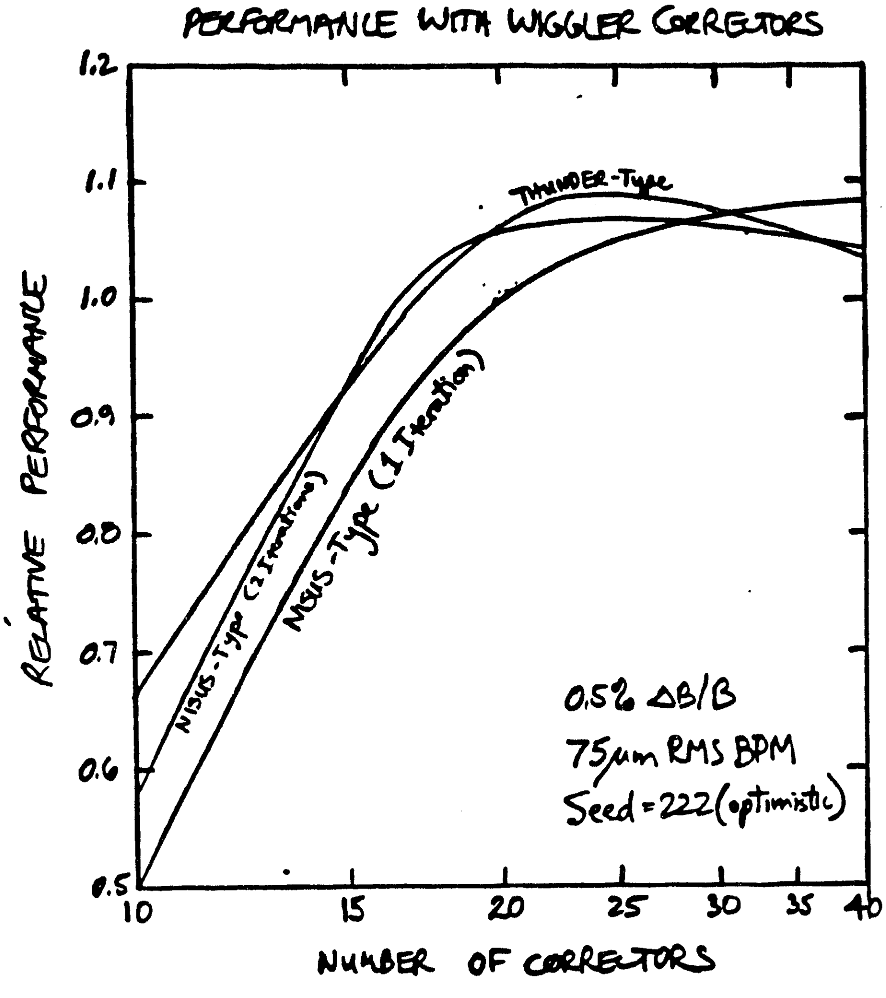

Figure 4. Performance variation with the number of correctors as calculated numerically with the FELEX code shows general agreement with the predictions of the SWOOP analytical model.

A notable disagreement with the SWOOP model is also found in Figure 4. The relative performance at the optimum number of BPMs is measured by the Q(1s) quality factor listed in Table 2. SWOOP predicts that, when compared to a THUNDER-type algorithm, the NISUS-type corrector geometries with 1 and 2 iterations should have 37 percent and 10 percent lower theta-squared values, respectively, at the optimum number of BPMs. However, Figure 4 shows that the lower theta-squared does not translate directly into higher FEL performance in these cases. Evidently other factors, such as the spatial distribution of the trajectory errors, also plays a role in determining the actual performance.

Performance is measured here in terms of relative power output. The output power is normalized in such a way that a relative value of 1.00 corresponds to 108 percent of the specified LSS power requirement. The conversion between the calculated single wavefront output power to estimated optical pulse energy is completed using standard approximations which have been verified with pulse calculations.

The numerical results shown in Figure 4 are obtained with a particular seed for the random number generator used to produce the random error distribution. We will see later that the seed used here is a somewhat optimistic choice in that it gives performance levels somewhat higher than average for a given level of rms errors.

Figure 4 shows that the NISUS-type system with a single iteration, N(13), does a relatively poor job of correcting large field error levels if only 20 BPMs are utilized. It is hampered because the number of correctors is much less than optimum for this scheme. As shown previously, the SWOOP analytical model predicts that this scheme would be more nearly optimum if the field error level was 0.3 percent rms and the BPM error level was about 125 microns rms. Figure 5 explores the relative performance of the various schemes with these rms error levels. As expected, the performance of the N(13) scheme optimizes near 20 correctors in this case. However, the optimum number of BPMs for the THUNDER-type correction algorithm and NISUS-type system with 2 iterations does not decrease as much as expected.

RANDOM NUMBER SEEDS. The SWOOP analytical model predicts the average characteristics of an ensemble of all the possible random wiggler field error distributions. On the other hand, a numerical model, such as FELEX, models individual possible wiggler realizations, one at a time. Different random error distributions are generated using various random number seeds. Table 3 shows that considerable variability is found between possible wiggler error distributions with the same rms error level. At the specified maximum allowable LSS error level, the variation in output power for different wiggler realizations has a standard deviation of approximately 10 percent.

The envelope of the electron beam trajectory is shown for two different error distributions in Figure 6. The two plots are for equal rms error levels, but random error distributions with differing performance levels. Visual inspection of the trajectories does not yield any obvious explanation for the differences. However, diagnosing the trajectories in terms of the average angle squared does generally show that poorer performance correlates with larger average trajectory deviation. In the examples shown in the figure, the longitudinal coherence phase for the random number seed with poor performance is 5.2 radians, compared to 3.9 radians for the good seed.

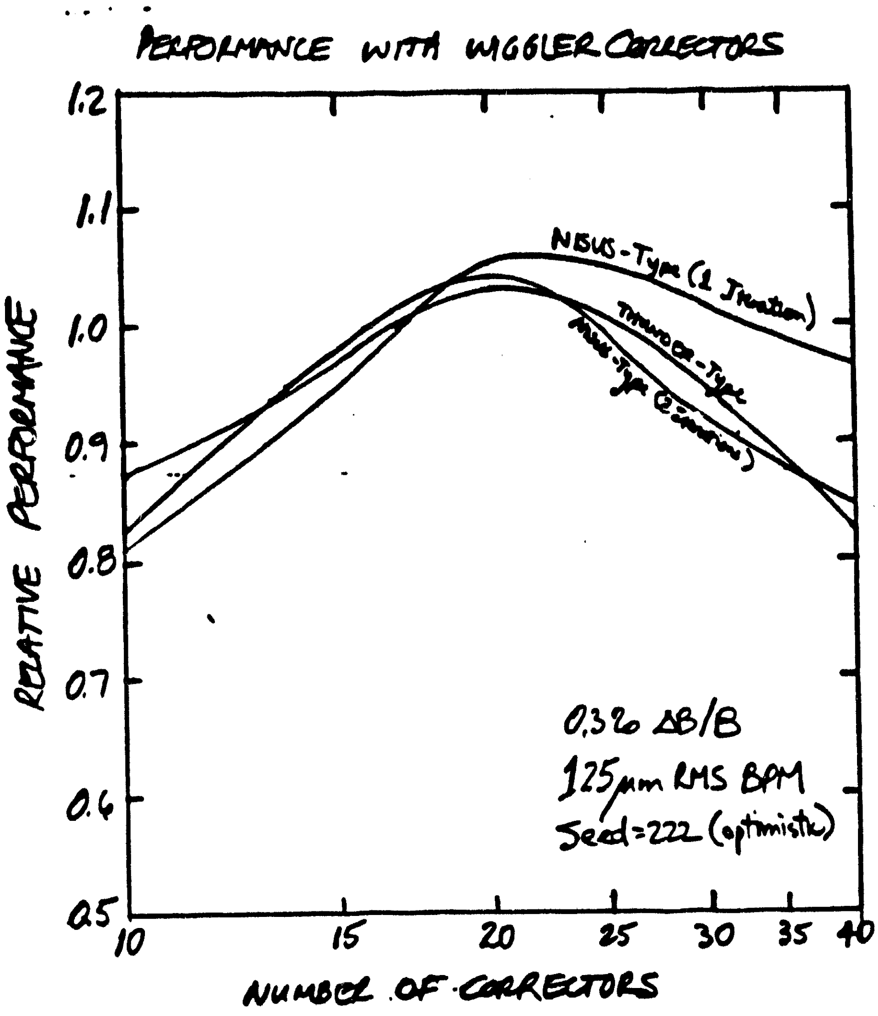

Figure 5. Performance variation with the number of correctors in a case where BPM errors are more important.

Table 3. Considerable variation is observed between random number seeds. Calculations completed for 0.5% RMS field errors, 75 μm RMS BPM errors, NISUS-type correctors with 1 iteration, and 320 axial steps.

Seed	RELATIVE OUTPUT POWER
111	0.880
222	1.000
333	0.778
444	0.932
555	0.981

Average = 0.914
Stand. Dev. = 0.089

Figure 6. Comparison of e-beam trajectories for different random number seeds reveals that larger $\langle\theta^2\rangle$ generally means poorer performance.

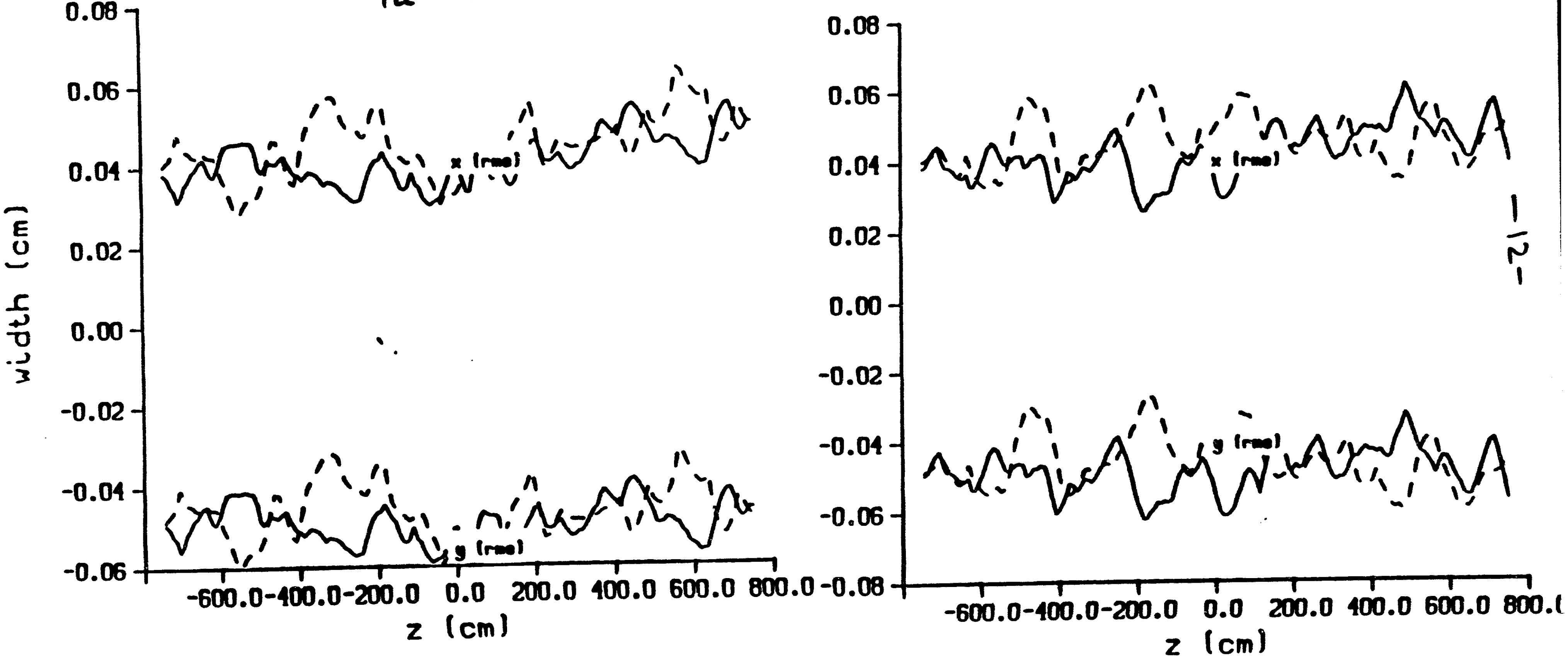

'GOOD' SEED (222)
$\langle\theta^2\rangle = 0.089\ \mathrm{mrad}^2$
$\phi_{LC} = 1.24\pi$

'BAD' SEED (333)
$\langle\theta^2\rangle = 0.118\ \mathrm{mrad}^2$
$\phi_{LC} = 1.65\pi$

0.5% ΔB/B
75μm RMS BPM
Nisus-Type, 2 Iterations

Table 4 examines the performance of various random number seeds when different field error correction schemes are applied. It is found that a seed which provides typical performance with one corrector scheme also provides typical performance for other corrector schemes. On the basis of the results of Table 4, seed 111 was chosen as the standard seed for this study; it tends to produce fairly average, but slightly pessimistic results, and is therefore a somewhat conservative choice.

It should be noted that the performance of a given seed was also found to be sensitive to the choice of axial grid size. This is because the use of a different step size causes the various random field error kicks to be redistributed relative to the position of the fixed corrector locations. Thus changing the axial grid size actually leads to a new wiggler field error distribution. To avoid erroneous results from these effects, care was taken to maintain a constant number of axial grid steps as the number of correctors was varied (Figures 4,5).

FIELD ERROR SENSITIVITY. A field error sensitivity study has been completed for the LSS parameters listed in Table 5. In all cases, the performance of NISUS-type correctors is compared to the THUNDER-type corrector case. Note that misalignments have been neglected for the purposes of this study.

Figure 7 shows the calculated sensitivity to BPM errors with 20 correctors and an rms field error level of 0.5 percent. Figure 8 shows corresponding results for the case of 0.3 percent rms field errors. Performance is again measured in terms of the relative output power as calculated with multipass simulations using FELEX. These curves show little incentive for achievment of BPM accuracies better than the specified level of 75 microns rms.

As expected, it is found that the NISUS-type correction is best applied differently depending on the level of errors present [3]. Two iterations are used for the case of small BPM errors or large field errors. Experimentally this would be done by zeroing the currents in all correction coils, then sweeping through the correction algorithm (first iteration) and measuring FEL performance. After application of a second iteration of the correction algorithm, the FEL power would then be remeasured. Whichever set of current settings gives the best performance should then be used. The best choice is highlighted in the figures by the heavy dark line. For 0.5 percent rms field errors (Figure 7), 2 iterations are used for all levels of BPM errors less than 200 microns rms. For 0.3 percent rms errors (Figure 8), 2 iterations are used for BPM errors of less than 120 microns rms. It appears that for the specified level of BPM errors (<75 microns), 2 iterations of the NISUS-type corrector algorithm would best be used (with the exception of the possible case of extremely small field error levels).

The sensitivity to field errors for the cases of 75 micron and 125 micron rms BPM errors is shown in Figures 9 and 10, respectively. With 20 BPMs, NISUS-type correctors give nearly equivalent performance or better than THUNDER-type correctors under all conditions. The real advantage of the NISUS-type correctors is reduced sensitivity to large BPM errors, but this effect is only evident for BPM errors greater than about 125 microns rms, a value which is considerably larger than the specified level (< 75 microns).

Table 4. The relative performance of different random number-seeds seems to be insensitive to the choice of corrector scheme. Calculations are for 0.5% RMS field errors and 75 μm RMS BPM errors.

SEED	RELATIVE EXTRACTION @ Fixed 1GW input Power		
	THUNDER-Type	NISUS-Type (1 Iteration)	NISUS-Type (2 Iterations)
111	0.960	0.903	0.967
222	1.011	1.000	1.027
333	0.939	0.855	0.926
444	0.919	0.922	0.946
555	0.966	0.999	1.019
	0.959 ± 0.034	0.936 ± 0.063	0.977 ± 0.044

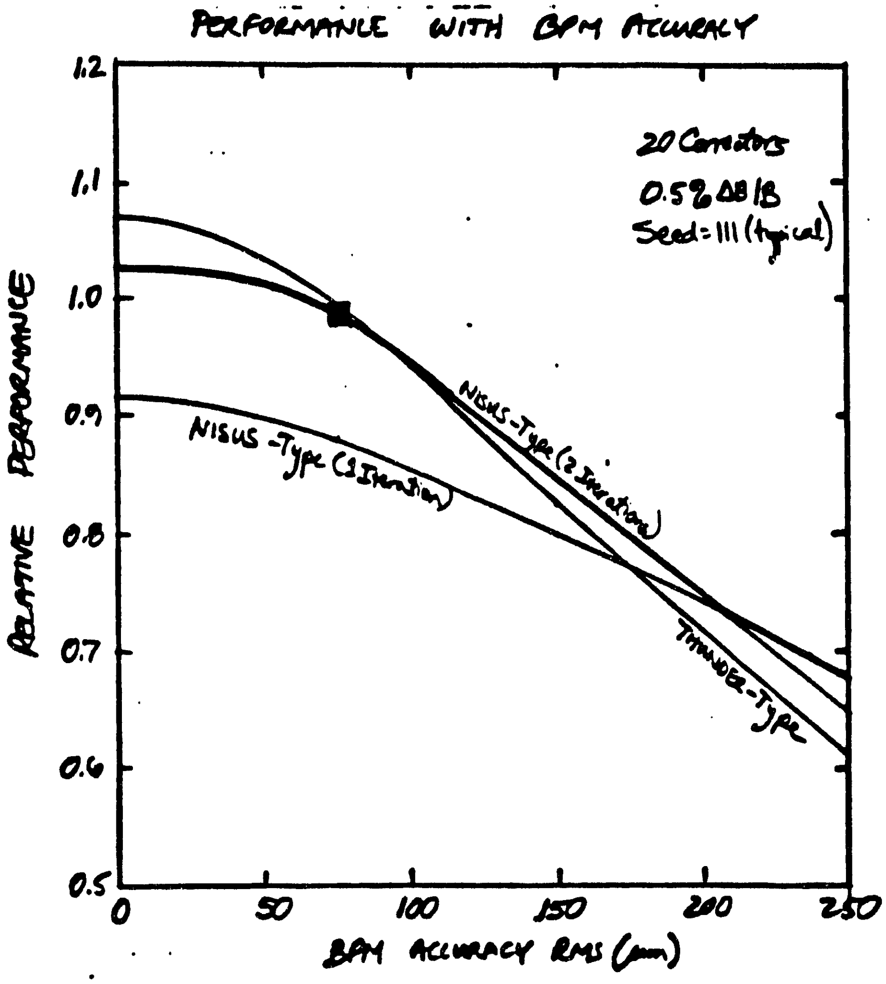

Figure 7. Sensitivity to BPM accuracy for 0.5% RMS field errors. There appears to be little incentive for BPM accuracy better than 75 μm RMS (104 μm radius error circle).

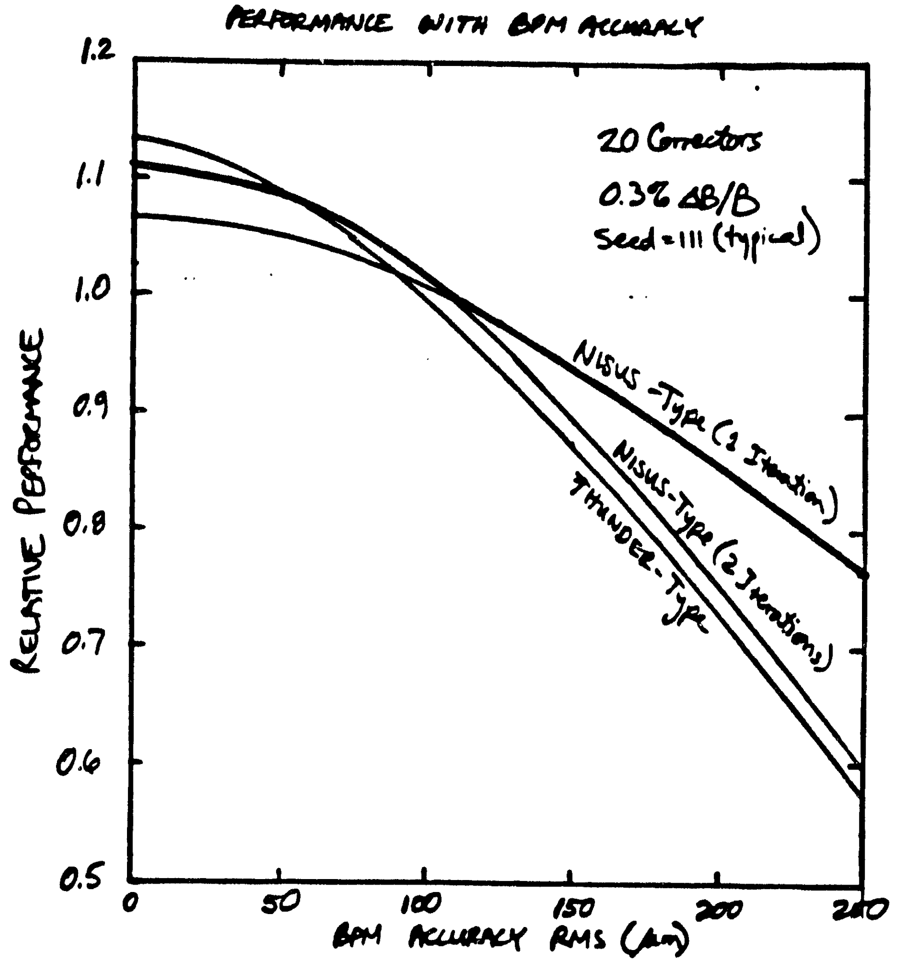

Figure 8. Sensitivity to BPM accuracy for 0.3% RMS field errors.

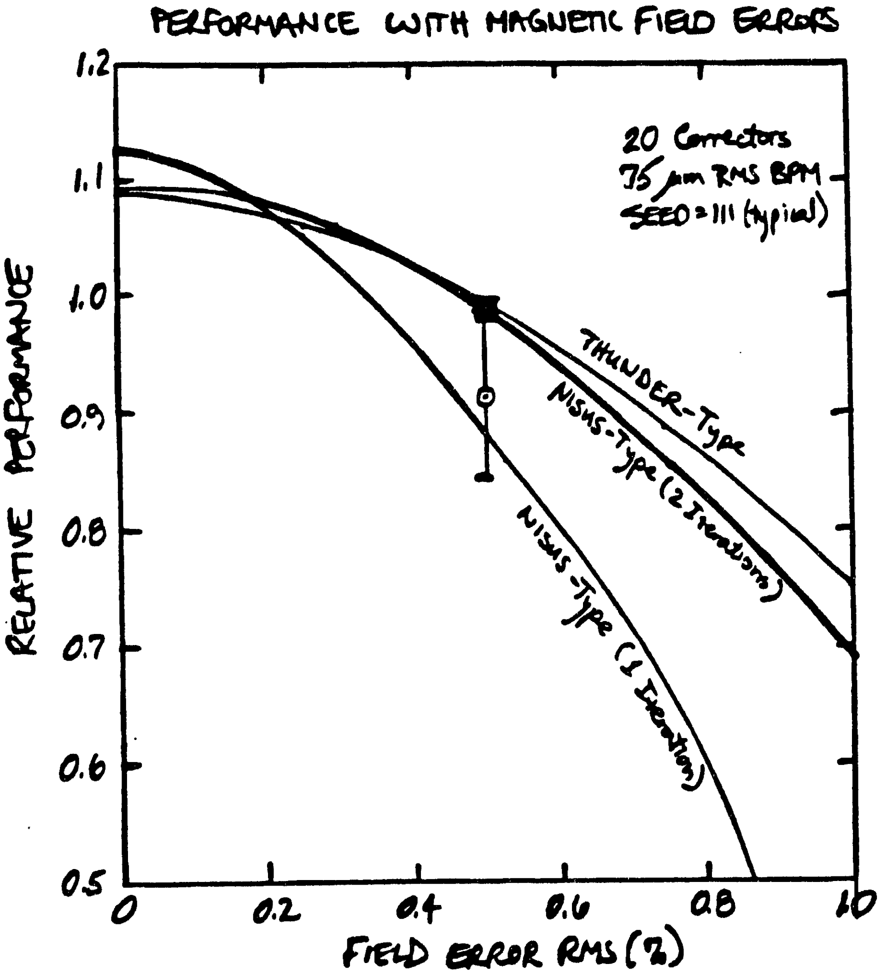

Figure 9. Sensitivity to field errors for 75 μm RMS BPM errors. Achievement of field error levels better than 0.5% RMS has a noticeable potential benefit. The error bars denote one standard deviation for 10 trial random error distributions in the NISUS-type corrector case with 1 iteration.

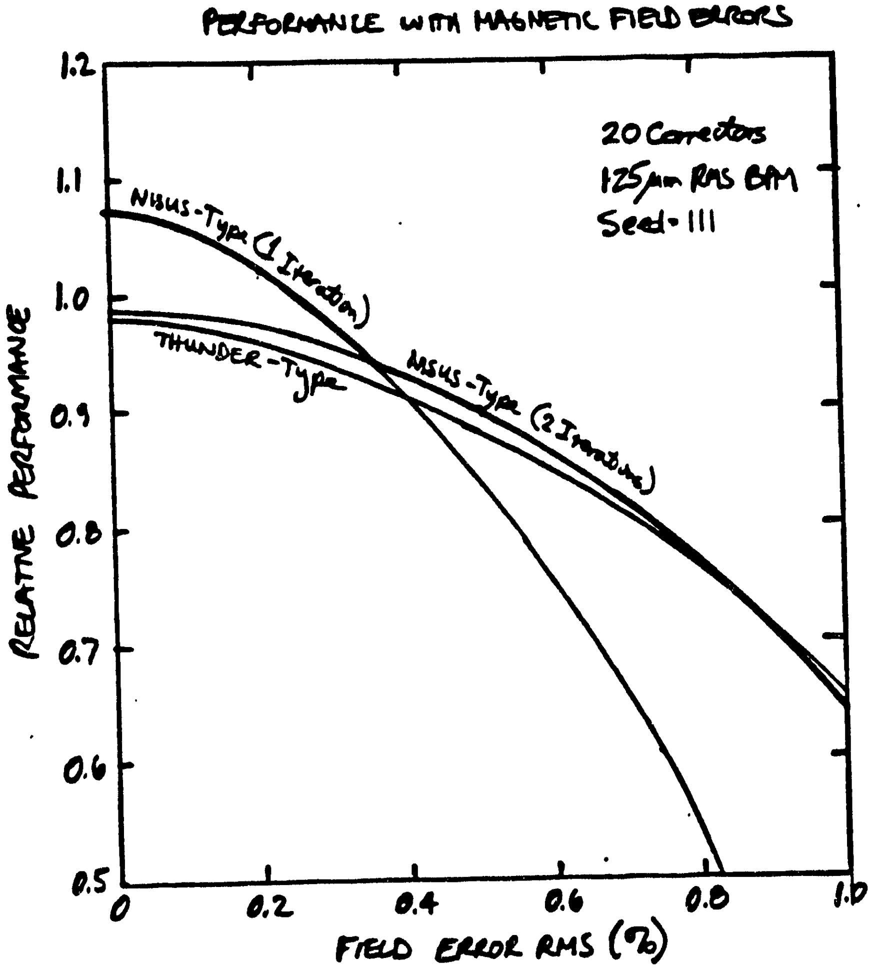

Figure 10. Sensitivity to field errors for 125μm RMS BPM errors (175μm radius error circle).

Table 5. Standard LSS Parameters

Quantity	Standard Value	Comment
E-BEAM:		
Resonant Energy	100 MeV	
Peak Current	480 A	
Micro.-Avg. Current	384 A	Used for single wavefront calcs.
Energy Spread	1 percent	Gaussian distrib., 90% particles
Norm. Emittance	57 pi mm-mrad	Gaussian distrib., 90% particles
Radius	0.67 mm	Edge radius, 90% particles
Betatron Period	9.5 m	
Misalignment	None	
Mismatching	None	
WIGGLER:		
Overall Length	14.9 m	
Period	3.72 cm	
Peak Field	4.47 kG	
Aw (rms)	1.099	
Resonant Wavelength	1.06 microns	
Resonant Energy Taper	8.9 percent	
Taper Prescription	Nonlinear	Provided by B. McVey
Clear Aperture	1.152 cm	
Vac. Tube Ellipticity	2:1	
Prebuncher	None	
OPTICAL CAVITY:		
Resonant Wavelength	1.068 microns	
Design Rayleigh Range	5.0 m	
Waist Radius	1.30 mm	1/e**2 intensity point
Misalignment	None	
Mode Matching	Mirrors despaced	Provided by B. McVey

Figure 9 shows that achievement of field error levels better than the maximum allowable 0.5 percent rms would lead to noticeable potential benefits. Approximately 10 percent better performance would be possible if the field errors were to satisfy an rms level of about 0.2 percent. The possible variability in various wiggler error distributions is also represented by the error bars shown in the figure for the case of NISUS-type correctors with 1 iteration.

CONCLUSIONS. The available analytical and numerical tools for providing field error correction guidance have been applied to the LSS parameter set. The SWOOP analytical model is useful for predicting the optimum number of BPMs and comparing the efficacy of various corrector configurations. The FELEX code quantifies the actual performance degradation. It is found that the performance of the NISUS-type correctors to be used in LSS is equivalent to or better than that of THUNDER-type correctors for the range of parameters of interest. For the present specified maximum allowable levels of field errors and BPM errors, field error effects dominate the performance loss. This implies that two iterations should be applied to the NISUS-type corrector algorithm. With 20 BPMs active along the 15 m wiggler length, the correction is quite good, providing power output which is expected to be within approximately 10 percent of what is theoretically possible without field errors.

At the present specified error level, the optimum number of BPMs is somewhat greater than 20, but the potential performance improvement is slight. One possible motivation for increasing the specified number of BPMs would be for performance recovery after potential field quality degradation from radiation damage. If achievement of the specified BPM accuracy is considered to be a higher risk than maintaining compliance with the field error specifications, there is no incentive for increasing the number of BPMs.

Work in this area is expected to continue over the next several months. The impact of mechanical errors such as wiggler misalignments and gap setting errors will be used to help establish mechanical tolerances. The impact of field errors on performance enhancement schemes such as the prebuncher and dynamic taper may also be examined. At some point it would also be useful to examine how error sources impact the micropulse dynamics. In particular, the performance rolloff with errors as calculated by single wavefront and full pulse calculations should be compared; it may be that the rolloffs are actually somewhat steeper that estimated here because errors may cause less of the micropulse to lase.

REFERENCES

[1] B. McVey, "Phase 1A Oscillator Sensitivities," memo dated 5 July 1989.

[2] C.J. Elliott and D.C. Quimby, "Analytical Treatment of Electron Trajectory Straightener Issues in Free-Electron Lasers," presented at the Eleventh International Conference on Free Electron Lasers, Naples, FL, 28 August-1 September 1989, to be published in Nucl. Instr. and Meth. (1990).

[3] D.C. Quimby and C.J. Elliott, "Numerical Treatment of Electron Trajectory Straightener Issues in Free-Electron Lasers," presented at the Eleventh International Conference on Free Electron Lasers, Naples, FL, 28 August-1 September 1989, to be published in Nucl. Instr. and Meth. (1990).

[4] C.J. Elliott and B. McVey, "Analysis of Undulator Field Errors for XUV FELs," in Undulator Magnets for Synchrotron Radiation and Free Electron Lasers, Symposium in the Adriatico Conference Series, Trieste, Italy, 23-26 June 1987 (World Scientific, Teaneck, NJ).

[5] B. Bobbs, G. Rakowsky, P. Kennedy, R. Cover, and D. Slater, "In Search of a Meaningful Field Error Spec for Wigglers," presented at the Eleventh International Conference on Free Electron Lasers, Naples, FL, 28 August-1 September 1989, to be published in Nucl. Instr. and Meth. (1990).

[6] S.C. Gottschalk, D.C. Quimby, K.E. Robinson, and J.M. Slater, "Wiggler Error Reduction through Shim Tuning," presented at the Eleventh International Conference on Free Electron Lasers, Naples, FL, 28 August-1 September 1989, to be published in Nucl. Instr. and Meth. (1990).

[7] C.J. Elliott, "Wiggler Field Error Lottery Heuristics and Strategies," presented to Los Alamos National Laboratory, 30 November 1989.

Distribution:

Boeing - Denis Pistoresi, John Adamski, Bob Papadopulos
LANL - Brian McVey, Les Thode, Jim Elliott
STI - Jack Slater, Steve Gottschalk, Kem Robinson, file (STI 1737).

MONTHLY PROGRESS REPORT

December 1989

Contract: 9-XG9-E9513-1
STI Control No.: 1737

EVALUATION OF SUPERCONDUCTING WIGGLER DESIGNS AND FREE-ELECTRON LASER SUPPORT

Monthly Progress Report
December 1989

INTRODUCTION

Scaling studies of quench dynamics have been started. Quench times increase with wavelength; temperature rise during a quench is typically 50-100°K and inductive voltages within the windings are several kilovolts.

DISCUSSION

Earlier quench calculations were in error. These used a misprinted equation for the quench time. After correction of the equation, the new quench behavior is much more benign.

A full analysis of quench dynamics is beyond the scope of this study, but factor of two estimates can be made. It is useful to examine the behavior of an unprotected wiggler during a quench. The longer wavelength wigglers take longer to quench, have a small temperature rise, but may or may not have a larger voltage within the windings.

Quench times are determined by estimating how long it takes before the i^2*R losses in the growing ellipsoidal normal zone become equal to the stored magnetic energy. This requires estimates of the growth rate and shape of the normal zone. A quench zone is ellipsoidal because the quench proceeds very rapidly along the wires due to the high thermal conductivity of the copper stabilizer, but moves very slowly across turns due to the poor thermal conductivity of the insulator. Since long wavelength wigglers have a much higher stored energy, due to higher magnetic fields and large volumes, the quench time increases with wavelength. Despite a complex dependance on several different factors, the overall quench time scales linearly with wavelength. A different method of setting the maximum current density would give a different wavelength scaling for the quench time.

Peak temperature rise during a quench is found by equating the ohmic heat generation per unit volume of winding to the temperature rise times the volumetric specific heat. By integrating the heat generation during a quench it is possible to estimate the temperature rise. The copper performs the added function of stabilizing temperature rises during a quench because of it's high heat capacity. The increased quench times for longer wavelength lead to lower temperature rises. However, none of the wavelengths showed any tendencies towards temperatures in excess of 200° K.

The winding voltage, Ldi/dt, is controlled by the wire size and the quench time. Longer wavelength wigglers allow larger diameter wires, i.e. larger currents, but require fewer turns per racetrack leading to a lower inductance, $2*\text{energy}/i^2$. The overall voltage scaling with wire size is then 1/wire size. As noted in the December report, the longer wavelength wigglers permit larger wires before flux jumping causes the wires to be unstable. While increasing the wire size does reduce quench voltages, there may be a penalty for space applications since increased charging currents imply larger, heavier power supplies. In addition, the current lead power dissipation during charging increases with current requiring a larger refrigeration capacity for space applications. Thus, in order to minimize the weight of a space based wiggler while maintaining the option of recharging the wiggler in space, a smaller wire size with lower currents is desirable. This has an impact on the use of an external dump resistor for quench protection.

For the wiggler designs being studied, the temperature rises during a quench remain below 200° K and the voltages stay below a few kilovolts. Quench protection seeks to limit both temperature rise and winding voltage. The magnetic energy can be dissipated through an external dump resistor thereby minimizing cryogen boiling and pressure rises; or it can be dissipated internally via coupled secondaries or subdivided windings with shunt resistors. For a lightweight wiggler, reducing pressure during a quench leads to a reduction in cryostat mass, but to maintain reasonable dump resistor voltages during the quench requires larger superconducting wires, which leads to a more massive charging system. This weight trade will be quantified in the next reporting period.

Another method of quench protection is the use of a coupled secondary. This is quite effective at reducing quench voltages and currents provided that the secondary is tightly coupled with the superconducting windings. The geometry of the present wiggler design has no room for extra windings, but the vacuum tube and the holmium may couple inductively during a quench due to induced eddy currents. This has been observed in solenoids wound on aluminum cylinders. The quench is further enhanced by a process known as quench back wherein the secondary heats up causing the normal zone to grow faster reducing both the quench time and the quench voltage. This process is quite complex, so only rough estimates can be made. It does require a stronger cryostat since all the magnetic energy is dissipated in boiling the cryogen. Mass estimates for this protection method will be made in the next reporting period.

There are refinements in quench estimates due to the presence of boundaries. In general, boundaries increase the temperature rise since a smaller volume of material is being heated; but they also lengthen the quench time leading to a smaller di/dt which gives lower quench voltage. For the FEL wigglers, the rapidly increasing enthalpy of the copper in the superconducting wire helps to minimize the additional temperature rise. The main effect of boundaries is to reduce the winding voltages by a factor of three. In a wiggler, the holmium backplane and the vacuum tube limit the quench volume. The holmium poles may also limit the volume. If the racetrack coils are wound in series, the quench can proceed from racetrack-to-racetrack along the conductor. The above mentioned boundaries limit the quench in the direction transverse to the current flow. This is called a quench which is bounded in two dimensions.

The remainder of this progress report summarizes quench scaling laws. The boundary limited quench behavior is more complex, so it is only presented in tabular form.

QUENCH SCALING RELATIONS

The quench propagation velocity of fully impregnated winding without cooling channels is:

$$v = \frac{J_{av}}{(\gamma C)_{av}} \left\{ \frac{L_o \, \theta_s}{\theta_s - \theta_o} \right\} \tag{1}$$

$(\gamma C)_{av}$ = averaged volumetric heat capacity (2)

= 8060 w/m^2-°K @ 2 cm

= 6900 w/m^2-°K @ 10 cm

J_{av} = average current density in windings (3)

L_o = Lorentz number = 2.45×10^{-8} $w \, \Omega \, k^{-2}$ (4)

$\theta_s = (\theta_g + \theta_c)/2$ (5)

θ_g = temperautre at onset of ohmic heating at J_{av} (6)

θ_c = critical temperature at peak magnetic field but zero current (7)

A table of quench velocities is given below

λ(cm)	v(m/sec)
2	37.7
4	26.1
6	20.4
8	17.2
10	14.6

The lower J_{av} at longer wavelengths reduces v. Quench propagation across turns is lower due to insulation. The slower quench speed is 3.0×10^{-2} v for a 1.5:1 Cu:Sc winding at all wavelengths:

$$\frac{v_{transverse}}{v_{longitudinal}} = \alpha = 3 \times 10^{-2} \tag{8}$$

The quench time is:

$$T_Q = \left\{ \frac{180\ E\ U_o^2}{4\pi\ J_{av}^6\ \rho_o \alpha^2 v^3} \right\}^{1/6} \tag{9}$$

U_o = constant related to volumetric specific heat and resistivity at quench temperature

ρ_o = copper resistivity averaged over a winding at quench temperature

= 8.1×10^{-9} Ωm

E = stored magnetic energy from PANDIRA

Stored energy scaling is:

$$E \alpha B^2 V$$

$$B \alpha \sqrt{\lambda}\ J_{av} \tag{10}$$

$$V \alpha \lambda L$$

L = length of wiggler

= 1 m

$$E \alpha \lambda L J_{av}^2$$

$$T_Q = 8.9 \times 10^5 \frac{\lambda^{1/2} L^{1/6}}{J_{av}^{2/3} v^{1/2}} \tag{11}$$

A table of T_Q and E is:

λ	E(J)	T_Q(sec)
2	3100	0.023
4	9700	0.054
6	18,000	0.092
8	27,500	0.134
10	36,800	0.184

The maximum temperature rise during a quench is:

$$\theta_m = J_{av}^{\;4} \; T_Q \left[\frac{\theta_o}{U_o^2}\right] \tag{12}$$

$$\theta_o = 100°K \tag{13}$$

using the scaling of (11) for T_Q gives:

$$\theta_m = 1.8x10^{-19} \; \frac{J_{av}^{\;8/3} \; \lambda \; L^{1/3}}{v} \tag{14}$$

Finally, the maximum winding voltage is:

$$V_m \simeq \frac{2LI}{T_Q} \tag{15}$$

L = inductance of wiggler (16)

$= 2E/I^2$

$$I = J_{av} A \tag{17}$$

A = area of supercon wire (18)

I = Current in supercon wire (19)

$$V_m = 2.6 \times 10^{-15} \frac{v^{1/2} \lambda^{15/6} L^{5/6} J_{av}^{10/6}}{A} \tag{20}$$

A table of $T_Q(\lambda)$, $\theta_m(\lambda)$, and $V_m(\lambda)$ is:

λ(cm)	T_Q (sec)	θ_m(°K)	V_m(volts)
2	0.023	57	640
4	0.054	47	1400
6	0.092	41	2100
8	0.134	36	2700
10	0.184	32	3100

Boundary effects reduce V_m, increase θ_m and T_Q. The results are:

λ	T_Q (Boun)/T_Q (sec)	θ_m (Boun) (°K)	V_m (Boun) (volts)
2	1.8	180	230
4	1.6	120	560
6	1.5	95	860
8	1.5	80	1200
10	1.4	45	1400

All values for V_m used A=1 mm² = 10^{-6} m². The scaling of (20) can be used to find V_m at other wire sizes. The value of 1 mm² is the flux jump limit at a wavelength of 2.0 cm. The flux jump limit at 10.0 cm is $A = (17 \text{ mm})^2 = 300 \times 10^{-6} \text{m}^2$.

CONCLUSION

Scaling laws for quench time, Equation (11); temperature, Equation (14) and voltage, Equation (20) have been determined. Quench protection with a dump resistor vs coupled secondary requires further study to determine the mass trade-offs.

MONTHLY PROGRESS REPORT

March 1990

Contract: 9-XG9-E9513-1
STI Control No.: 1737

EVALUATION OF SUPERCONDUCTING WIGGLER DESIGNS AND FREE-ELECTRON LASER SUPPORT

Monthly Progress Report
for Period Ending March 1990

This Month's Work

Effort has focussed on exploring the extraction and average current benefits of superconducting and wedged pole hybrid wigglers. Superconducting wigglers show 90% higher extraction, 35% lower average current and 15% lower beam energy. The wiggler length, output power and single pass saturated gain were held fixed.

Resistive wall heating must be reduced. A superconducting NbTi liner in the vacuum tube can reduce the wall heating from 300 W/m to 0.02 W/m.

Next Reporting Period

Interaction will LANL on η and I_{avg} scaling will continue. A strawman design of the superconducting vacuum tube liner concept will be developed.

The earlier estimates of the cryostat mass and wedged pole hybrid (WPH) wiggler weight are high. Better estimates can be made at the superconducting and WPH design points.

Benefit of Superconducting Wiggler and Strong Magnets

We have explored the benefits of stronger magnet technology on the performance of possible space-based FELs. The technologies are a super-ferric design which uses Holmium poles and racetrack superconducting windings, and the wedged pole hybrid. For the superconducting design the current density was varied to explore the benefits of increased current density, j. The results are shown in Figure 6. Stronger superconducting wigglers acheive higher extractions. The WPH design also showed increasing extraction with stronger magnets, Figure 3. At the present state-of-the-art for both technologies the superconducting design achieves 90% higher extraction. This increased extraction occurs because superconducting wiggler acheive $a_w = 1$ at lower λ_w at all gaps, Figure 12. The extraction benefit is a direct consequence of keeping the total wiggler length, L, fixed and operating both designs at the same <u>average</u> output power. The extraction benefits because γ is lower for the superconducting wiggler, there are more periods allowing the superconducting wiggler to achieve a higher extraction for the same peak circulating optical power. This permits it to operate at a lower duty factor, i.e. lower average beam current which enables the peak circulating power to increase further without changing the average circulating optical power. All analyses also kept the saturating gain fixed. Thus, the same optical cavity would be used in both designs (unless peak optical power influences the optic design).

A detailed discussion of the η and I_{avg} modeling as well as derivations of the approximate scaling laws follows.

Comparison of Superconducting with Wedged Pole Wigglers

There are several benefits from using a superconducting wiggler which help to offset the added system complexity. These benefits are a direct result of the ability of a superconducting wiggler to achieve more magnetic field than a WPH. This allows the superconducting device to operate at a smaller λ_w

while still achieving the optimum $a_w \simeq 1$. For a fixed length of wiggler, the superconducting device will have more periods and thus a higher extraction. In addition, since λ_w is smaller for a superconducting than a WPH, the beam energy is lower, leading to higher extraction since

$$\eta = \delta \int \frac{1}{\gamma} \frac{d\gamma}{dz}\, dz = \delta \int \frac{1}{\gamma^2}\, e_s\, a_w \sin \psi\, dz$$

We have used a simple model for η to explore the potential benefits of a superconducting device vs. WPH. The model neglects the effects of emittance and energy spread. (These should be very similar for both devices and cancel out to the lowest order.) The fixed parameters were

L = length of wiggler
λ_s = photon wavelength
g_{mag} = magnet gap (set by 3 mm vacuum tube offset plus beam clearance)
P_{out} = average output power
g = single pass gain at saturation
$Z_r \simeq 1/2L$

Since

$$\gamma^2 = \frac{\lambda_w}{2\lambda_s} \left(1 + a_w^2\left(\lambda_w, g_{mag}\right)\right)$$

We chose to vary λ_w and find the peak extraction vs. either remanent field, B_r or current density, j. (Varying γ with λ_w from resonance would be equivalent.)

The fixed system parameters are in Table 1.

Table 1

Wiggler Length (L)	20 m
Photon Wavelength (λ_s)	1 μm
Output Power (P_{out})	2.5 MW
Saturated Gain	0.4
Rayleigh Range (L/2)	10 m
Waist $(Z_R\ \lambda_s/\pi)^{\frac{1}{2}} = w_o$	0.178 m
Vacuum Tube Aperture (3x(2w))	1.5139 cm
Magnetic Gap (g + 0.3 cm)	1.8139 cm
Trapping Fraction, δ	0.3
Resonant Phase Angle, ψ_r	30°
Peak e-Beam Current	250 A

For each value of B_r, or j, an optimum λ_w was found. This is illustrated in Figures 1 and 2. Note that the optimum λ_w is lower for the superconducting wiggler, Figure 2 than the WPH, Figure 1. This implies that a lower beam energy can be used provided there is sufficient extraction to produce the required power. Note also, that the superconducting wiggler has a peak extraction of 0.223 while the WPH has a peak extraction of 0.125, (at the chosen B_r and j values).

Figure 3 shows the benefit of stronger magnets for WPH. The upper curve is the extraction that could be reached without any limit on the average beam current. The extraction improves from 0.09 at B_r = 0.6T to 0.135 at B_r = 1.2T or a 50% improvement by doubling B_r. If a current cap is operative, then the beam energy needs to increase at low B_r since there is insufficient current to acheive the necessary output power. The upper curve in Figure 4 shows the average beam current needed to achieve the desired output power. If the accelerator current is not high enough, say 0.2 A when 0.25 A are needed, the γ must be increased to make up for the loss. This is illustrated in Figure 5. Since γ must be increased, λ_w and a_w (λ_w) change to maintain resonance, but this results in a loss of extraction (Figure 1) and a further increase in γ is needed to make up for the additional lost extraction. The net result is a B_r dependant η degradation which is shown as the lower curve of Figure 3. As B_r increases the extraction rises so less current is needed until the current limit makes no effect on the achievable extraction.

As already noted, the superconducting wiggler achieves higher extraction because it can operate at a lower wavelength which implies a lower γ. When λ_w is varied at fixed current, j the optimum extraction, η is higher, Figure 2. For a wide range of j the superconducting wiggler is able to achieve a higher extraction. This is illustrated in Figure 6. The upper curve shows the maximum possible extraction achievable without any caps on the maximum current density. An added benefit of the superconducting wiggler is that the average beam current needed to achieve the target power, P_{out}, is lower. This is shown in Figure 7. As shown in the appendix, the average current scales as γ^2/a_w^2. This means that the superconducting can achieve the required output power with 30% less average current. The current limit of 0.2 A which decreased the WPH extraction at lower B_r, see Figure 3 is not even needed for the superconducting wiggler. The maximum achievable extraction from a superconducting wiggler is determined by the highest current density for that λ_w. At larger j, than this the superconducting wiggler must operate at a reduced wavelength, see Figure 8. When λ_w drops, the a_w falls below 1 and the η plummets as shown by the lower curve of Figure 6. This rapid fall-off in η also forces the average beam current to rise very steeply as seen by the upper curve of Figure 7. Therefore, the maximum achievable j for superconducting wigglers has $j = j_{max} (\lambda_w)$ such that $a_w = 1$ and $\eta = \eta_{max}$. If a_w falls very much below unity, the superconducting wiggler FEL performance degrades rapidly.

Both wiggler designs optimize at $a_w \simeq 1$. This is shown in Figure 9a for WPH and 10a for superconducting. (For completeness $\lambda_w (B_r)$, $\lambda_w(j)$, $\gamma(j)$, and $j/j_{max}(j)$ are shown in Figures 9b, 10b, 10c, and 10d.) At low j, in order to get $a_w = 1$, the wavelength λ_w increases and j falls below j_{max} so that at lower j we do not even need the fall current density that a superconducting wiggler is capable of achieving.

Gap Dependance of Superconducting Benefit

We have established that $a_w = 1$ and a minimum λ_w yield the highest extraction at fixed L, P_{out}. At any gap, increasing λ_w leads to an increase of a_w. The optimum λ_w has $a_w = 1$. This is illustrated at gap = 1.81 cm in Figure 11. The $a_w = 1$ points are:

λ_w (super) = 2.48 cm $\qquad$ γ (super) = 157.48

λ_w (WPH) = 3.82 cm $\qquad$ γ (WPH) = 195.44

As the gap is reduced (more beam scraping on the wiggler) the extraction (neglecting aperturing) increases due to a shorter wavelength, λ_w, Figure 12, but the extraction benefit for the superconducting remains flat until the magnetic gap falls below 0.8 cm, Figure 13. From Figure 12, short period ($\lambda_w \lesssim 2$ cm) wigglers are useful at gaps $\lesssim$ 0.65 cm for WPH and gaps $\lesssim$ 1.25 cm for superconducting. Of course, short period wigglers could be used at larger gaps with $a_w < 1$ with a resultant loss of extraction. We have not explored sub-optimum designs in great detail.

Summary

Scaling laws of average current and extraction at fixed average laser power and wiggler length have been determined. Superconducting wigglers benefit from increased current densities, j (see Figure 6) with the highest extraction achieved for $j = j_{max}$. Wedged pole hybrid wigglers also benefit from higher remanent field in the magnets (see Figure 3). At a design point which reflects the current state-of-the-are for both technologies

$B_r = 1.0T$ $\qquad$ WPH

$j = j_{max}$ $\qquad$ Superconducting

$$\frac{\eta(\text{super})}{\eta(\text{WPH})} = 1.9$$

$$\frac{I_{avg}(\text{super})}{I_{avg}(\text{WPH})} = 0.65$$

$$\frac{\gamma(\text{super})}{\gamma(\text{WPH})} = 0.81$$

The design point parameters are shown in shown in Tables 1 and 2.

Table 2

Superconducting		WPH	
j	71.7 kA/cm^2	B_r	1.0T
λ_w	2.55 cm	λ_w	3.80 cm
γ	167	γ	192
I_{avg}	0.124 A	I_{avg}	0.206 A
a_w	1.09	a_w	0.976
η	0.236	η	0.123

APPENDIX

APPENDIX

Duty Factor Calculation Used for Average Beam Current

At saturation, assume a fixed average cw output power, P_{out} and a fixed out coupling (optical gain/pass), g. Then

$$P_{out} = g \bar{P}_s \tag{1}$$

where $\bar{P}_s$ is the average power in the optical beam

$$\bar{P}_s = \text{duty} \times P_s \tag{2}$$

$$\text{duty} \equiv I_{avg}/I_{peak} \tag{3}$$

From energy conservation

$$gP_s = \eta P_{eb} \tag{4}$$

$$P_{eb} = \gamma mc^2 I_{peak} \tag{5}$$

P_s = optical power at saturation from a micropulse

At low gain

$$\eta = \delta \int_0^L \frac{1}{\gamma} \frac{d\gamma}{dz} = \delta \int_0^L \frac{1}{\gamma^2} e_s a_w \sin\phi \, dz \tag{6a}$$

If the gain per pass is low enough, then

$$\eta = f e_{s,peak} = f \sqrt{P_s} \tag{6}$$

The effects of gap, Gaussian beam shape, taper, etc are all buried in f. The $\sqrt{L_s}$ scaling comes from e_s linearity in (6a). When (6), (4) are substituted into (1) we get

$$P_{out} = f\, P_{eb} \frac{\overline{P}_s}{\sqrt{P_s}} \tag{7}$$

using (2) for P_s in (7) gives

$$P_{out} = f\, P_{eb} \sqrt{duty}\ \sqrt{\overline{P}_s} \tag{8}$$

Finally, after using (1) for P_s in (8) we get

$$duty = \frac{g\, P_{out}}{(f\, P_{eb})^2} \tag{9}$$

Extraction Model

The extraction model uses a Gaussian optical beam for e_s (z) in (6a) and neglects the variation of a_w, γ, $\sin\phi$, with z. The extraction of the resonant electrons is found. Both wedged pole and superconducting systems use the same assumptions so there should be a pretty good cancellation of errors if relative performance is used. The absolute numbers will be inaccurate. Anyway, when $\gamma \simeq \gamma_r$, $\sin\phi \simeq \sin\phi_r$, ϕ_r = const, a_w = const, the integral in (6a) is analytic and η is

$$\eta = 8\pi \left[\frac{e}{mc^2}\right] \delta \sin\phi \left[\frac{2P_s}{c}\right]^{1/2} \chi \tag{10a}$$

$$\chi = \frac{1}{\alpha}\ \frac{gap}{2\lambda_w}\ \frac{a_w}{\left[1+ a_w^2\right]}\ \frac{\ln\left[q+(1+q^2)^{\frac{1}{2}}\right]}{(1+q^2)^{\frac{1}{2}}} \tag{10b}$$

α = gap/2w
w = optical waist at wiggler entrance (exit)
gap = vacuum tube aperture
$q = L/2Z_R$
L = wiggler length
Z_R = Rayleigh range

From Equation (10) we see that the function f of (6) is

$$f = 8\pi \left(\frac{e}{mc^2}\right) \delta \sin \phi \left(\frac{2}{c}\right)^{\frac{1}{2}} \frac{1}{\alpha} \frac{gap}{2} \frac{\ln\left[q+(1+q^2)^{\frac{1}{2}}\right]}{(1+q^2)^{\frac{1}{2}}} \text{ x }$$

$$\frac{a_w}{\lambda_w\ (1+a_w^2)}$$

$$f = h\ (\delta,\phi,\alpha,gap,\ L/2Z_r)\ \frac{a_w}{\lambda_w(1+a_w^2)} \qquad (11)$$

The optimum Rayleigh range is at $L/2Z_R \simeq 1$ or $Z_R = L/2$. A minimum gap gives the largest B field. Once the length is fixed we know Z_R and at fixed optical wavelength, λ_s we know the waist which gives the minimum clear gap

$$gap = 2\ w\alpha = 2\alpha_o w\ \ (1+q^2)^{\frac{1}{2}} \qquad (12)$$

$$w_o = \sqrt{\frac{\lambda_s Z_R}{\pi}} \qquad (13)$$

The magnetic gap is an additional 3 mm larger for a vacuum tube

$$g_{mag} = gap + 0.3\ cm \qquad (14)$$

The maximum extraction is found by varying λ_w. The a_w is a function of λ_w, B_r, g_{mag} for the wedged poles and a function of λ_w, j, g_{mag} for superconducting wiggler. The extraction is a function of λ_w and (B_r or j) since g_{mag} is fixed. At each B_r or j we vary λ_w to find the highest extraction. The optimum λ_w, $a_w(\lambda_w)$ are used in the resonance equation to get γ and (9) is used to find the duty factor. The result is

$$\eta\begin{pmatrix} j \\ B_r \end{pmatrix},\ \lambda_w\begin{pmatrix} j \\ B_r \end{pmatrix},\ a_w\begin{pmatrix} j \\ B_r \end{pmatrix},\ \gamma\begin{pmatrix} j \\ B_r \end{pmatrix},\ I_{avg}\begin{pmatrix} j \\ B_r \end{pmatrix}$$

In general, superconducting wigglers can achieve $a_w = 1$ at a smaller λ_w than wedged poles. From (6a) or (11), when λ_w is small γ is small, and the extraction increases. In addition, this yields a lower duty factor, i.e. a small average current. This can be seen from (11) and the resonance equation:

$$\gamma^2 = \frac{\lambda_w}{2\lambda_s}\left(1+a_w^2\right) \tag{15}$$

$$f = \frac{h\ a_w}{2\lambda_s\gamma^2} \tag{16}$$

$$\text{duty} = \left\{\frac{P_{out}\ g\ (2\lambda_s)^2}{h^2\left(mc^2 I_{peak}\right)^2}\right\}\frac{\gamma^2}{a_w^2} \tag{17}$$

$$\text{duty} = \frac{k\gamma^2}{a_w^2} \tag{18}$$

Both types of wiggler operate best at $a_w \simeq 1$, but the superconducting wigglers has a lower γ then the WPH

$\gamma_{super} = 157$
$\gamma_{WPH} = 195$

giving

duty (superconducting) = 0.65 duty (wedged).

Extraction Scaling at Fixed P_{out}, L

The constraint of a fixed output power and length leads to a $1/\gamma^3$ scaling of the extraction, η. This can be shown by using (6), (2) and (9)

$$\eta = f\sqrt{\bar{P}_s} = f\sqrt{\frac{\bar{P}_s}{duty}} = f^2 P_{eb}\sqrt{\frac{\bar{P}_s}{P_{out} \times g}} \qquad (19)$$

The factor under the square root is just $1/g^2$. Using (16) and (5) gives

$$\eta = f^2 \frac{P_{eb}}{g} \qquad (20)$$

$$\eta = k \frac{a_w^2}{\gamma^3} \qquad (21)$$

The constant k contains functions of the fixed parameters of the system.

Optimum performance has $a_w = 1$. This lends to

$$\frac{\eta_{super}}{\eta_{WPH}} = \left(\frac{\gamma_{WPH}}{\gamma_{super}}\right)^3 = 1.9$$

Reducduction of Image Currents in Vacuum Tube Wall

A major limitation on the feasibility of a space-based superferric wiggler is resistive wall heating due to image currents induced by the electron micropulses. While a lower average beam current does reduce this heating, the amount is negligible when one considers that to supply 3 kW of refrigeration in the 1.8 -9°K range requires about 10^5 kg = 100 metric tons of refrigerator which has a volume of about 200 m^3 at a cost of $20-30M. The efficiency is about 10% of carnot or 0.13% so 3 kW of cooling requires 2.2 MW of prime power.

These problems cannot be reduced by simply cooling the vacuum tube since the anomalous skin effect increases the rf surface resistance thereby limiting the heat reduction to about a factor of 10.

A much more elegant approach is to use a thin superconducting liner on the inner wall of the vacuum tube. Type I superconductors are driven normal by the wiggler field but type II are not. The type II conductors, such as NbTi, still exhibit zero resistance to DC currents, but they have very weak diamagnitism beyond H_{c1} with a perfect Meissner effect below H_{c1}. Niobium titanium has H_{c1} = 30 G, so there is essentially no perturbation in the wiggler field except near the zero crossings. (The width of the zero crossing area from -30 G to 30 G corresponds to the 1000th harmonic or so.) The type II superconductors have much higher normal current resistivities since high critical fields require flux pinning centers to reduce fluxoid motion. These pinning centers are very effective scatterers of normal electrons. The higher normal current resistivities mean that type II superconductors has a much higher rf surface resistance than type I (which is why type I superconductors are used for superconducting rf cavities).

A very rough estimate was made of the reduction in the power deposition. The skin depth of NbTi is 4×10^{-3} cm at 100 MHz and the DC penetration depth is about 10^{-5} to 10^{-4} cm. (Type II have a longer penetration depth than type I.) The reduction of the power deposition using the Poynting vector is 10^{-5} over what would be absorbed without NbTi going superconducting. Since the rf power deposition scales as $1/\sigma$, the overall reduction is 5.8×10^{-5} relative to copper at 300°K. Takeda has estimated that the resistive wall heating should be ~300 W/m, so with a NbTi liner

$$dP/dz \simeq 0.02 \text{ W/m} \qquad \sigma_{cu} = 5 \times 10^{7}$$

$$\sigma_{NbTi} = 1.5 \times 10^{6}$$

If dP/dz due to resistive wall heating is this low, then it becomes negligible relative other heat sources.

The key element in reducing resistive wall heating is the use of a superconducting liner. The wiggler field must be established <u>before</u> the liner is superconducting since at zero resistance, $dB/dt = 0$ for the <u>static</u> wiggler field and the liner would act as a perfect shield against intrusion of the wiggler if it is superconducting before the wiggler field has been established. Thus we must use a "warm" ($T > T_c = 9.3$°K) bore while the magnet is being energized, then cool the bore below T_c after establishing the wiggler field. Steering correction would use thin superconducting filaments along the same lines as the sextupole superconducting correctors being used in the 17.5 m SSC dipoles.

FIGURES 1 - 13

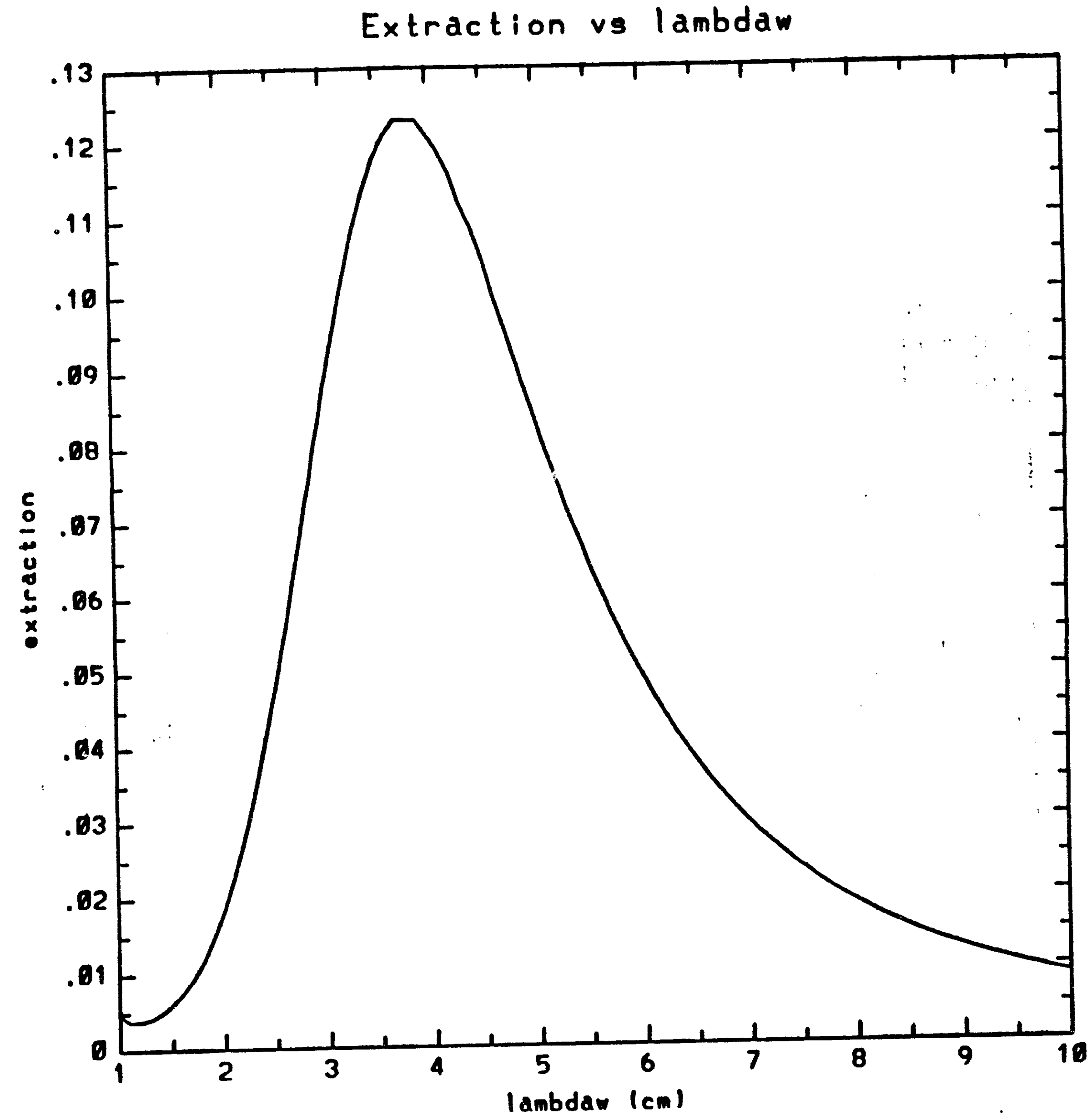

Extraction vs λ_w @ B_r = 1.0T
for WPH

B_r = 1.0T

Fig 2

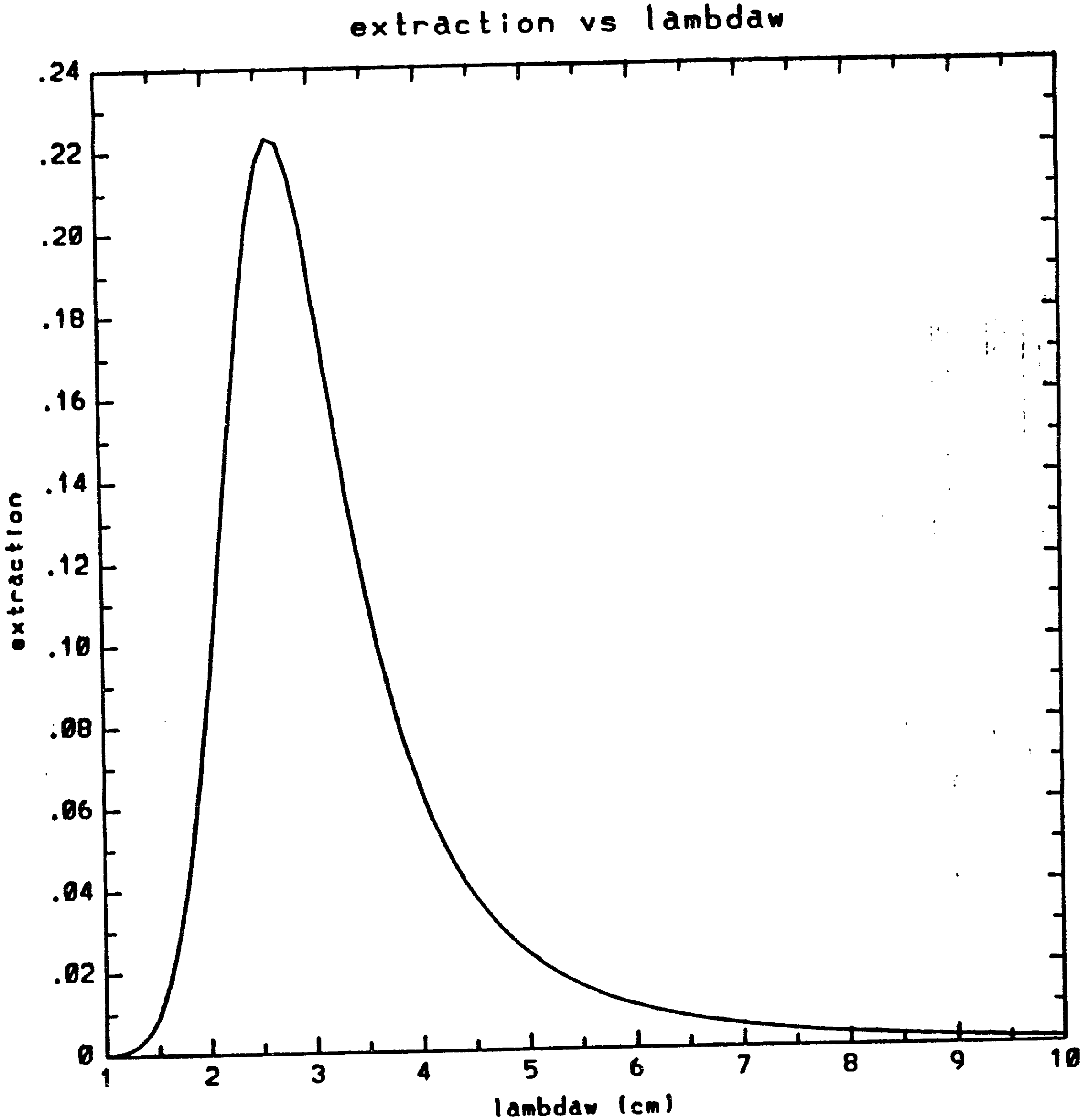

Extraction vs λ_w @ $\bar{j} = 60$ kamps/cm^2
supercon wiggler

Fig 2

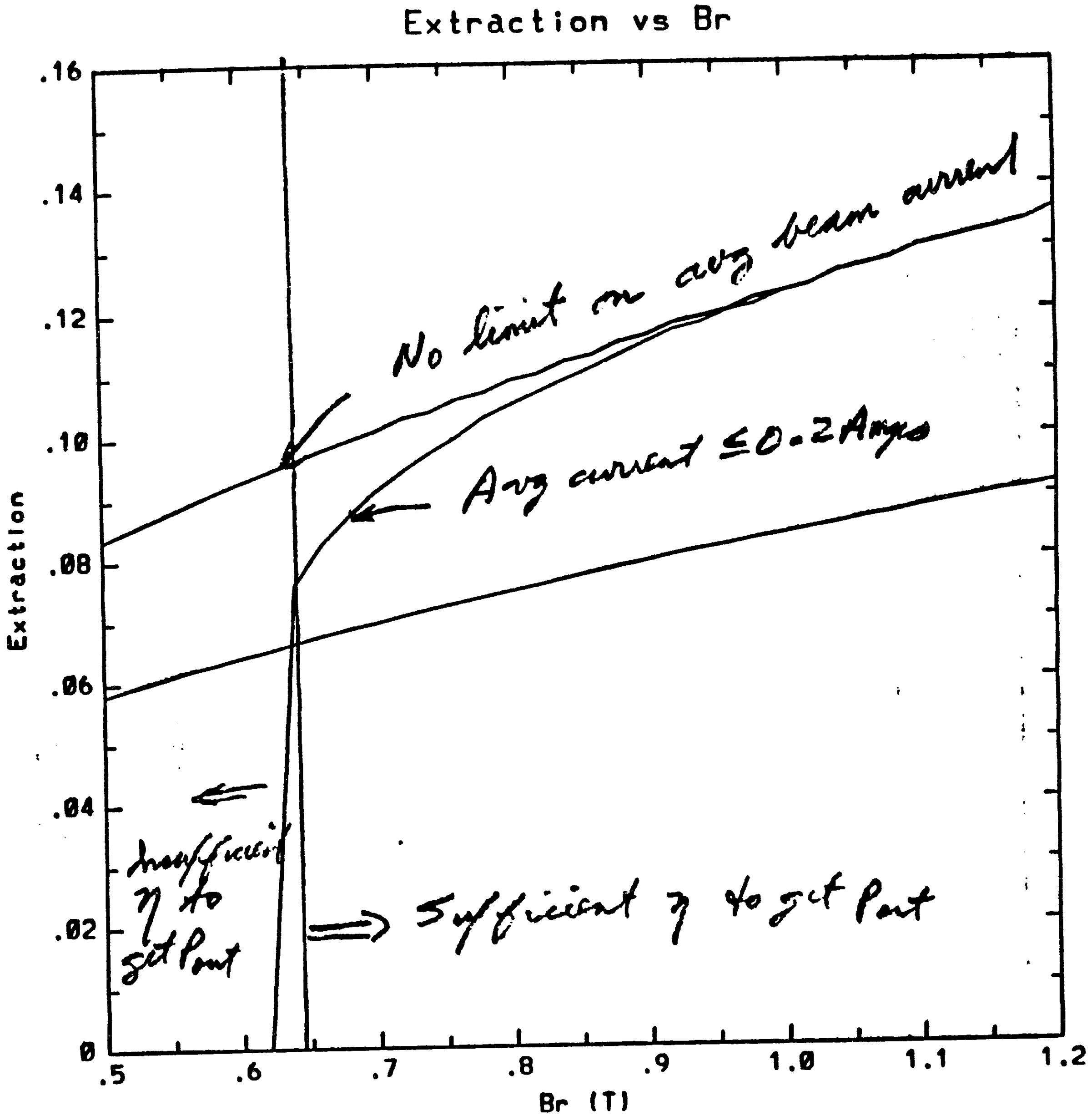

Benefit of stronger magnets

Fig 3

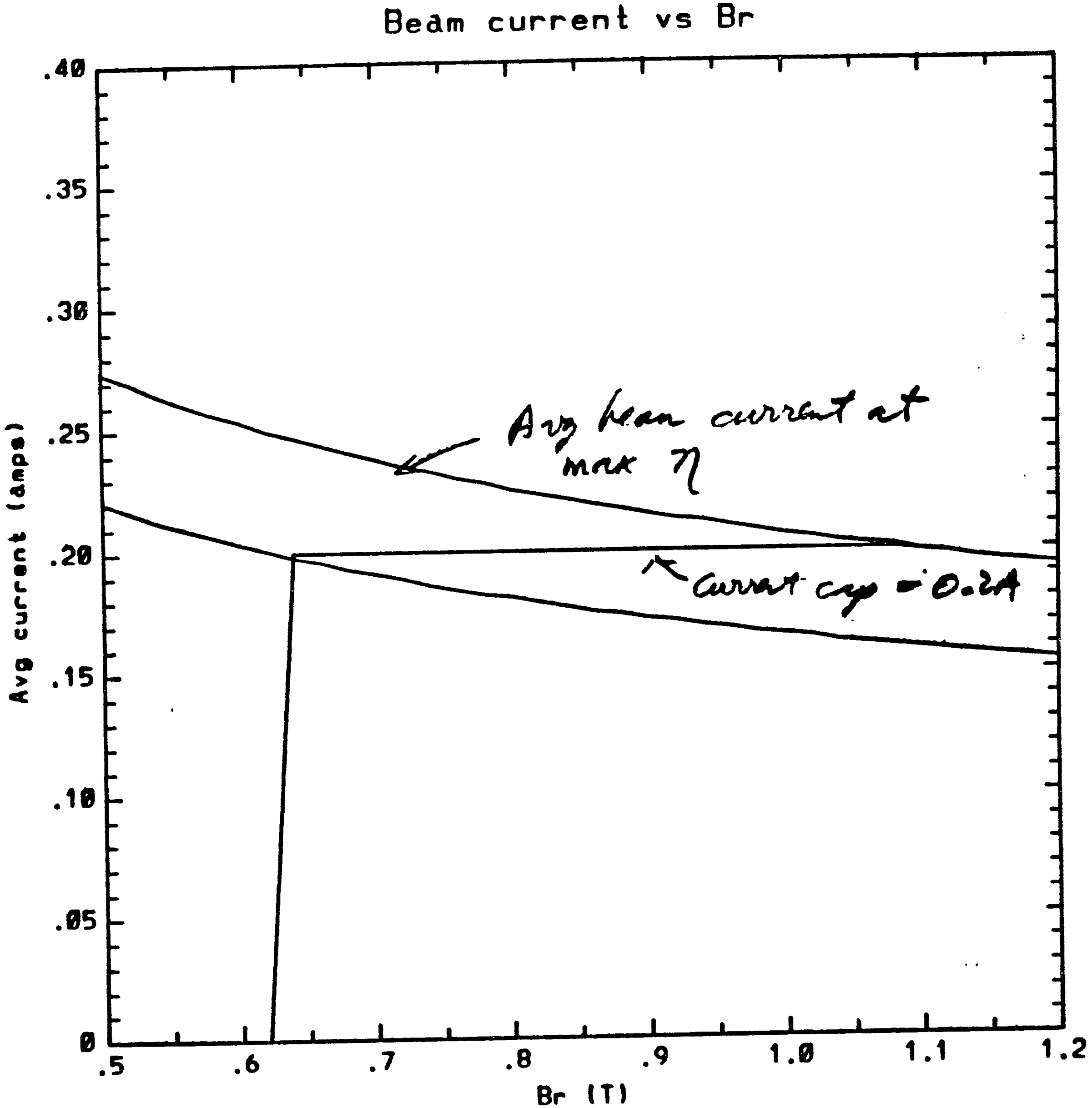

Avg beam current at max η

current cap = 0.2A

Avg current reduction for stronger magnets

Fig 4

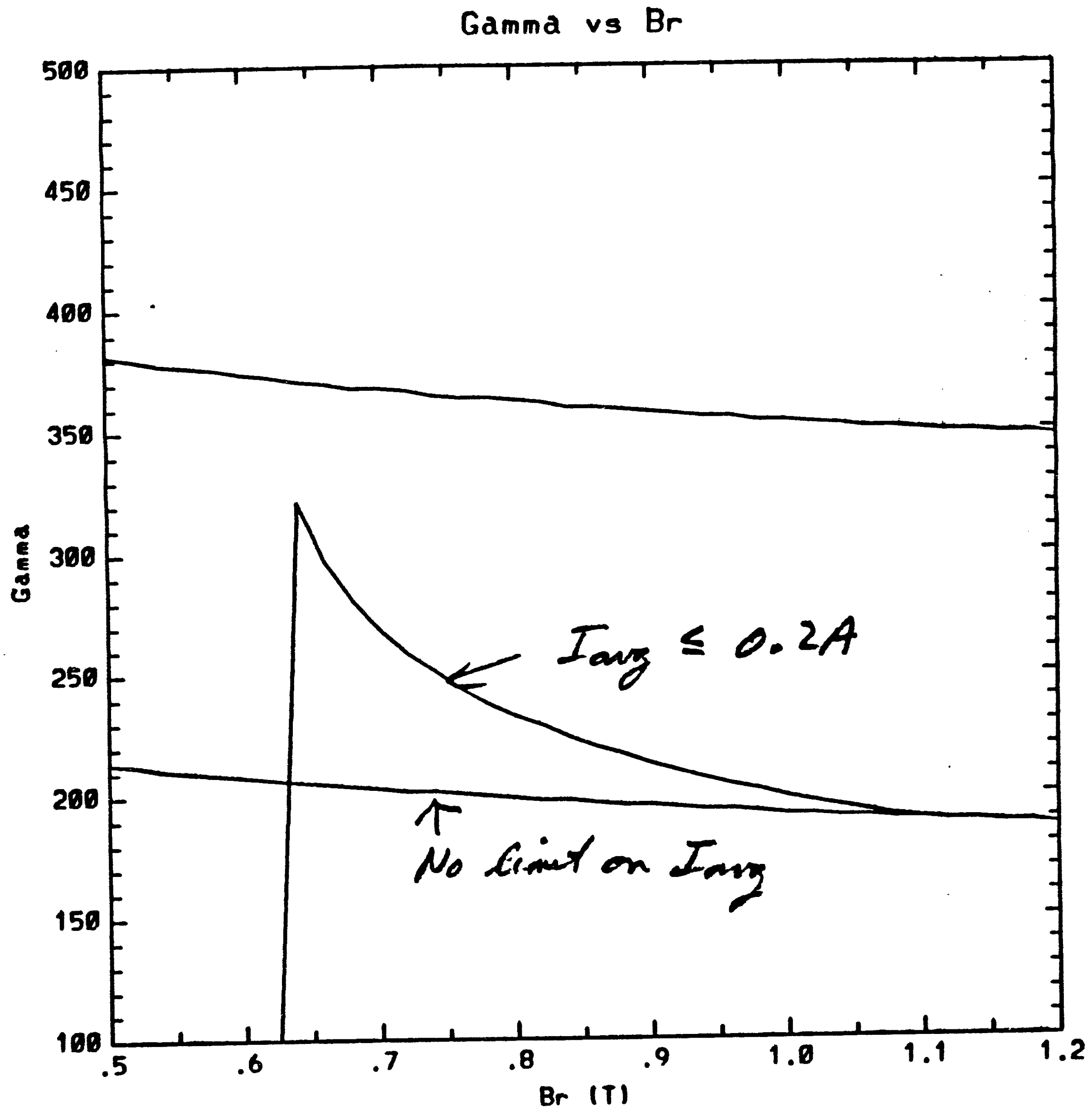

Fig 5 - E-beam energy

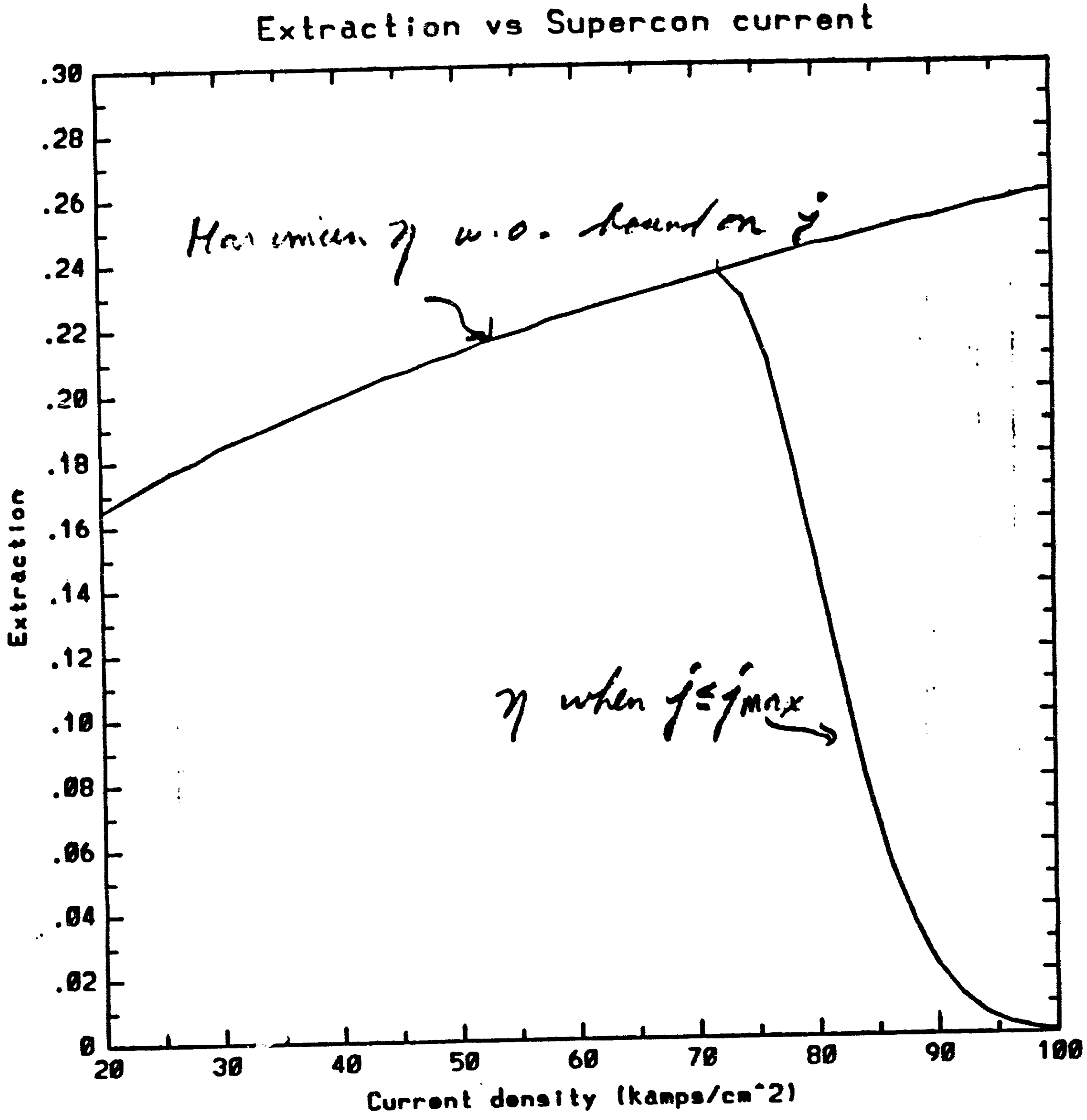

Fig 6 - Supercon extraction vs current density

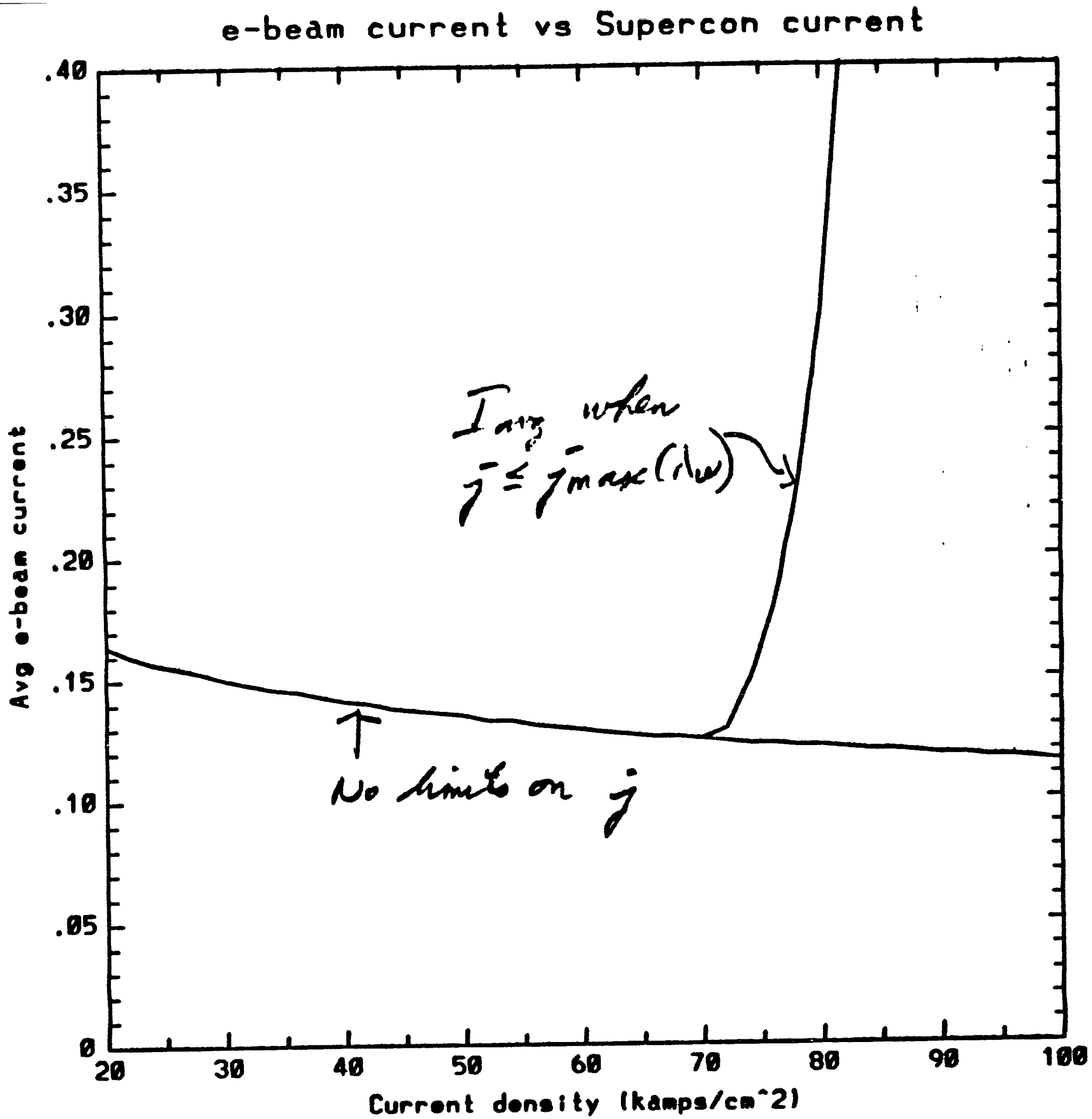

Fig 7 - Avg e-beam current needed for supercon wigglers

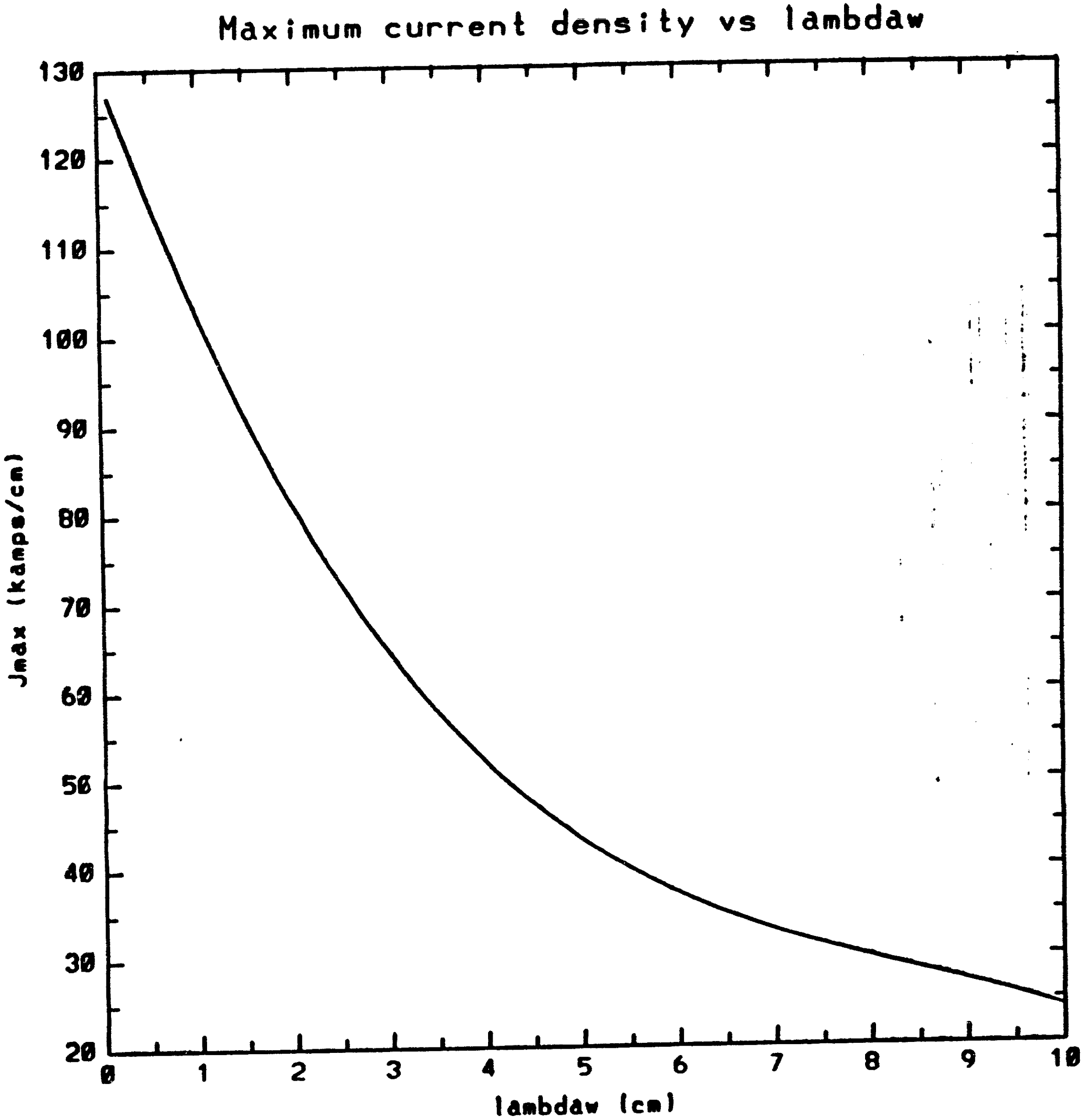

Fig 8 - Maximum allowed [illegible] current density vs λw

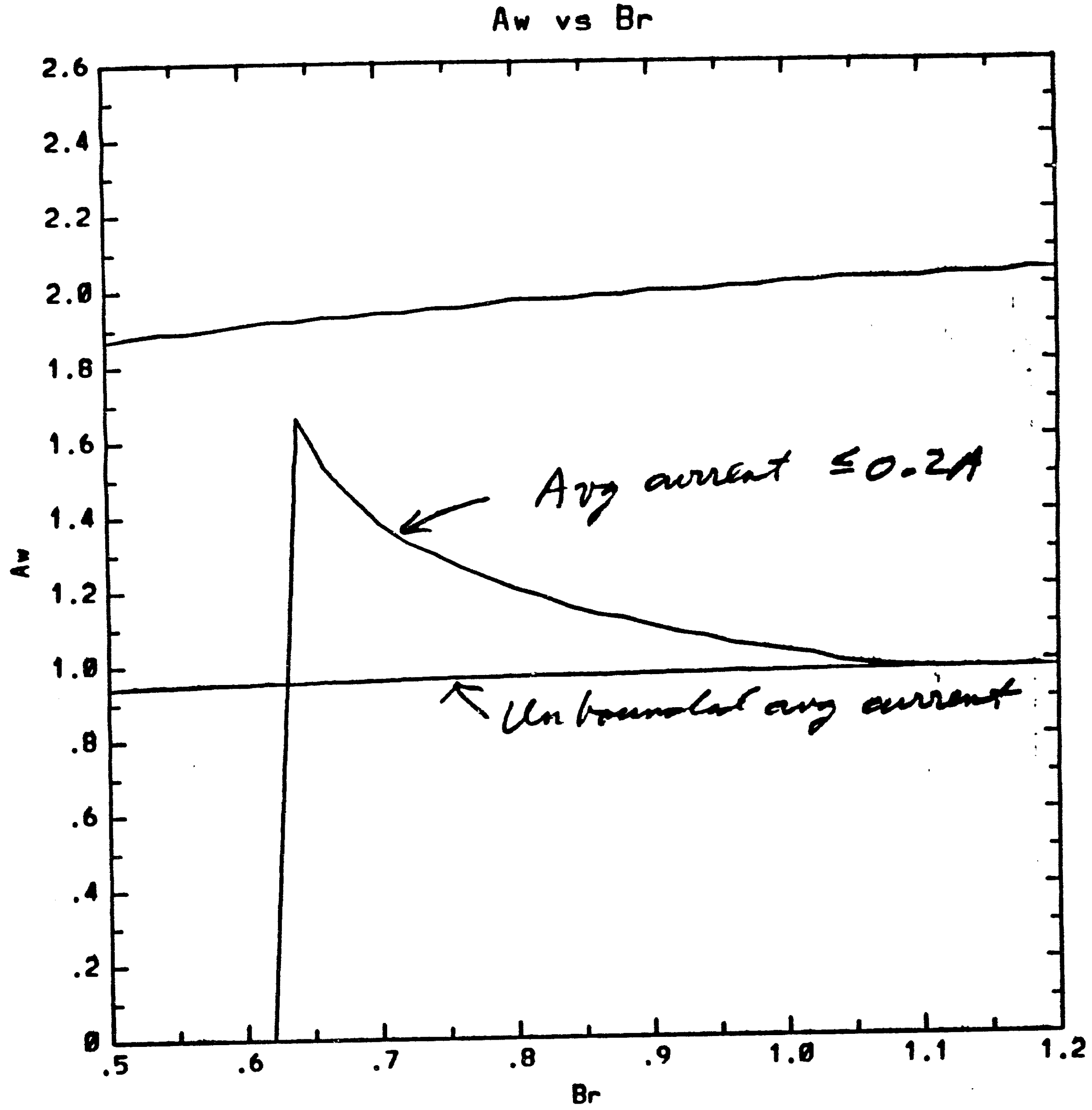

Avg current ≤0.2A

Unbounded avg current

Fig 9a: A_w of WPH vs B_r. $a_w \approx 1$ for all B_r

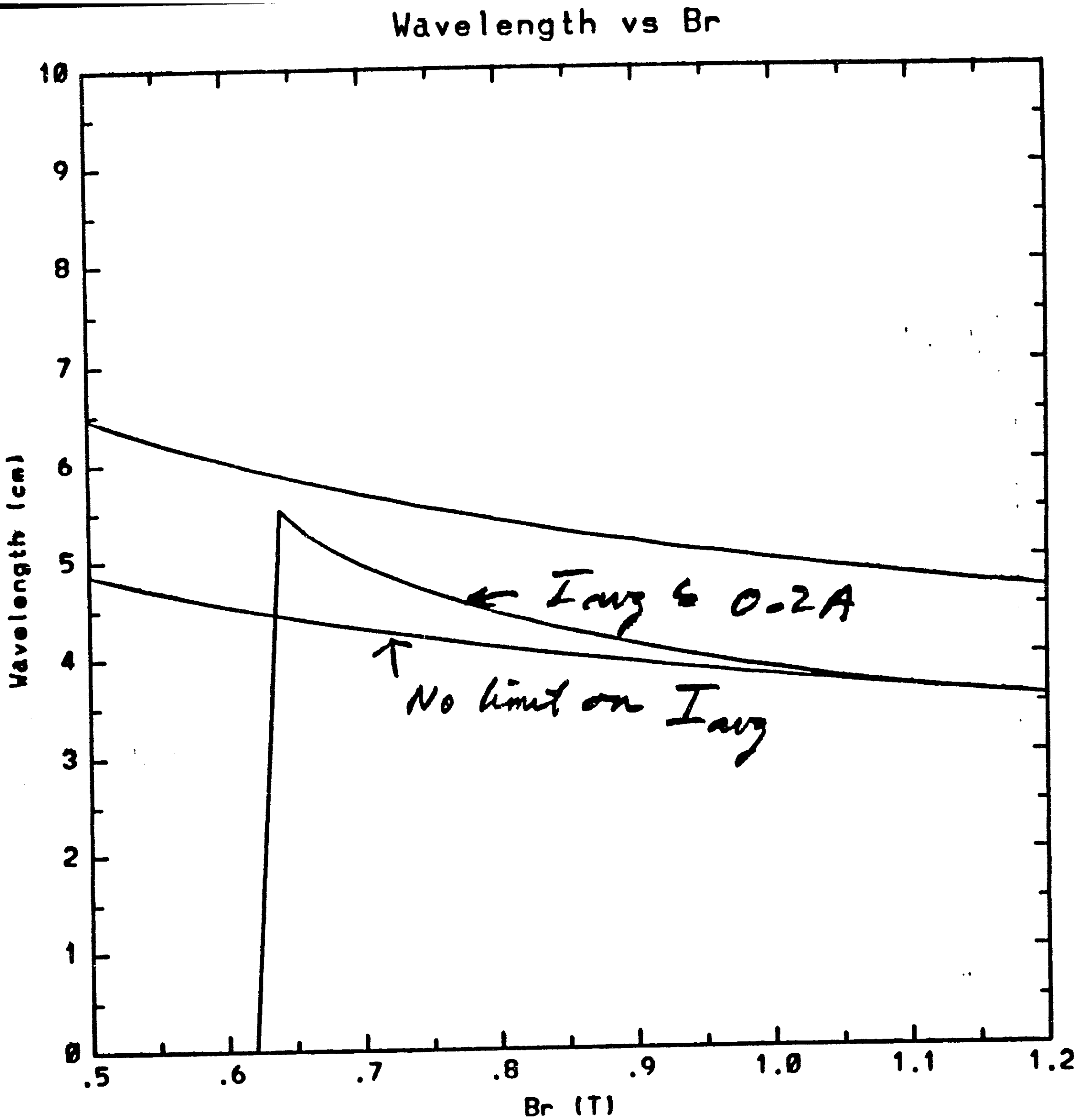
Wavelength vs Br
Wavelength (cm)
0
1
2
3
4
5
6
7
8
9
10
.5
.6
.7
.8
.9
1.0
1.1
1.2
Br (T)
← Iavg ≤ 0.2A
↑ No limit on Iavg

Fig 9b

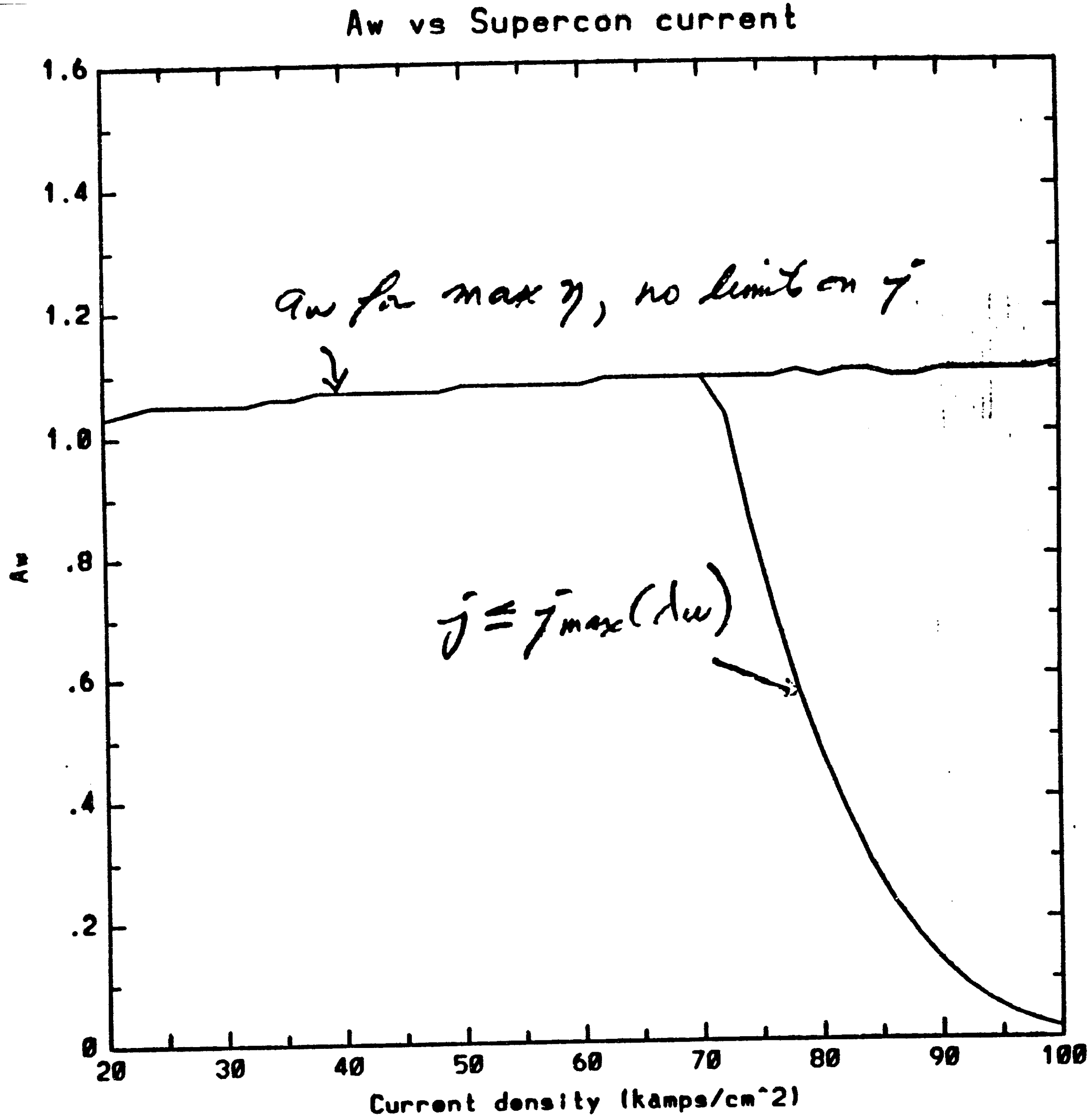

Fig 10a – Aw for supercon vs j

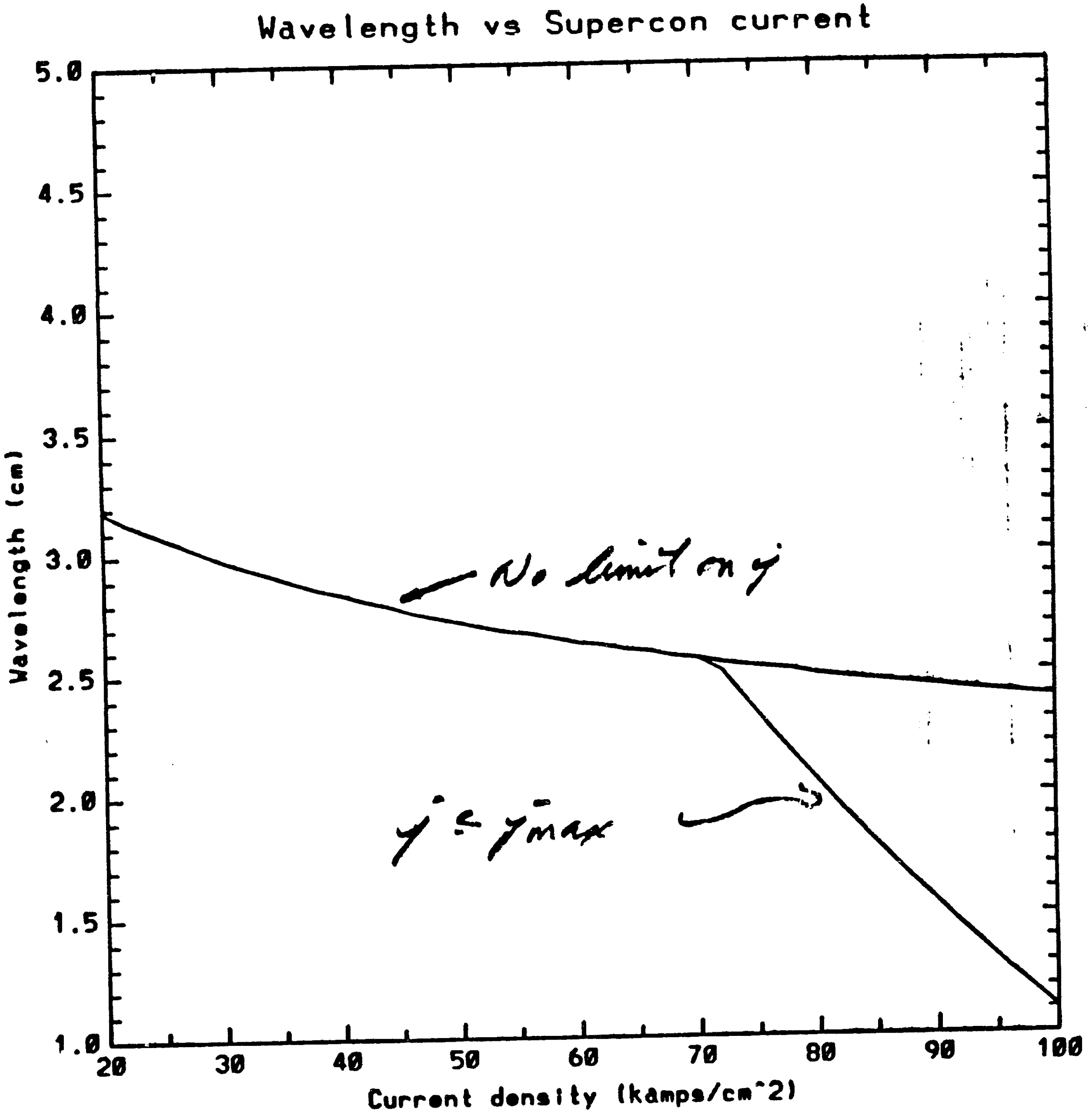

Fig 106 – λw vs j

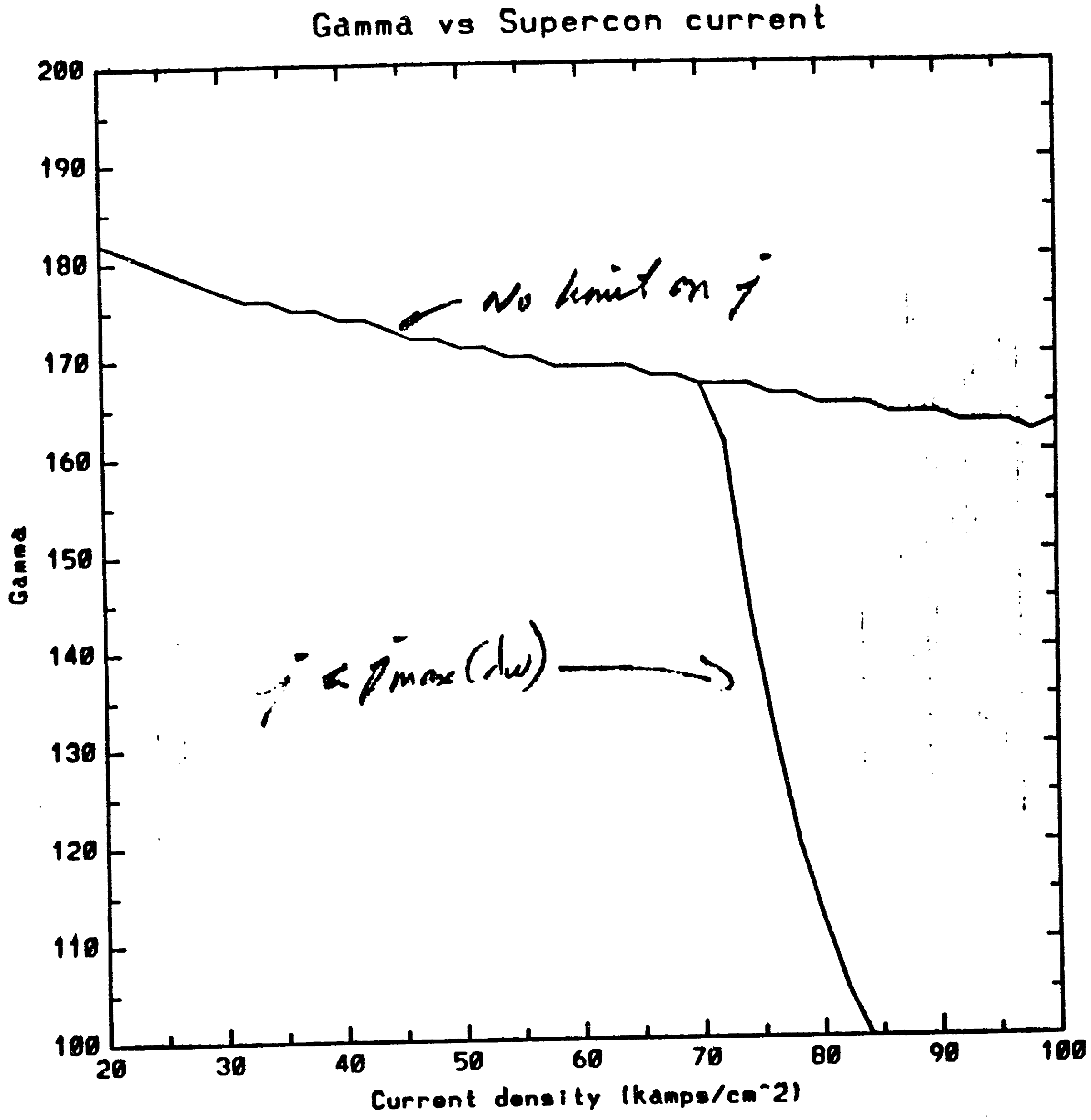
Gamma vs Supercon current

Fig 10c – γ vs j

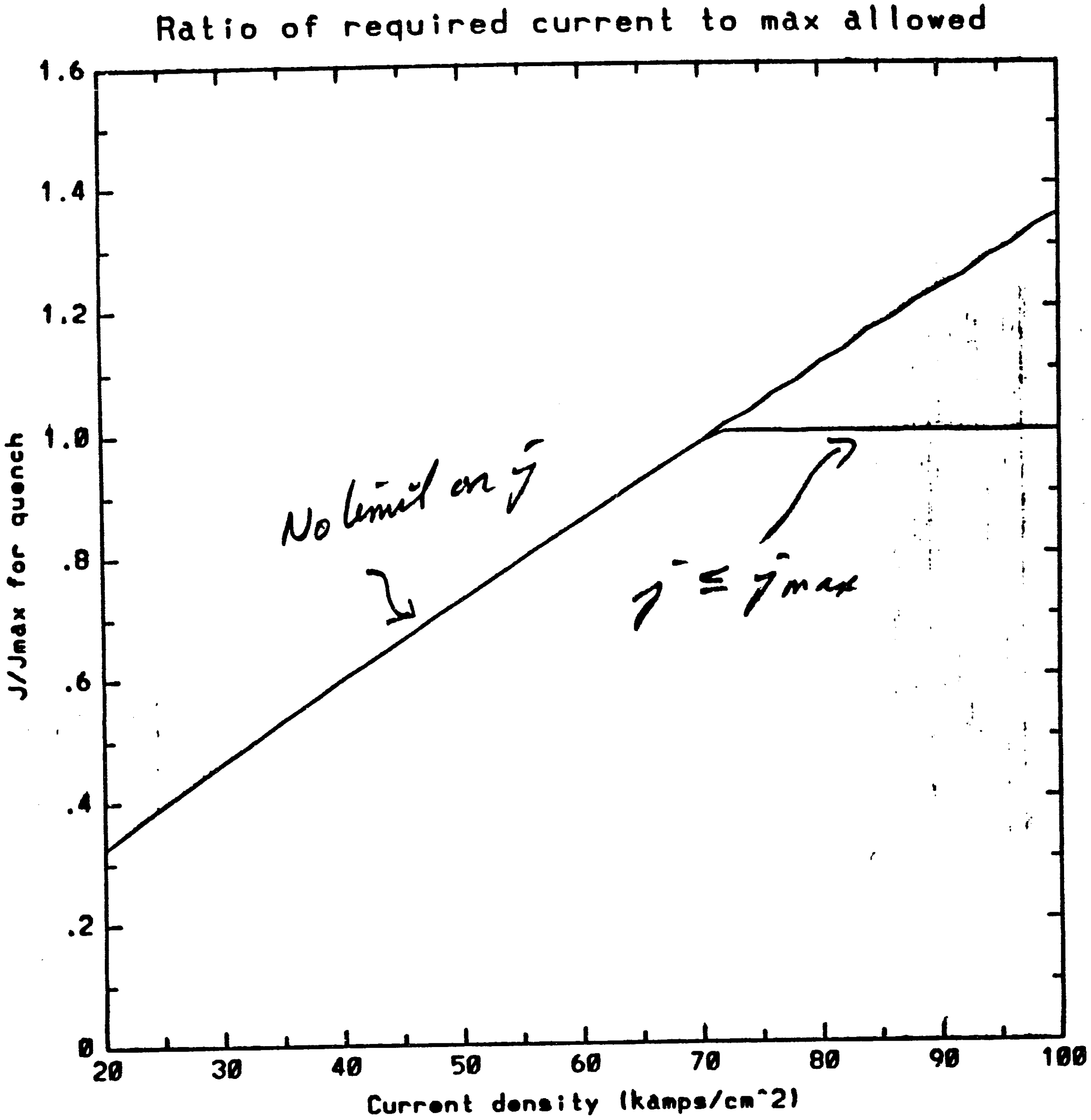
Ratio of required current to max allowed

Fig 10d – $\bar{j}/\bar{j}_{max}$ vs $\bar{j}$

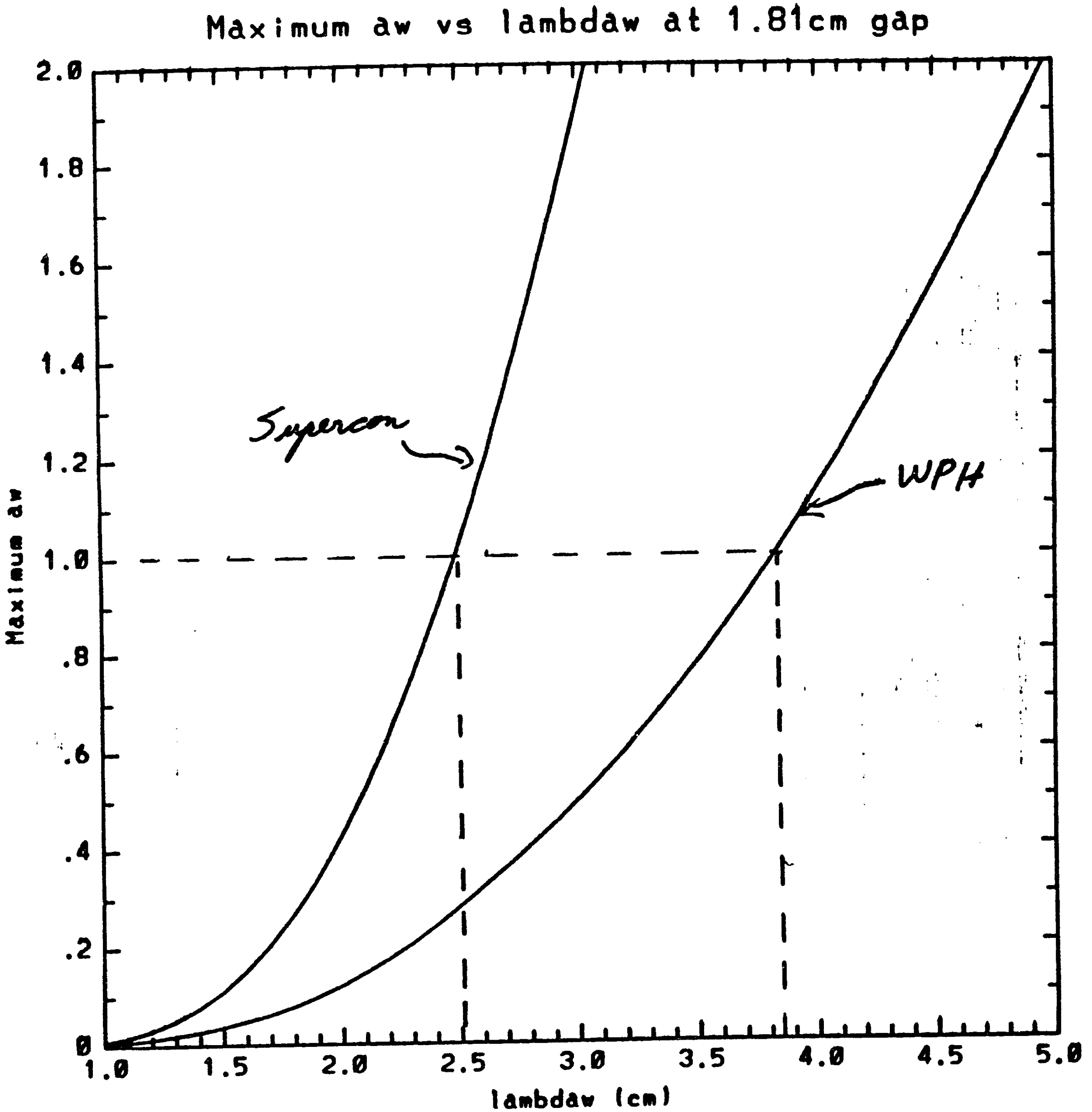

$B_R = 1.0T$

$j = j_{max}$

Fig 11 – $a_w(\lambda_w)$ at 1.81 cm gap for supercon + WPH

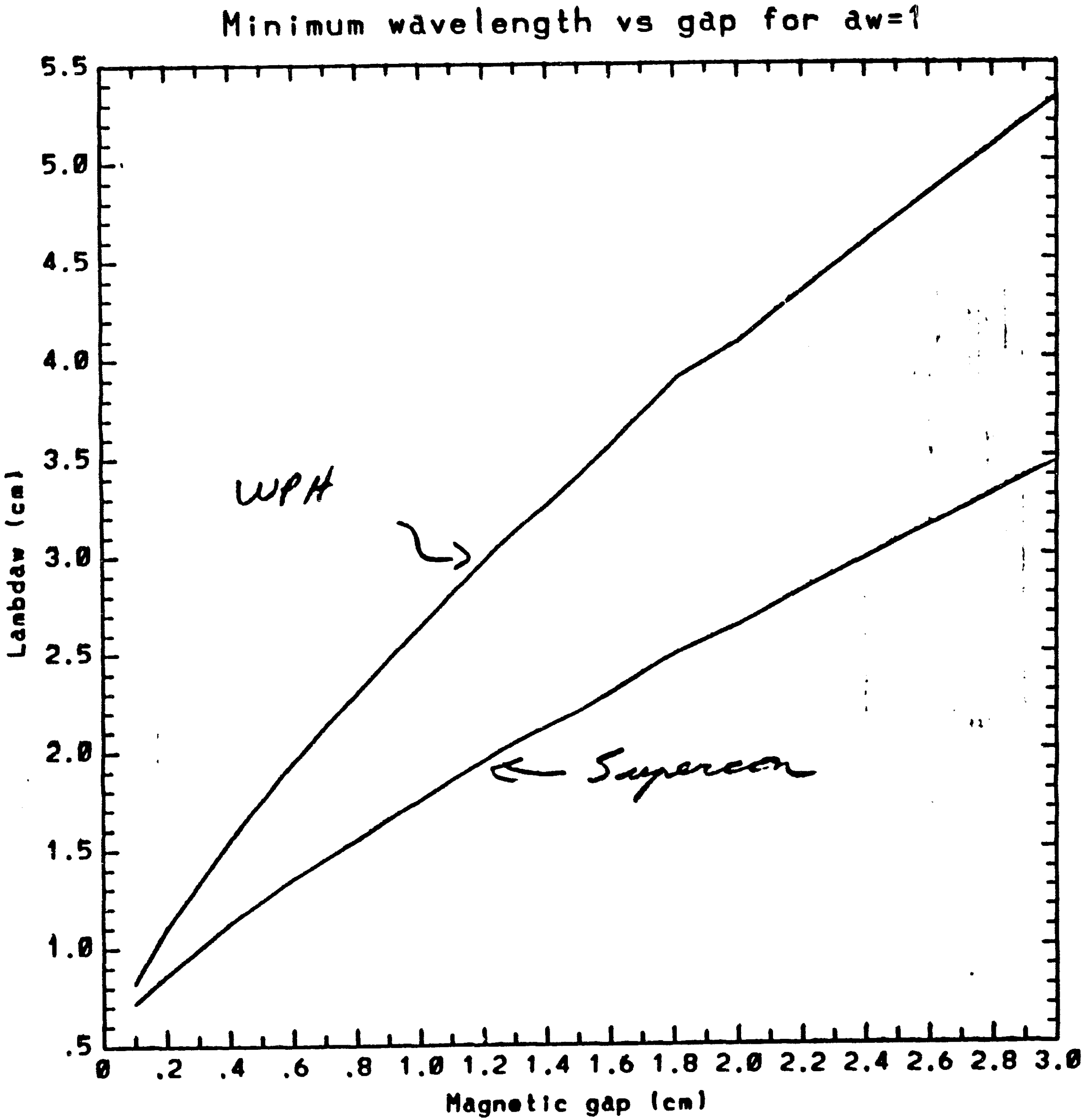

$B_r = 1.0T$
$j = j_{max}$

Fig 12 – Minimum λ_w vs magnetic gap for supercon & WPH

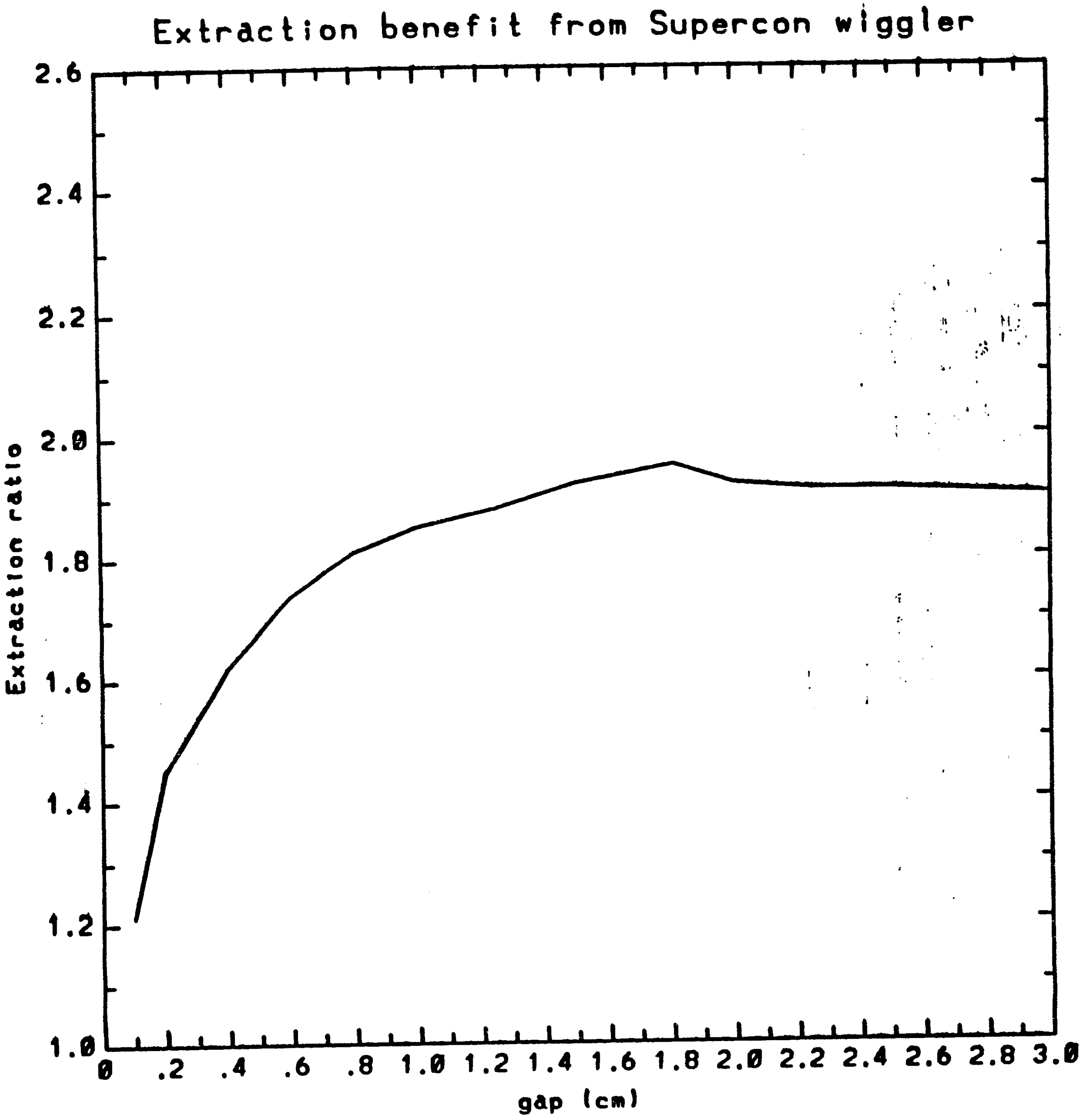

$B_r = 1.0T$

$j = j_{max}$

Fig 13 - η(supercon) / η(WPH) vs magnetic gap at $a_w = 1$.

MONTHLY PROGRESS REPORT

June 1990

Contract: 9-XG9-E9513-1
STI Control No.: 1737

EVALUATION OF SUPERCONDUCTING WIGGLER DESIGNS AND FREE-ELECTRON LASER SUPPORT

Monthly Progress Report
for Period Ending June 15, 1990

COOLING SYSTEM

A passive (dewar) and active (refrigerator) approach to maintaining superconducting temperatures of ca. 4.2°K were examined.

Heat load at 4.2°K arises from synchrotron radiation, e-beam halo and heat leakage. Heat leakage has been estimated to be 0.005 W/m based on existing space cryostat designs. The other loads are unknown, so the total heat load is a parameter.

The passive approach is summarized in an appendix. It's main features are the use of superfluid He II and a non-mechanical, fountain effect pump. Pumping is needed in zero gravity because helium is diagmagnetic so it would be repelled by the wiggler poles with fluid accumulating at the magnets. In addition, there are thermal issues of two phase management. The appendix describes the results of the cryostat design. While operation at 2.1°K aids magnet stability, the cryogen mass needed for 1 year of operation at 0.2 W/m is 500 kg/m.

The active approach would use refrigeration. At present there are no space-qualified cryogenic refrigerators. Lockheed is presently working on an 80°K refrigerator for space use. The main issue is lifetime. We have made a worst case analysis of power and mass requirements using land based refrigeration data. Since most of the mass, volume and power are due to the 4.2°K heat load we can ignore the high temperature refrigeration. (If SSC heat loads are used, 90% of the mass, volume and power are from the 4.2°K heat load.) At 4.2°K the refrigerator mass and volume scaling are:

C = total cooling (W)

$$\text{Mass (kg)} = 306\ C^{0.706}$$

$$\text{Volume } (M^3) = 0.406\ C^{0.848}$$

$$\text{Power (W)} = 25 \times \left(\frac{300}{4.2}\right) C$$

The power scaling assumes a power efficiency of 4% of ideal Carnot efficiency. At L=20 m, C=0.2 W/m the mass, volume and power are:

C = 4 W

M = 814 kg

$V = 1.3\ m^3$

P = 7.1 kW

A passive dewar would require 10,000 kg of helium. Clearly, it is much more desirable to use refrigerators.

CRYOSTAT MASS - ACTIVE REFRIGERATION ONLY

Earlier cryostat mass estimates were very pessimistic since they were based on long wavelength (10 cm) wigglers. The croystat diameter is about 5 times the cold volume diameter. For a 2.5 cm wavelength wiggler, the cold volume needed (Holmium plus wires) is only 5 cm x 5 cm, so the cryostat can be 25 cm in diameter. Cryostat wall thickness can be estimated using:

$$\Delta r = \left(\frac{P}{\sigma}\right) r$$

r = cryostat radius

P = maximum pressure

σ = allowed stress in cryostat

The pressure depends on the details of a quench. In the SSC, which has a much higher stored energy per unit length than a short wavelength wiggler, the maximum pressure at 10 atm. We will use 5 atm for P. The allowed stress is usually 1/5 the yield stress. For 316 LN steel at cryogen temperature, the yield stress is 1000 MN/m^2, we will use 100 MN/mm^2 to allow for differences in dynamic vs. static stresses. Thus

$$\begin{aligned} P &= 5 \text{ atm} = 0.5 \ MN/m^2 \\ \sigma &= 100 \ MN/m^2 \\ P/\sigma &= 0.005 \end{aligned}$$

(The SSC has $P/\sigma = 0.01$ and LHC has $P/\sigma = 0.005$.) The cryostat mass is then:

$$\frac{M}{L} = 2\pi r \Delta r \rho = 2\left(\frac{P}{\sigma}\right) \pi r^2 \rho$$

$$r \simeq 10 \ \lambda w \qquad\qquad \rho = 8.8 \times 10^3 \ kg/m^3$$

$$\left(\frac{M}{L}\right) \left[kg/(m)\right] = 2.8 \ \lambda_w^2 (cm)$$

At a 2.5 cm wiggler wavelength, this is only 17.5 kg/m, but at a 10 cm wavelength this becomes 280 kg/m, which agrees with the earlier worst case estimate.

Cryogen mass for this refrigerated system is about 10% of the cryostat mass, but reserve is advisable in the event of a quench. To within a factor of two, the cryogen mass can be set equal to the croystat mass.

APPENDIX

CRYOSTAT DESIGN

Maintaining superconducting magnets at superconducting state with relatively high current density requires an operating temperature of 5°K or less. This requires a cryostat composed of either a dewar or a refrigerator with liquid helium as the working media. Since a space qualified refrigerator system is not likely to be available in the short future, this study has been primarily focused on the stored liquid helium approach.

For liquid helium croystat designs, normal liquid Hr I, superfluid He II, and supercritical He are all possible candidate cryogens. Normal liquid helium has a boiling point of 4.2 K at 1 atm. So it is possible to operate a dewar at these saturation conditions (i.e. 4.2 K, 1 atm), to provide adequate cooling and pumping power to circulate the coolant around the magnet and other heat loads. However, the management of two phase (liquid/gas) media within the dewar is a complex issue. Under zero or micro-gravity conditions, it is necessary to introduce some body force to cause phase separation. Otherwise, venting liquid helium instead of gas helium becomes a probability and dewar lifetime becomes unpredictable. Introduction phase separation forces (e.g. surface tension, centrifugal, diamagnetic, dielectrophoretic etc.) would inevitably increase system mass, or system complexity, or both which made this approach very unattractive.

For a pure substance at its critical point, the liquid and vapor phase have identical properties and hence cannot be distinguished. Hence, operating the helium croystat at supercritical conditions would alleviate the problems associated with two phase media under zero gravity field. Unfortunately, helium has a critical temperature of 5.3° K and critical pressure of 2.3 atm. Therefore, supercritical helium cryogenic systems cannot be used for cooling requirement less than 5.3° K. Also operating at supercritical pressure would require a heavy pressure vessel for the dewar and also higher heat leakage through the heavier structures.

Superfluid He II is the second liquid phase which occurs at temperatures below the λ point of 2.18° K. The fluid properties of helium at this superfluid state are rather spectacular. It has zero viscosity, very high apparent thermal conductivity, and very high liquid specific heat at or close to the λ point of 2.18° K. More importantly, the fountain effect observed in the liquid He II allows the superfluid to be pumped by the "fountain effect" pump which relies on the thermal gradient and without any moving parts. Furthermore, gas helium only venting from the dewar is possible by using the "porous plug" design.

The superfluid He II system is the stored cryogen system of choice for superconducting magnets in space, operating at 5° K or less. In fact, it allows the superconducting magnet to operate at 2° K or less, which provides the benefits of higher critical current density of the superconducting coil. A simple schematic of the stored He II system is illustrated in Figure 1. In this design, the wiggler and superconducting magnet is external to the cryogen storage. The wiggler, superconducting magnet, and the cryogen storage are insulated from the space background radiation via multi-layers of superinsulation and radiation shields. Liquid He II is pumped to the cooling circuits within the heat load by the fountain effect pump and then back into the dewar. Gas helium only venting from the dewar is ensured by using a porous plug. The vented helium gas is routed to the radiation heat shield in order to reduce the heat leakage into the cryostat, before it escapes into the space vacuum.

CRYOGEN MASS INVENTORY

The stored cryogen provides cooling power to the heat load from the FEL wiggler liner heating due to synchrotron radiation absorption, magnet heating and ambient heat leakage. The wiggler liner heat load has been estimated to be less than 0.4 W/m. The magnet heat load is usually much less, except during the event of a quench. Quenching requires special thermal treatment to ensure the magnet recovers, and unless it occurs at a frequent basis, it should have relatively small impact on the total cryogen inventory requirements. The heat leakage can be made small by using

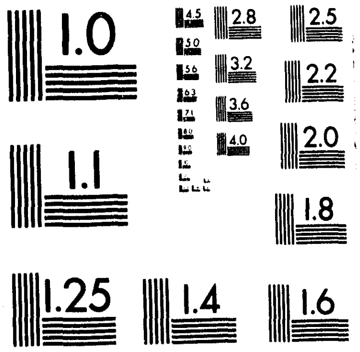
1.0
4.5
5.0
5.6
6.3
7.1
8.0
2.8
3.2
3.6
4.0
2.5
2.2
2.0
1.1
1.8
1.25
1.4
1.6

2 of 2

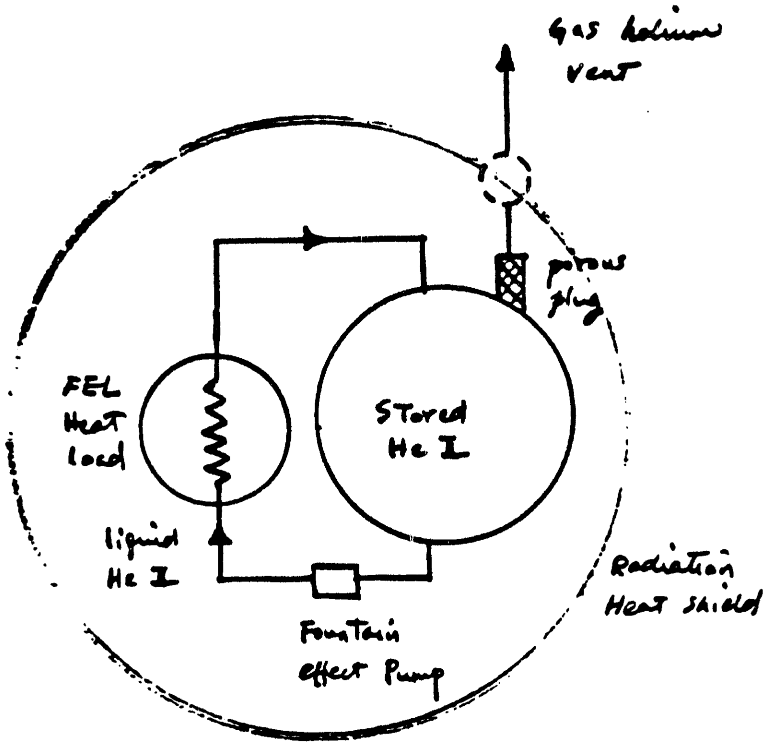

Figure 1. Schematic of Stored Superfluid He II Cryogenic System for Space-Based FEL.

advanced techniques of superinsulation, helium cooled active radiation heat shield, etc. For example, ASTROMAG [1] preliminary design using stored superfluid helium system has a radiation influx of 4 W for a cryostat volume of 4000 liters and a surface area of approximately 10 m^2. Most of the heat leakage into the cryostat is only 0.16 W. So, a wiggler design of approximately 5 cm x 5 cm/cross section, the heat leakage will be approximately $5x10^{-3}$ W/m, assuming heat leakage scaled linearly with surface area. There is additional heat loss, of course, due to the additional volume and surface of the stored cryogen.

A simple thermal model has been developed to study the amount of the stored cryogen required to maintain operation for 1 year. The schematic of a cryogen system is shown in Figure 1. The model assumed the superconducting magnet and the wiggler is uniformly at 2°K. Around them, there is one layer of superinsulation (1 in. thick) and an active radiation heat shield which is cooled by the vented helium gas. The amount of helium gas mass vented is to offset the total heat leakage into the cryostat (wiggler, magnet and dewar). The superfluid He II storage heat leakage is assumed to scale with ASTROMAG design according to surface area. The results of this study is presented in Figure 2, where the liquid He II storage required, per unit length of wiggler, is plotted against the synchrotron radiation power absorption, per unit length, in the wiggler liner. The result indicates that for low synchrotron radiation absorption (i.e. < 0.1 W/m), the heat leakage is dominant and drives the cryogen storage required. At high radiation absorption values (i.e. >0.1 W/m), the majority of the cryogen is used to cool the wiggler liner. The net result is a nearly linear dependency of the stored mass on the absorbed power, with a zero offset, which is the minimum overhead required to maintain the cryostat at 2°K. In rough order of magnitude, it takes approximately 100 Kg/m of stored liquid He II at zero radiation absorption, and it increases to approximately 1000 Kg/m at 0.4 W/m radiation absorption. The cryogen volume can be calculated with a liquid density of 0.14 Kg/liter.

REFERENCE

[1] Green, M.A. "Cryogenic Techniques for Large Superconducting Magnets in Space," Cryogenic, Vol 29, p 484-492, May 1989.

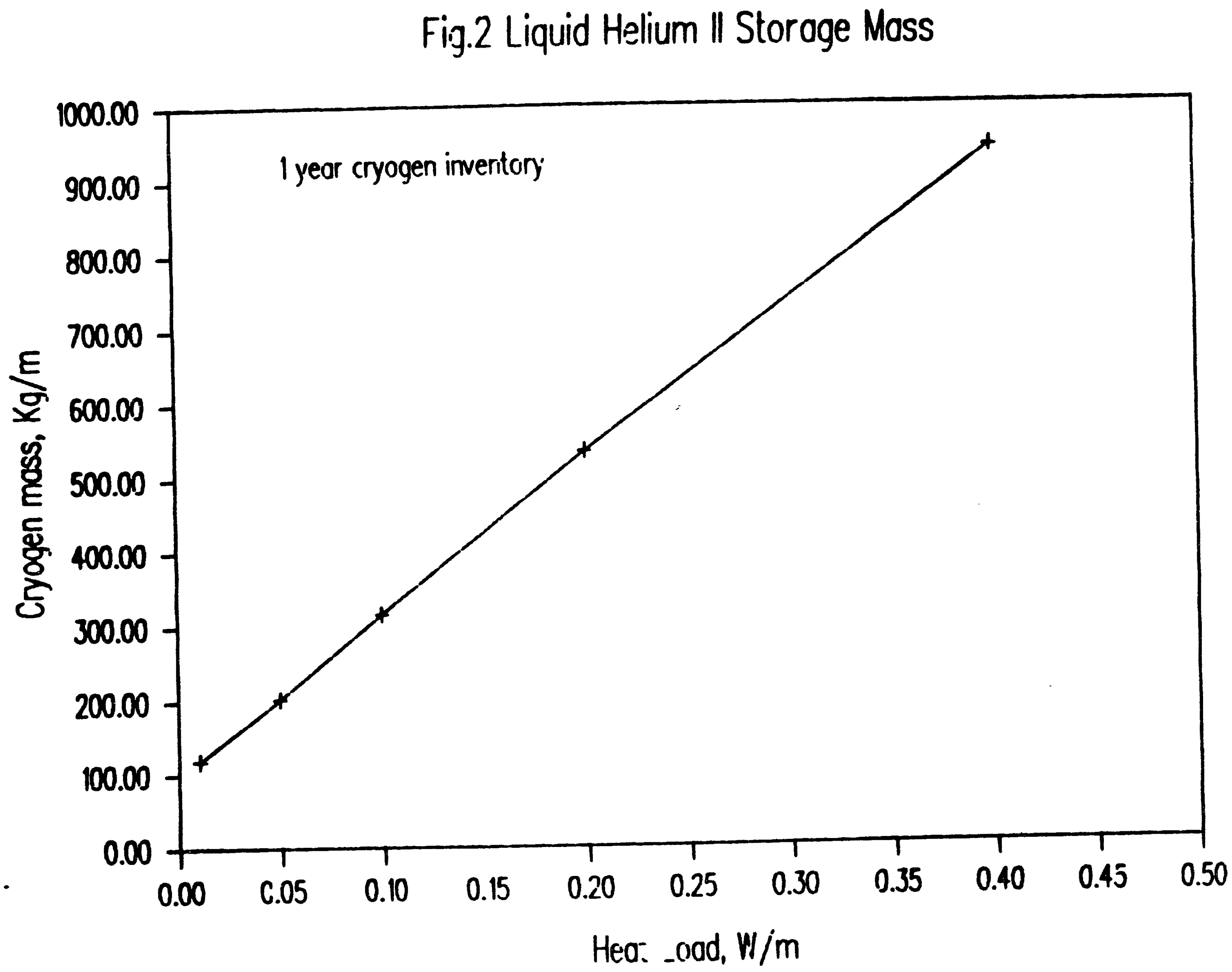

Figure 2. **Liquid He II Cryogen Mass v.s Wiggler Liner Power Absorption.**

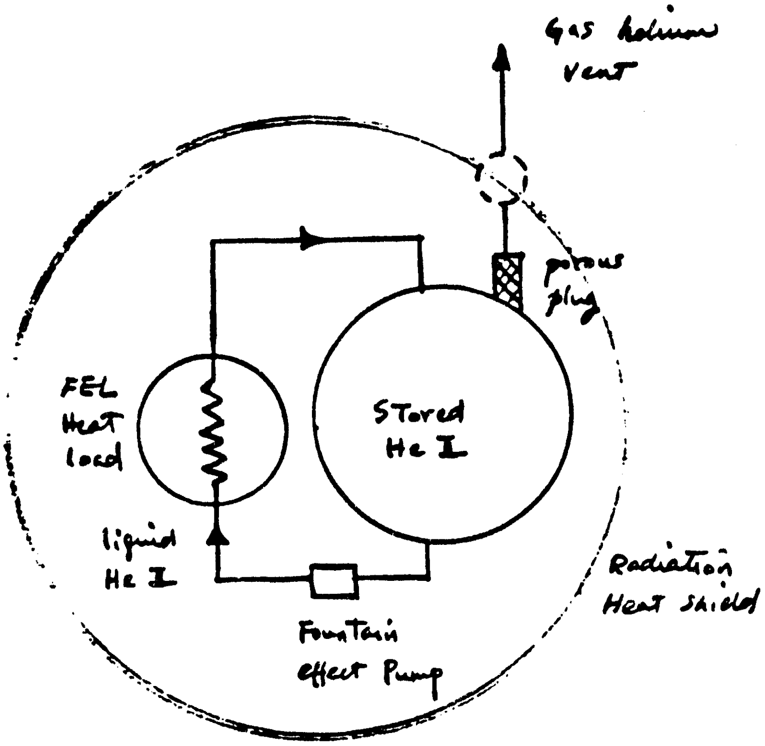

Figure 1. Schematic of Stored Superfluid He II Cryogenic System for Space-Based FEL.

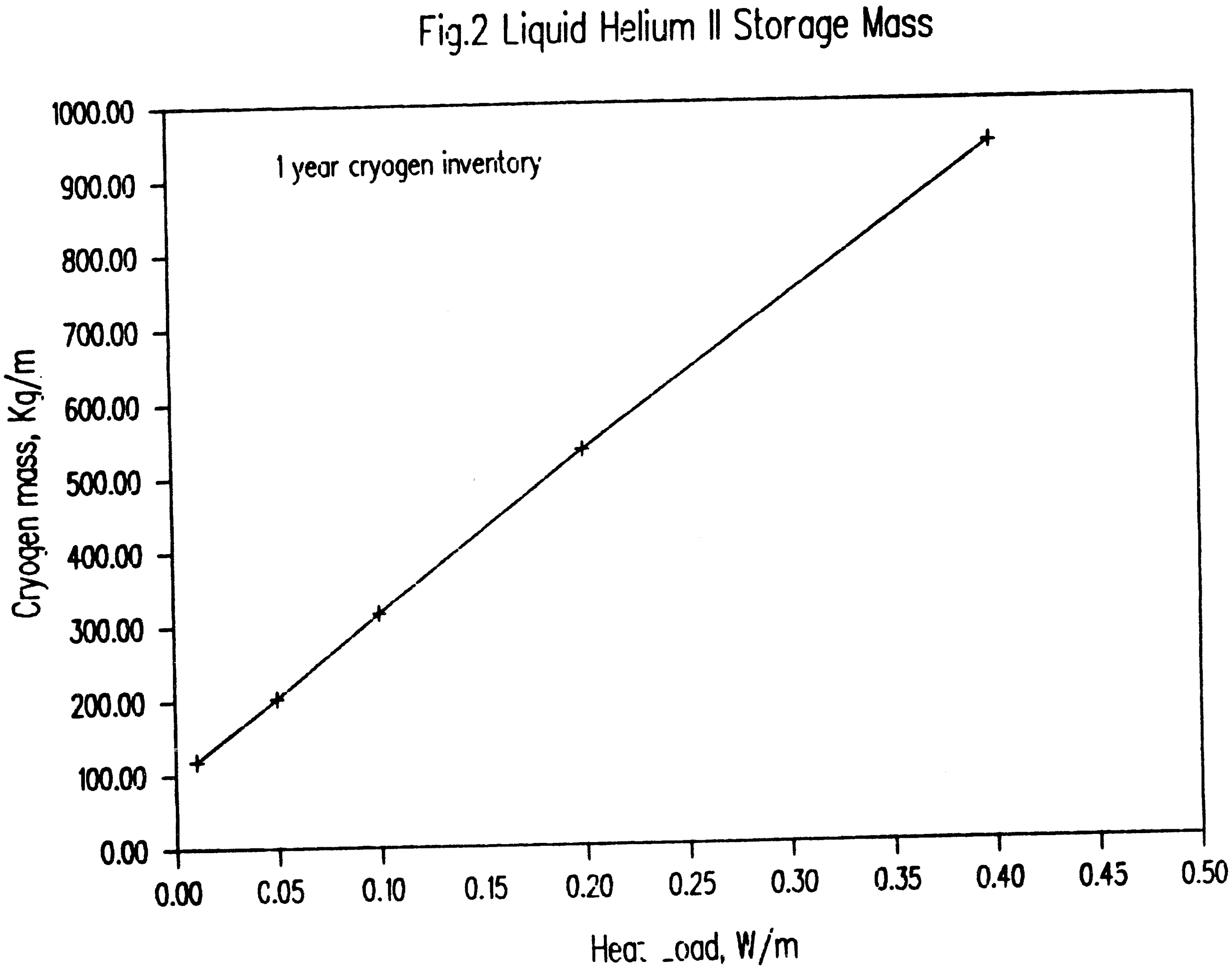

Figure 2. Liquid He II Cryogen Mass v.s Wiggler Liner Power Absorption.

Spectra Technology

ADVANTAGES OF SUPERCONDUCTING WIGGLER TECHNOLOGY TO HIGH-EFFICIENCY FELs

Presented by

Steve Gottschalk
Jack Slater

Presented at

Los Alamos National Laboratory

ADVANT
TECH

- ➤ Magnetic Field Scaling
- Extraction Optimization
- Cryostat Cooling
- Weights
- Vacuum Tube Liner
- Conclusion

ADVANTAGES OF SUPERCONDUCTING WIGGLER TECHNOLOGY TO HIGH-EFFICIENCY FELs

Presented by

Steve Gottschalk
Jack Slater

Presented at

Los Alamos National Laboratory

26 July 1990

TYPICAL CRITICAL CURRENT BEHAVIOR OF SUPERCONDUCTORS

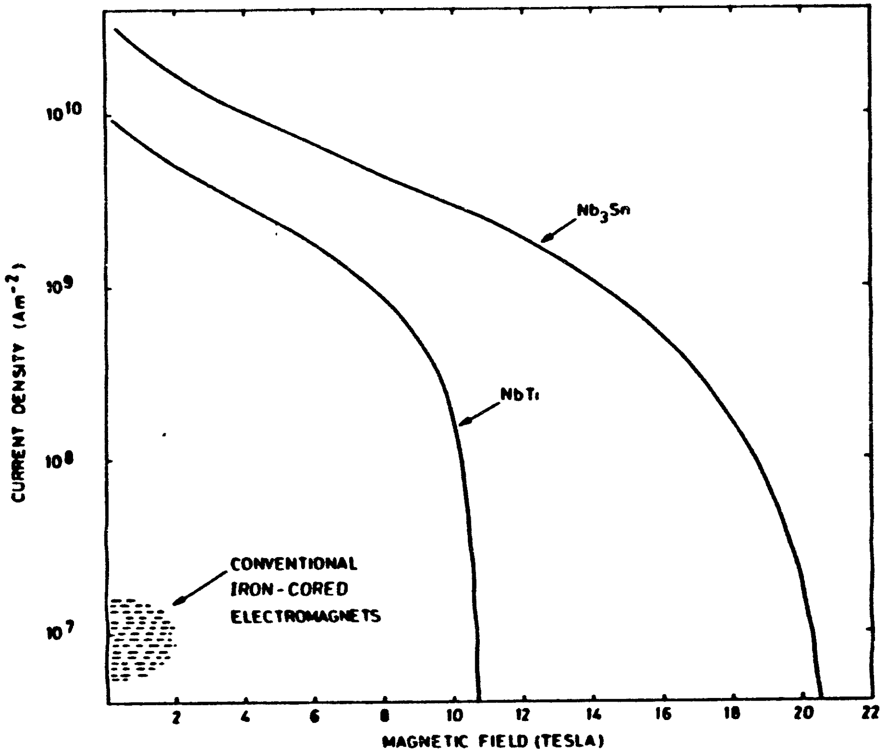

Fig. 1.2 Critical curves for the two common technological superconductors, niobium titanium and niobium tin, at a constant temperature of 4.2 K. Superconductivity prevails below the curves and normal resistivity above. Shaded area at bottom left illustrates the usual operating range for conventional electromagnets.

OVERALL BEST MATERIAL IS NbTi

- $NbSn_3$
  - Better intrinsic current, critical field
  - Hard and brittle
  - Minimum bend diameter 3 cm (60μm tape)
  - Needs lots of stablizer (4:1 or more)
- High Tc
  - Hard and brittle
  - Current, fields properties??
  - Good stability, slow normal zone propagation → cryostable
- NbTi
  - Ductile, easy to use
  - Needs little stabilizer (1.5:1)
  - Large experience base
  - Best effective current, critical field

OPTIMIZED SUPERCON WIGGLER GEOMETRY

PARAMETER	VALUE	COMMENTS
Pole Width	0.2 λ_w	Large B_{wig} reasonable peak fields
Pole Height	3/8 λ_w	Little benefit beyond 3/8 λ_w
Backplane Height	~ 1/4 λ_w	Fine adjust to eliminate coil attraction
Transverse Width	1.5 λ_w	Transverse rolloff. Shaped pole?

FIELD AT BASELINE GEOMETRY

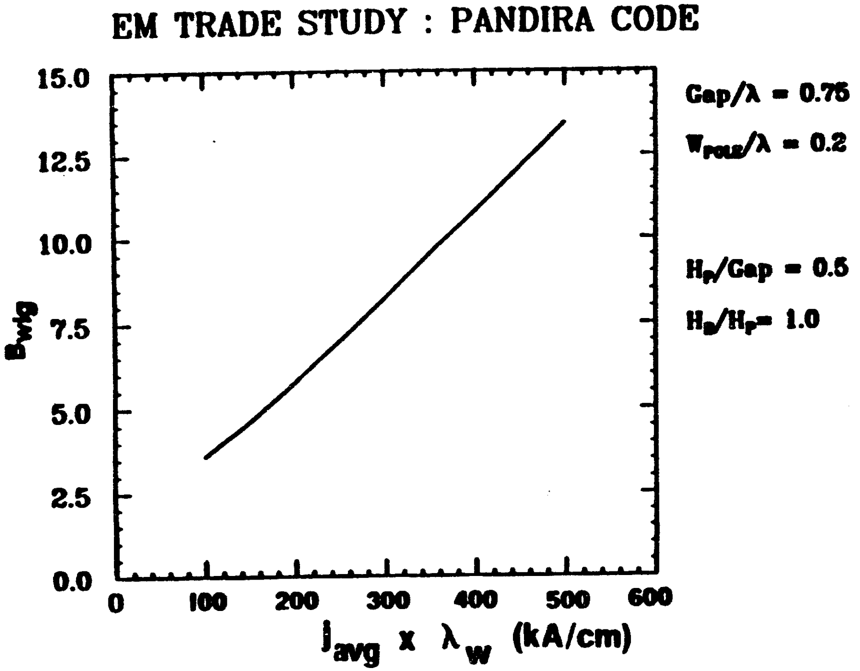

- Resulting field is

$$B_{wig}\,(T) = 1.26\, e^{-\pi g/\lambda_w} + 0.0269\, J(kA/cm^2)\lambda_w(cm)\, e^{-\pi g/\lambda_w}$$

  - Valid for $j\lambda_w(kA/cm) \geq 50$ kA/cm

STRESSES ON WIGGLER COILS ARE NOT LARGE

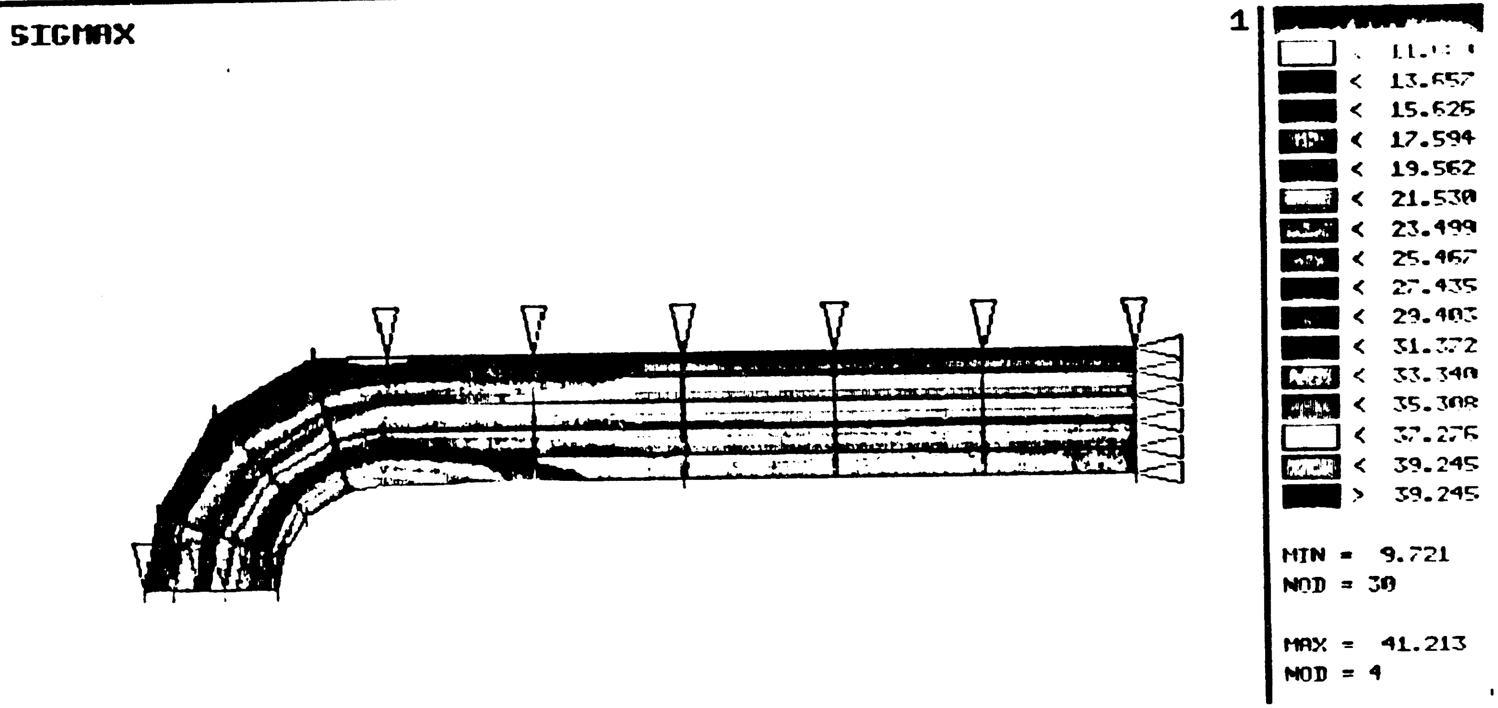

- COSMOS (stress) and PANDIRA (forces)

- NbTi:Cu is ductile, changes in superconductive properties sets highest stress at 500 MN/m^2

  - $\lambda_w = 10 \quad \sigma \leq 30\ MN/m^2$
  - $\lambda_w = 2 \quad \sigma \leq 8\ MN/m^2$

LOAD LINE USED TO ESTABLISH IDEAL CURRENT DENSITIES

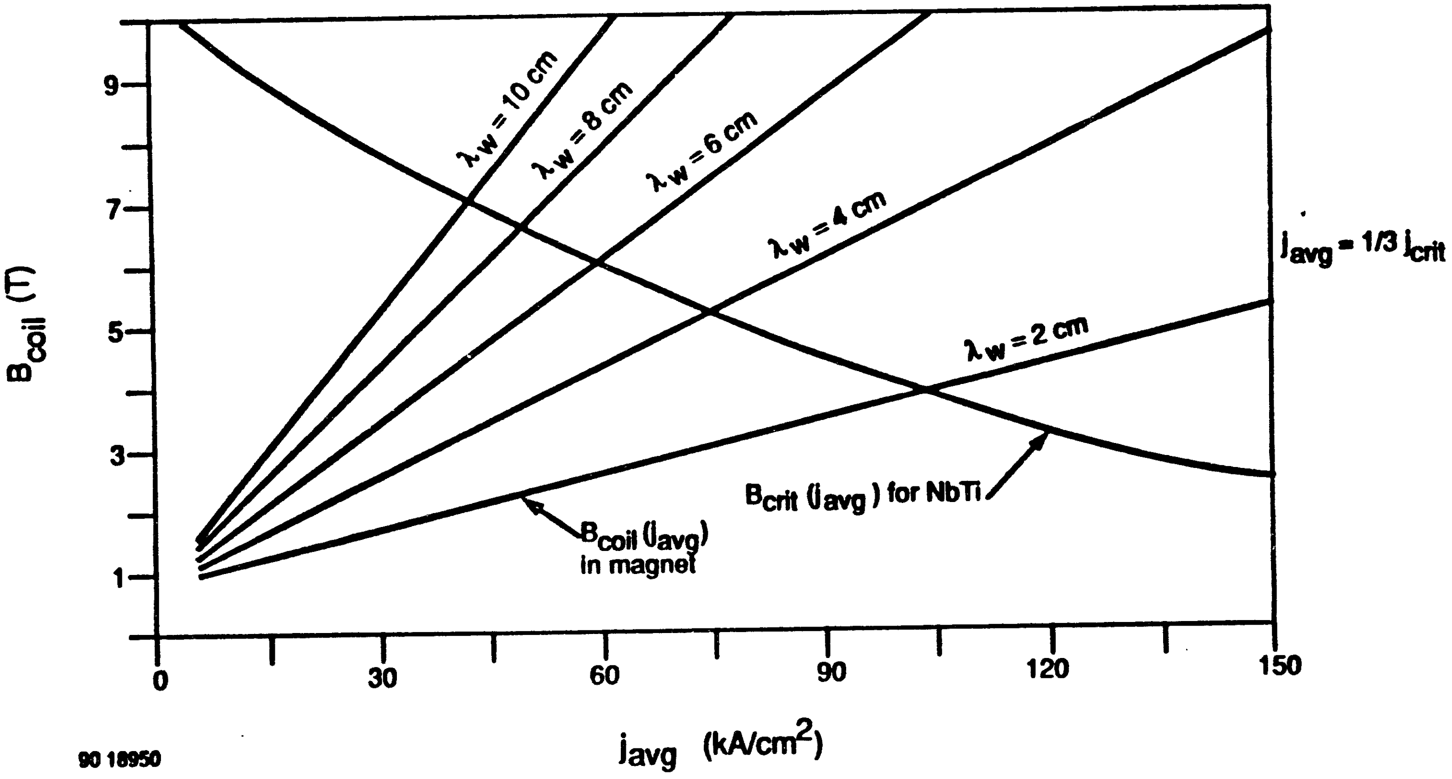

90 18950

- Peak field in windings (B_{coil}) is independent of gap

Spectra Technology

REAL CURRENTS LOWER THAN IDEAL FOR QUENCH STABILITY

DERATE FACTOR	CURRENT MULTIPLIER (1.0-NO DERATE) $\lambda_w = 2$ cm	$\lambda_w = 10$ cm	COMMENT
Cu stabilizer	0.4	0.4	1.5:1
Packing	0.83	0.83	Typical
Normal Quench	0.70	0.30	Stress/Energy Den = 1000
Point Disturbance	1.0	1.0	$>10^{-5}$ J all λ_w
Temperature Margin	1.0	1.0	$\Delta\theta > 1.0^{\circ}$K all $\lambda_w > 2.0$ cm
TOTAL	0.23	0.10	

- Estimates are conservative
- Adiabatic and dynamic flux jump stability sets conductor dimensions

HOOP STRESS/DISTRIBUTED QUENCH DENSITY IS MAIN DERATE FACTOR

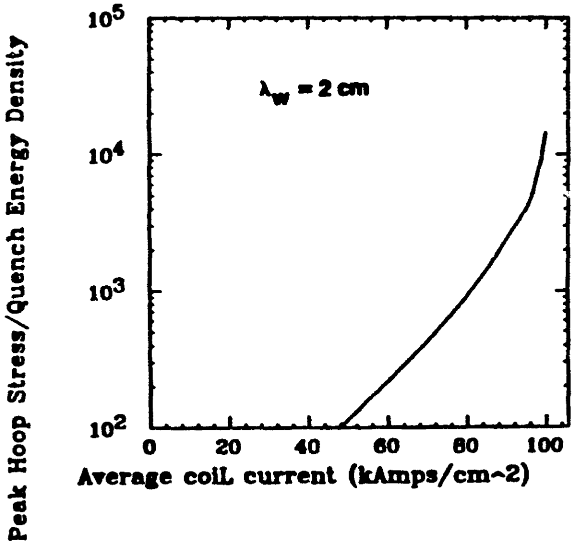

- Stresses cause conductor motion
- At 1000 can use 70%, 10^4 could use 97% of critical current
- MPZ analysis indicates point density to initiate quench 10^{-5} J to 10^{-6} J
- Both figures of merit favor using 1000

COMPARISON OF EXISTING DEVICES TO LIMIT CURVE

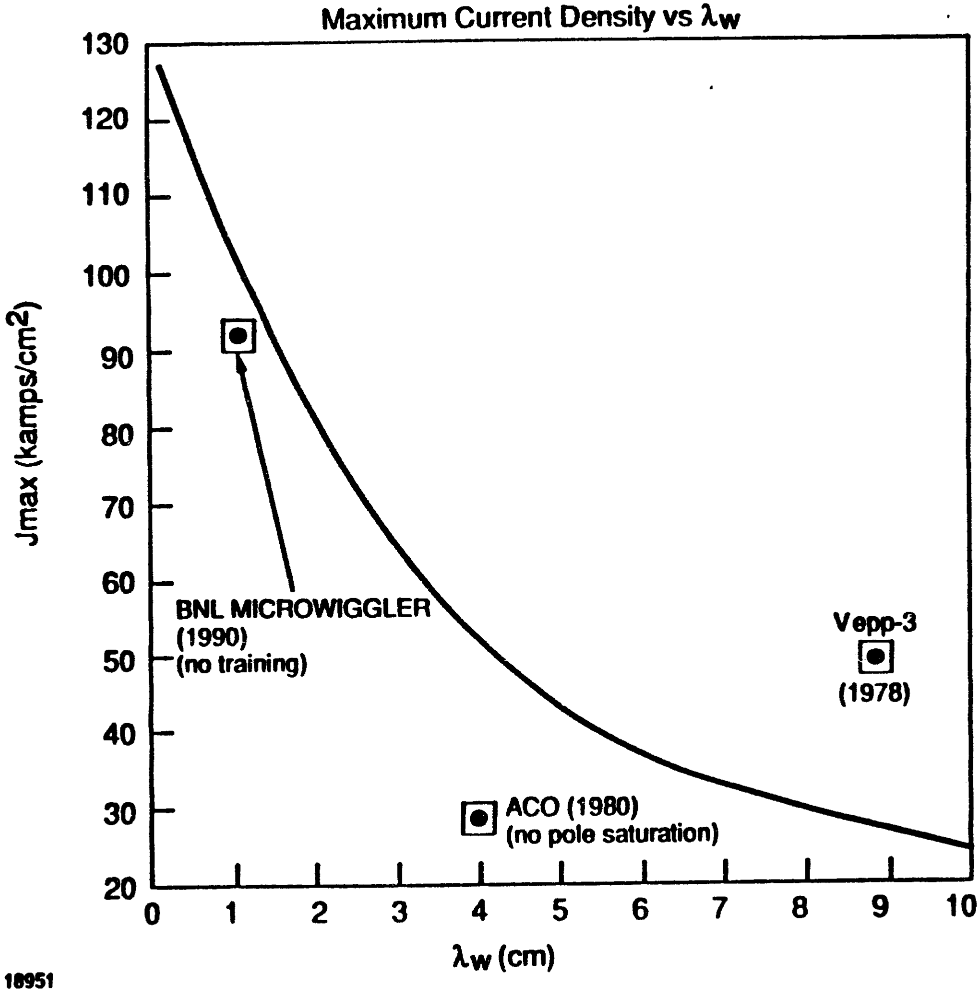

90 18951

- Independent of gap

Spectra Technology

SYSTEM SAFE FROM QUENCH DAMAGE

Temperature Rise	50 - 200°K	Low Cu resistivity High Cu specific heat
Duration	0.02 - 1 sec	Low stored energy
Voltage	200 - 3000 V	Low LdI/dt (Low λ_w best)

- Adiabatically stable magnets need quench training

SUPERCON FIELD STRENGTH CONCLUSION

- Superferric wiggler with Holmium poles, multifilamintary Cu stabilized NbTi wires
- On axis and internal field determined by g/λ_w and $j\lambda_w$
- Maximum current densities increase with decreasing wavelength
- Acceptable quench behavior

Magnetic Field Scaling

➤ Extraction Optimization

Cryostat Cooling

Weights

Vacuum Tube Liner

Conclusion

ONE FIGURE-OF-MERIT FOR FEL IS EXTRACTION AT FIXED GAIN

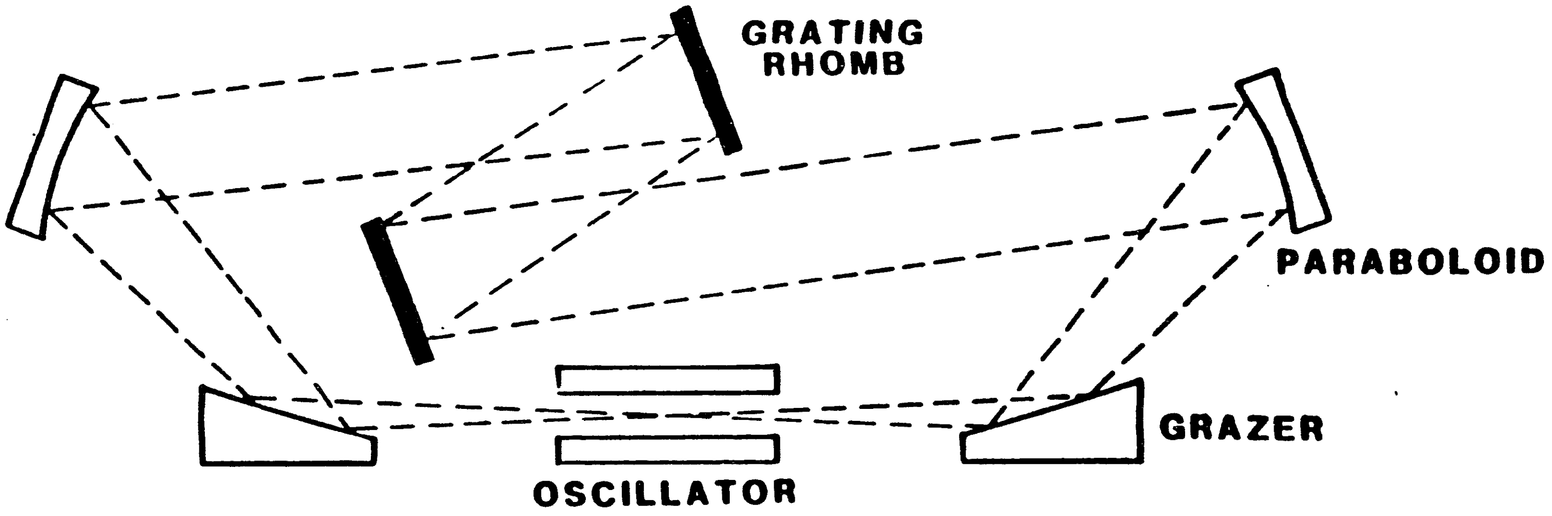

- Output coupling fixes the saturated gain
- Maximize the extraction at fixed gain

EXTRACTION DEPENDS ON INITIAL TRAPPING AND SUBSEQUENT DECELERATION

COLD BEAM

$\left(\frac{\Delta\gamma}{\gamma} << \text{bucket height}\right)$

HOT BEAM

$\left(\frac{\Delta\gamma}{\gamma} \geq \text{bucket height}\right)$

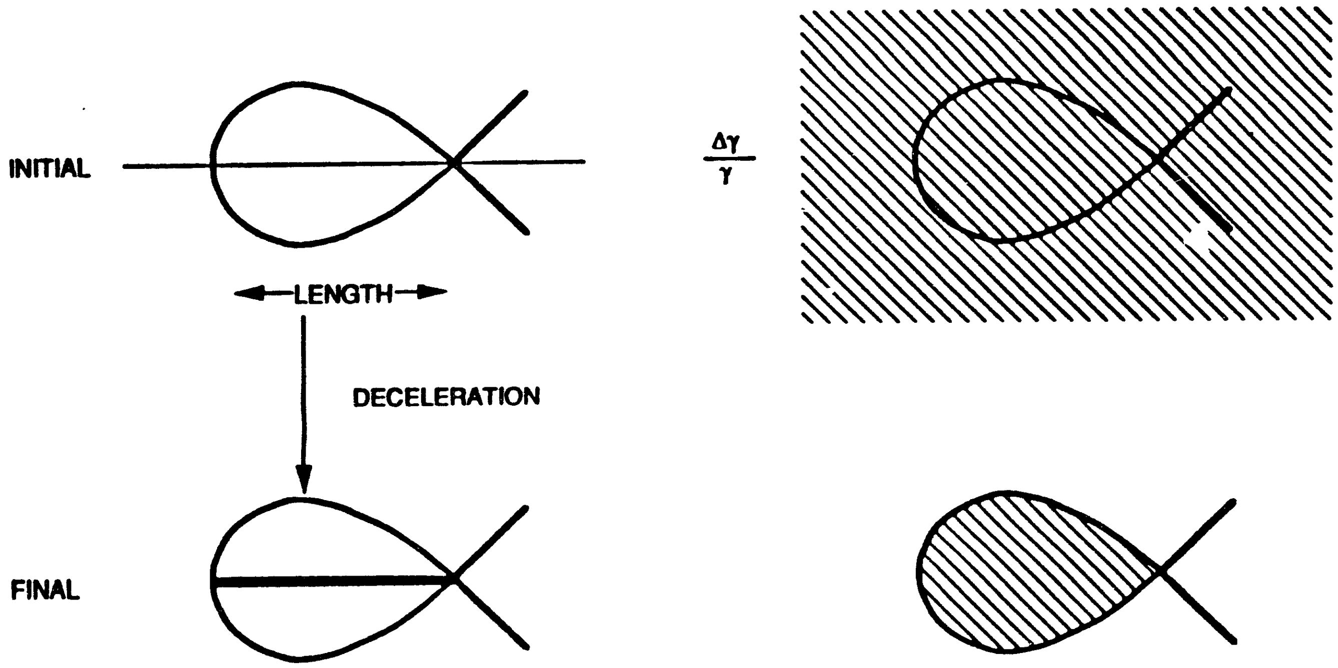

$$\eta_c = \frac{\text{BUCKET LENGTH}}{2\pi}$$

$$\eta_D = \int_{-L/2}^{L/2} \frac{1}{\gamma}\frac{d\gamma}{dz}dz$$

$$\eta_c = \frac{\text{BUCKET AREA}}{2\pi\,\Delta\gamma/\gamma}$$

$$\eta_D = \int_{-L/2}^{L/2} \frac{1}{\gamma}\frac{d\gamma}{dz}dz$$

$$\boxed{\eta = \eta_c \eta_D}$$

OPTIMIZATION PROCESS

- Analytic equations calculate extraction based on capture fraction and $d\gamma/dz$ (constant phase angle approximation)
  - OK for low and moderate gain
- Fixed parameters
  - Wiggler length
  - Gap
  - Photon wavelength
  - Gain
  - Peak current
- Vary these parameters to optimize extraction
  - B_r, λ_w - Wedged-pole hybrid
  - j, λ_w - Superconductor

SUPERCONDUCTOR GIVES 70% EFFICIENCY IMPROVEMENT IN COLD BEAM LIMIT

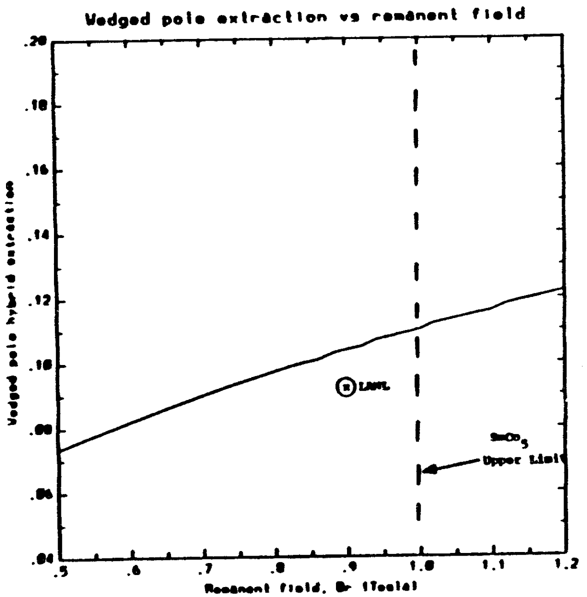

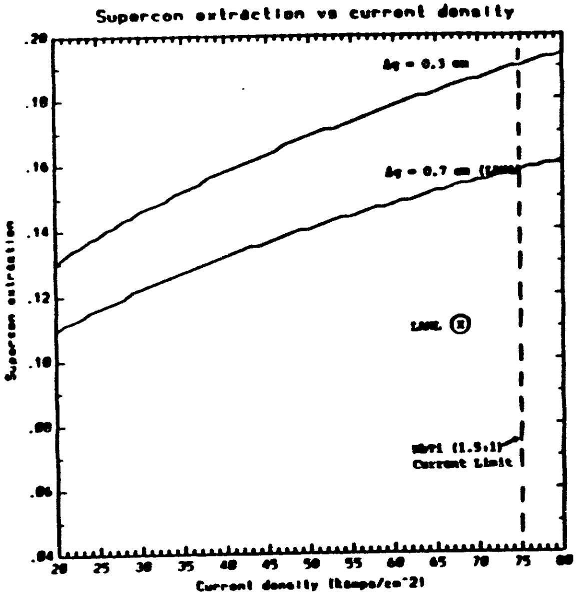

- Power increases 63% at same peak current ($L_{wiggle} = 20$ m, $\lambda_{photon} = 1.06 \mu m$, $I_{peak} = 250A$, gain = 40%, gap = 1.6 cm)

COLD BEAM RESULTS (CONTINUED)

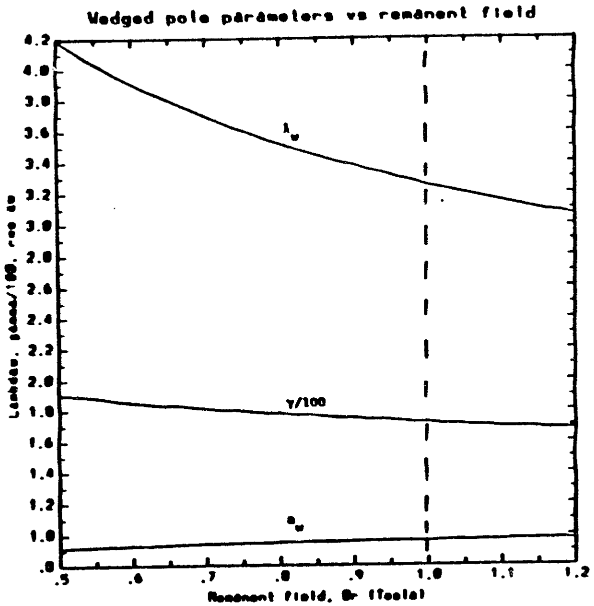
Wedged pole parameters vs remanent field

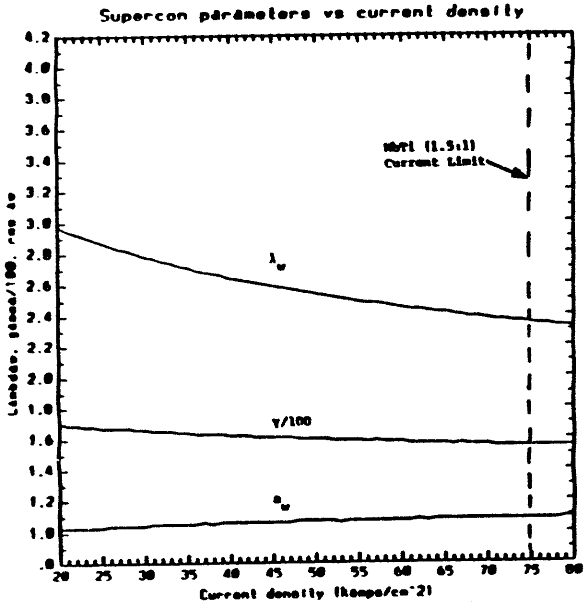
Supercon parameters vs current density

- $a_w \simeq 1$ for both technologies
- γ reduced slightly (11%) for superconductor
- λ_w much smaller, 2.4 cm for superconductor vs. 3.3 cm for WPH
- Perfect agreement with LANL's a_w, λ_w, γ for WPH and superconductor ($\Delta g = 0.7$ cm)

REASONS WHY SUPERCONDUCTOR WORKS BETTER

- Permits use of less stiff e-beam
  - Achieves $a_w = 1$ at lower γ
- Shorter λ_w increases the number of wiggler periods at a fixed wiggler length
- Large extraction increase overcomes slight energy reduction (11%) so that power gain ~ efficiency gain

COLD BEAM EXTRACTION IMPROVEMENT HOLDS OVER WIDE GAP RANGE

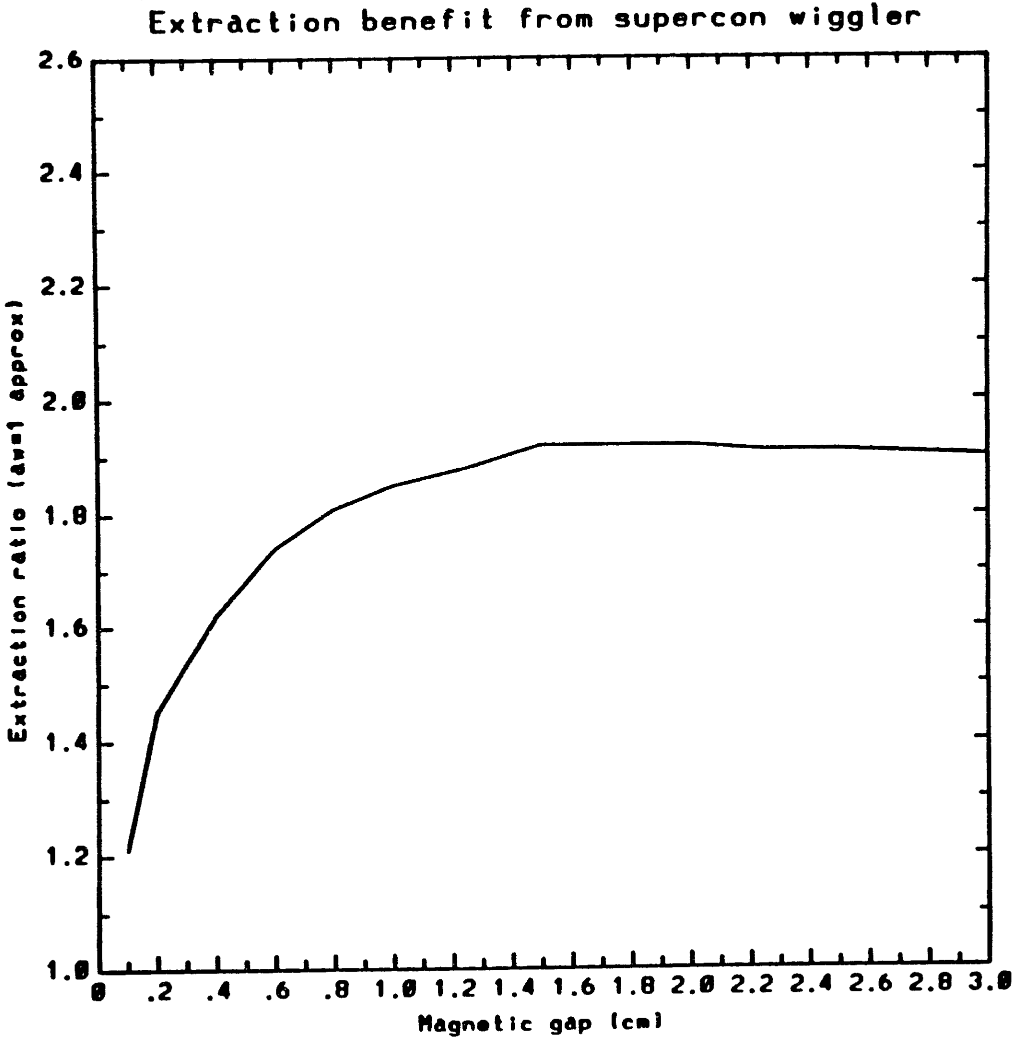

$a_w = 1$
$B_r = 1.0T$
$j = j_{max}(\lambda_w)$

Spectra Technology

WARM BEAM LIMIT HAS 35% HIGHER EXTRACTION

- Present FEL is close to cold beam

$$\left.\frac{\Delta\gamma}{\gamma}\right|_{\text{bucket}} = 2.3\% \qquad \left.\frac{\Delta\gamma}{\gamma}\right|_{\text{eff}} = 0.35\% \qquad \left.\frac{\Delta\gamma}{\gamma}\right|_{\text{E-spread}} = 0.2\%$$

- Lower power/poorer e-beam FELs approach warm beam limit

- Warm beam rules
  - Fixed total $\Delta\gamma/\gamma$ (emittance and E-spread) > bucket height
  - Optimize at fixed e-field, e-beam current

- Results

	η (a.u.)	λ_w (cm)	a_w	γ
WPH	1.0	5.11	2.24	392
Superconductor	1.35	3.43	2.82	392

- Observations
  - Same trends as cold beam
  - η_c increases with increasing λ_w, a_w while η_D decreases forcing a_w,λ_w higher

CONCLUSION

- Supercon wiggler achieves better extraction
  - 70% higher in cold beam limit
  - 35% higher in warm beam limit

- Excellent agreement with LANL's optimum a_w, λ_w, γ but not extraction
  - Breakdown of low extraction approximations in STI code
  - Insufficient taper in LANL code

- Improvement due to
  - Lower λ_w at $a_w = 1$
  - Slightly lower γ

Magnetic Field Scaling

Extraction Optimization

➤ Cryostat Cooling

Weights

Vacuum Tube Liner

Conclusion

SPACE-BASED FEL HAS UNIQUE COOLING REQUIREMENT

- Liquid He is diamagnetic
  - Cryogen collects around low field regions, away from wires
  - Pumping required to get cryogen near wires
- Pumping can be done several ways
  - "Fountain Effect" pumping using superfluid He
  - Mechanical pumping using cryogenic refrigerators

REFRIGERATION IS PREFERRED COOLING APPROACH

- Superfluid He without refrigeration
  - Use 500 kg/m/year at 0.2 W/m continuous heat load
  - Need 100 kg/m/year due to cryostat heat leaks
  - May be feasible for intermittent FEL operation
- Cryogenic refrigerator, but not superfluid He
  - Refrigerator lifetime key issue
  - Land based refrigerator, 20 m wiggler at 0.2 W/m

    Mass = 800 kg
    Volume = 1.3 m^3
    Power = 7.1 kW
- Mass comparison, 20 m wiggler

LOAD (W/m)	SUPERFLUID	REFRIGERATOR
0.2	10,000 kg	800 kg
1.0	50,000 kg	2500 kg

Magnetic Field Scaling

Extraction Optimization

Cryostat Cooling

➤ Weights

Vacuum Tube Liner

Conclusion

WEIGHT SCALINGS

- WPH weight ~ 3x (magnet + pole) weight
  - Pole height varies with g/λ_w
  - $M\ (\mathrm{kg/m})|_{WPH} = 3 \times \lambda_w^2 \times (1 + 3u - 8.7u^2 + 18.3u^3 - 9.2u^4)$
    $u = \exp(-\pi g/\lambda_w)$
- Superconductor weight
  - Magnet (kg/m) $= 0.55\ \lambda_w^2$
  - Cryostat $2\pi r \Delta r \rho = 2\ \pi r\ (P/\sigma) r\rho$, $P = 5$ atm, σ

    $= 1/10$ yield stress $= 100\ \mathrm{MN/m^2}$, $P/\sigma = 0.005$, $r \simeq 10\ \lambda_w$
  - Cryogen ~ 0.1 cryostat without reserve, set cryogen = cryostat
  - $M\ (\mathrm{kg/m})|_{\mathrm{supercon}} = 6.2\ \lambda_w^2\ (\mathrm{cm})$

BOTH TECHNOLOGIES HAVE COMPARABLE WEIGHTS

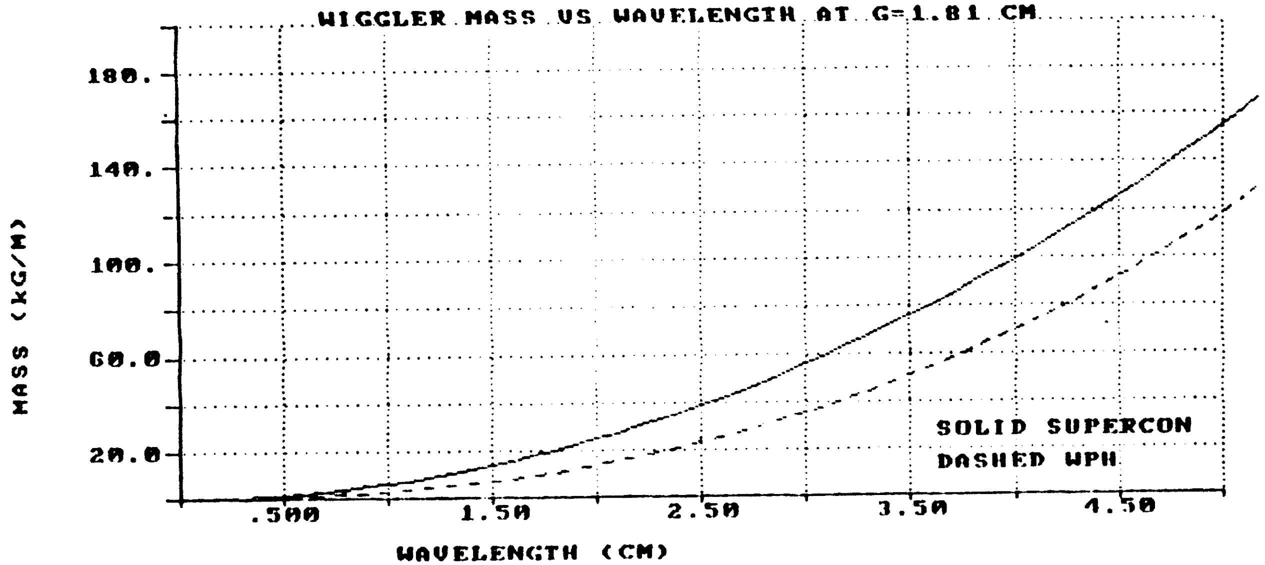

Gap = 1.81 cm

Heat Load = 0.2 W/m

1 Year Continuous Operation

- Superconductor $\simeq$ 40 kg/m + 40 kg/m refrigeration + 1 kg/m power at λ_w = 2.5 cm, L= 20M
- WPH $\simeq$ 90 kg/m at λ_w = 3.6 cm

Magnetic Field Scaling

Extraction Optimization

Cryostat Cooling

Weights

➤ Vacuum Tube Liner

Conclusion

THERMAL MANAGEMENT DETERMINES SUCCESS OF SUPERCONDUCTOR

- Absorbed heat load in magnets is key issue
- Primary heat source is resistive wall heating by e-beam image currents
- Superconductive tube lining can solve problem

RESISTIVE WALL EFFECTS

- Allow 1 W/m <u>in magnets</u>
- Major heat source is image currents

Room Temp Vac Tube	Cooled, Non-Supercon V.T	Supercon Lined V.T
1	1/10	10^{-4}
too high	may work	(preferred approach)

- Secondary heat is
  - Cryostat ≃ 0.005 W/m (Lockheed's ASTROMAG cryostat)
  - Synchrotron radiation, only 0.2 W/m generated
  - Beam scraping & scattering must be tightly controlled

SUPERCONDUCTING LINE REDUCES WALL HEATING

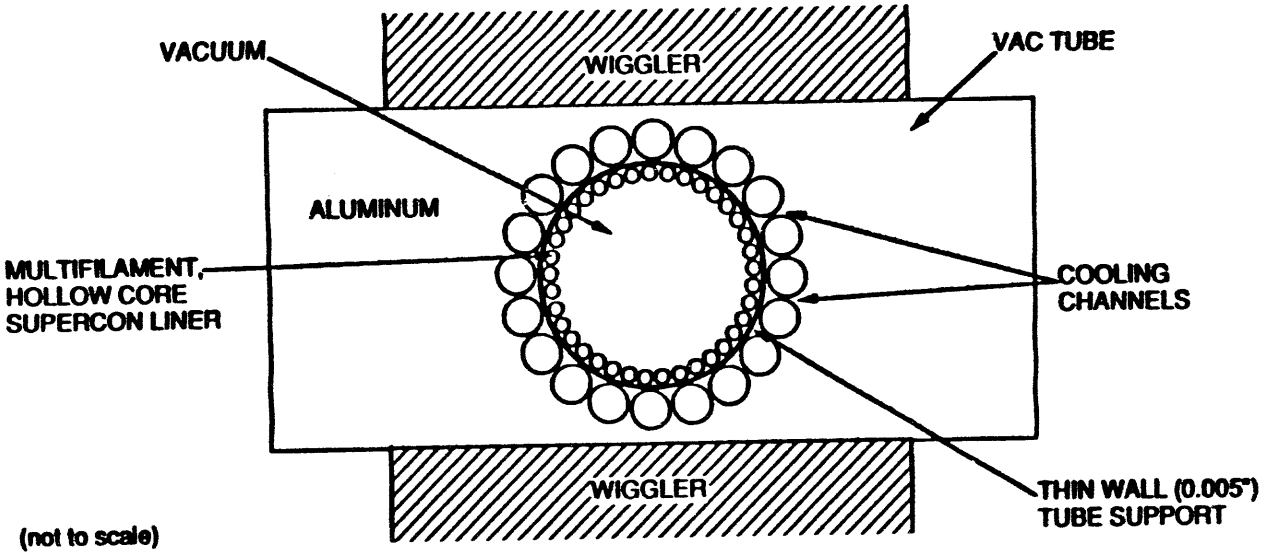

90 18913

- Rf image currrent flows in liner
  - AC impedance very low
  - Type II because of DC wiggler field
  - NbTi has $H_{c1} = 30$ G, negligible wiggler field perturbation
- Heating reduced by $6\text{X}10^{-5}$

PROPER STARTUP LETS WIGGLER FIELD PENETRATE VACUUM TUBE

- Amperes Law, quasistatic fields during charnge-up
  - $\partial B/\partial t = \nabla \times E$
  - $\sigma \rightarrow \infty$ in superconductor $E = 0 \rightarrow \partial B/\partial t = 0$
- Liner must not be superconducting during magnet energizing
- Solution is to cool liner below T_c after energizing
  - Energize with warm bore, high heat loss, then cool down
- Hollow core conductors have already been manufactured

Magnetic Field Scaling

Extraction Optimization

Cryostat Cooling

Weights

Vacuum Tube Liner

➤ Conclusion

CONCLUSION

- Have characterized superconductor geometry
  - Superferric with holmium poles and NbTi wires
- Have optimized FEL extraction efficiency
  - 70% cold beam
  - 35% hot beam
- Key issue is thermal management
- Potential solution identified uses
  - Superconductor vacuum tube liner
  - Space qualified refrigerator

DATE
FILMED
2/25/94

END